PHYSICS-BASED PRINTHEAD DESIGNS FOR ENHANCED ELECTROHYDRODYNAMIC JET PRINTING

By

Tse Lai Yu Leo

A dissertation submitted in partial fulfillment
of the requirements for the degree of
Doctor of Philosophy
(Mechanical Engineering)
in the University of Michigan
2017

Doctoral Committee:

Assistant Professor Kira Barton, Chair
Professor Placid Ferreira, University of Illinois Urbana-Champaign
Professor S. Jack Hu
Assistant Professor Ariella Shikanov

CONTENTS

LIST OF FIGURES

LIST OF TABLES

Abstract

As growth in the electronic and biomedical device industries continues on a steep trajectory, the demand for high-resolution fabrication technology will remain at the forefront of innovation. Traditional high-resolution fabrication techniques such as optical lithography, stamp printing, or ink jet printing, each exhibit significant shortcomings in addition to their acknowledged advantages. As such, they are unable to provide a cost effective solution to highly customizable feature fabrication at the micro-scale.

Electrohydrodynamic jet (E-jet) printing is a growing printing-based additive manufacturing technology for high-resolution device fabrication. It enjoys the advantages of other additive manufacturing technologies, and is compatible with a large range of materials; thus it is an advantageous choice for electronic fabrication, high-resolution prototyping, and biological component fabrication. Despite these advantages, E-jet is currently limited by two key technical challenges: (1) Low throughput due to challenges with multi-nozzle printing accuracy and lack of integrated sensing and control, and (2) Substrate constraints due to process sensitivity to offset height variations.

The research in this dissertation aims to investigate the basic physics behind the electric-field driven ink meniscus to aid in the development of new E-jet printhead designs and printing approaches to overcome the substrate limitation. In this dissertation proposal we will introduce the key process parameters that drive E-jet printing and present our design methodology that has led to 3 different printhead designs with varying capabilities. Through the observation of new printing behaviors associated with the new E-jet printheads, we investigate and analyze the relationships between these new behaviors and different controlling parameters. These studies offer new insights into the physics and dynamics that govern micro-scale E-jet printing, which can further the development of E-jet and printing-based micro-AM processes in general. As research continues, we will apply our findings and knowledge towards the advancement of printing-based micro-AM fabrication of electronics or biological devices in the future.

Chapter 1

Introduction

1.1 Motivation

To meet high efficiency and performance requirements, the electronics and biomedical industries demand high-resolution fabrication technologies. For example, charge-coupled devices (CCDs) used in high-quality digital imaging require high-resolution fabrication techniques to create high-resolution sensor arrays. Furthermore, as the interest in lab-on-a-chip devices continues to expand into different fields (e.g. chemical analysis, medical diagnostics, environmental monitoring), research will remain focused on the development of high-resolution fabrication processes to build micro-fluidic channels and chambers.

Driven by a variety of needs across various industries, many different micro-/nanofabrication technologies have been developed. Each of these fabrication techniques come with different cost efficiencies, environmental impacts, material limitations, and geometry restrictions. By identifying the strengths and weakness of several major micro-/nanofabrication technologies, we have identified a strong need for micro-scale additive manufacturing processes that can meet the currently underserved market needs. Among the numerous developing micro-additive manufacturing technologies, our work concentrates on advancing the science of electrohydrodynamic jet (E-jet) printing.

In this chapter, we will give a brief review of a few existing micro-/nanofabrication technologies, followed by an introduction to electrohydrodynamic jet printing.

1.2 Review of traditional high-resolution fabrication technologies

For the few major fabrication technologies we discuss in this section, we will assess the resolution, cost efficiency, material compatibility, time consumption, and environmental impact of each technology.

1.2.1 Optical lithography

Arguably the most prolific high-resolution manufacturing technology for electronic device fabrication is optical lithography. Advantageously, optical lithography is very cost effective for high-volume production (high costs are distributed over large volume productions), enabling high-resolution (<1μm) (Rothschild, M., et al., 2003) fabrication for mass production. The process requires cyclical patterning of 2D layers towards the production of 3D structures. In general, each cycle starts off with depositing a layer of photosensitive material onto a substrate, and then selectively patterning specific areas through exposure to a light or radiation source (UV laser or electron beam). The light exposed area is controlled by a mask, which contains the geometry/shape of the desired pattern. The light alters the material property of the exposed areas, transferring the geometric pattern from the photomask to the substrate. The pattern is emphasized either through chemical treatments that etch the exposed pattern into the material or through a series of depositions that build up a 3D structure on top of the original substrate; depending on the application.

Through optical lithography, very complicated 3D structures, such as flexible comb like structures (Sharma, K., et al., 2008) or cantilever beams (Duffy, S., et al., 2001) can be created at the micro-

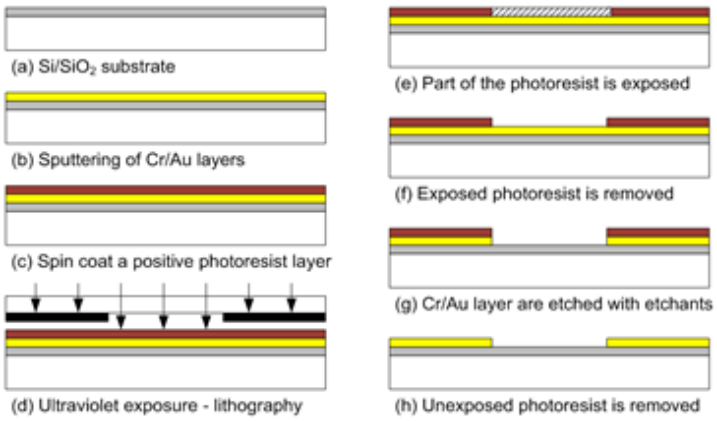

Figure 1. Schematic diagram of optical lithography (Xue, W., & Li, P. 2011)

scale with high accuracy; features size of a few hundred nanometers can be generated with minimum error. It is possible to create a large number of features simultaneously when a large mask is used; therefore the process can be used for high volume production.

A key shortcoming of this technology stems from the use of masks. The photomasks are very expensive to fabricate; they usually come with high geometric complexity and high-resolution features. Additionally, the masks require a long manufacturing time, making design iterations tedious and expensive. To create intricate 3D structures with optical lithography, several masks will be required; therefore the production process becomes very complicated, time intensive, and expensive. Furthermore, optical lithography has to be performed within an environmentally controlled space (such as a clean room or environmental chamber) because of the toxic chemicals involved, and the specific conditions required for etching and deposition. These controlled spaces are generally very expensive to use and maintain.

Further disadvantages of optical lithography include the use of harsh chemicals that are toxic to cells and biological tissues; it is therefore not suitable for biomedical applications. The use of harmful chemicals and large material waste also make this technology environmentally unfriendly. Lastly, optical lithography is not an ideal approach for small scale production due to the high costs from the masks and the cleanroom space; hence the technology is not popular among the market for highly customized features.

1.2.2 Contact printing

Contact printing is one of the oldest printing techniques in history. The process involves the use of a stamp, which is a structure with customized geometry, or a dip pen (Salaita, K., et al. 2007) to pick up ink material, and then transfer the ink material to a desired location through contact with the substrate surface. As this technology has progressed over time, the material variety of both the

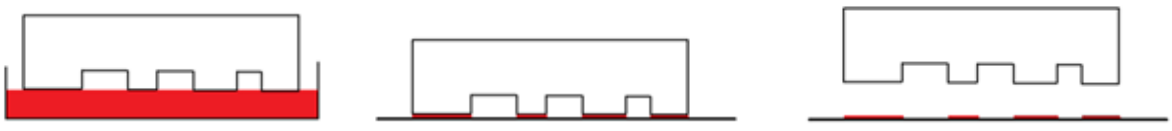

(a) (b) (c)

Figure 2. Schematic diagram of stamp printing. (a) The stamp is wetted by dipping into the pool of ink. (b) The wetted stamp is pressed onto the substrate surface. (c) The stamp is lifted from the substrate surface; ink pattern is left on the substrate.

ink and the contact source (stamp or dip pen) have increased significantly; thus, enabling the printing of new geometries and features.

Ink material compatibility includes pigmented fluids, polymers (Kumar, A., & Whitesides, G. M. 1993), proteins (Bernard, A. et al. 2001), and metals (Schmid, H. et al.2003). Contact printing has been used for applications ranging from microelectronics to biological material printing (using PDMS as a stamp material). Additionally, the resolution is not limited due to the diffraction of light (as with laser deposition processes); therefore, very high-resolution features (<200nm) can be achieved.

Interestingly, a similar technique can be used to perform transfer printing; instead of picking up ink, stamps can also be used to pick up nano/micro-scale features such as silicon nano-membrane or graphene membrane (Liang, X., et al. 2007) and place them onto desire locations. In this configuration, it can be a cost effective approach for mass production, especially when a large stamp is used. Similar to other forms of additive manufacturing, contact printing is an environmentally friendly process; minimizing waste by using only the necessary amount of material, and eliminating the use of harmful chemicals. Contrary to optical lithography, contact printing can generally be performed in an ambient rather than cleanroom environment, thereby reducing fabrication costs.

The key limitation for this process lies in the use of the stamp. Stamp deformations during the physical contact with the substrate lead to resolution and reliability constraints. Similar to the mask in optical lithography, the fabrication of the stamp can be challenging due to the complex geometry and high-resolution feature requirements. Additionally, the design of the printed pattern cannot be changed in real-time; it must be changed through the fabrication of a new stamp, which reduces the flexibility and increases the cost of the process. Due to these disadvantages, contact printing has seen limited use for creating 3D structures.

1.2.3 Inkjet printing

The use of inkjet printing has expanded rapidly in the past three decades. Initial inkjet printing processes is called continuous inkjet printing (Buehner, W. L., et al., 2001) that used a mechanical wave to break-off the ink material into droplets; an electrostatic field will then charged the droplets and a separate electric deflection field controls the droplet flight trajectory therefore the landing

location of the ink drops. An alternative inkjet printing technique requires a heat source within the ink chamber, termed bubble jet printing. In this process, a small heat source is used to heat the ink until it vaporizes into gas bubbles. The transition from liquid to gas increases the volume of the material, thereby generating a pressure within the ink chamber. This positive pressure pushes ink material out of the ink chamber through a micro-scale nozzle, and releases a droplet upon the substrate underneath. In practice, this droplet formation approach is only applicable to volatile ink that is not denatured by the heating process; as such, bubble jet printing is generally not applicable for device fabrication in the biomedical field (Allain, L. R et al. 2004).

Another popular ink jet printing approach utilizes a piezoelectric crystal within an ink chamber. As the piezoelectric crystal is charge with a voltage, it expands and generates an acoustic wave within the ink chamber. The acoustic wave manifests in the form of positive pressure within the ink chamber, pushing ink material out of a micro-scale nozzle, and releasing a droplet onto the substrate below. This inkjet printing approach is compatible with a large variety of ink materials including polymers, proteins (Allain, L. R et al. 2004), and cell suspensions (Saunders, R. E., et al. 2008). It is currently being used for printing 3D structures for industrial or biomedical applications.

Inkjet printing is a mature technology with the advantages of relatively low costs and high yield rate. It is not subjected to the use of a mask or stamp; the printed pattern can be easily customized through programming. The process is also environmentally friendly due to direct patterning with the materials and minimum use of toxic chemicals. The major restriction in inkjet printing is the printing resolution. Printed feature sizes are typically larger than 20μm due to vibration inaccuracies with the piezo actuation, and the large pressures required to release material from small nozzle openings. According to the Hagen-Poiseuille equation ($\Delta P = \frac{8\mu LQ}{\pi r^4}$, where ΔP is pressure loss, L is length of pipe/channel, μ is the dynamic viscosity, Q is the volumetric flow rate, r is the radius of channel), as the nozzle size decreases, the required pressure to release material increases rapidly. This issue is particularly significant for ink with high viscosity μ.

Based on our literature search, the market for low-volume, highly customizable devices with high-resolution features is not well met by any of these established technologies. Most of the current technologies are either too expensive or cannot accommodate real-time design changes. This

market need is driving the development of alternative micro additive manufacturing (μ-AM) technologies, one of which is electrohydrodynamic jet (E-jet) printing. In the following section, we will give a brief overview of E-jet technology and discuss its current development.

1.3 Electrohydrodynamic jet printing

As described previously, printing-based AM processes enable high customizability of printed features that are well suited for 3D device applications. However, current processes such as inkjet printing are limited by available resolution of the printed features. Electrohydrodynamic jet technology has emerged as a promising approach to increase the resolution of printing-based μ-AM as compared to inkjet printing. In this section we will explore the development process of E-jet printing, its current capabilities as well as limitations.

1.3.1 Brief history of electrohydrodynamic jet printing

The first scientific record of electrohydrodynamic phenomenon was found in the sixteenth century by William Gilbert. The early work regarding electrohydrodynamics started approximately 100 years ago. In 1914, an experiment with an electrohydrodynamic jet was proposed as an approach to measure electric intensity of conductive surfaces (J. Zeleny 1914). In this record, a conical shaped meniscus of fluid at the tip of a small nozzle charged with high voltage was recorded, along with the first documented record of electrohydrodynamic spray behavior. This conical shaped meniscus was termed "Taylor Cone" after Sir Geoffrey Ingram Taylor. Sir Taylor is one of several earliest scientists who created an analytical physics model of the electrohydrodynamic phenomenon.

Electrohydrodynamic spray (e-spray) is a very popular spray painting technique in industry. Since the released ink droplets from the nozzle are highly charged, they repel each other during flight, leading to a large spray coverage area. There were also applications of e-spray for fluid atomization in mass spectrometry (Lai, S. T., *et al., 1980*) or deposition of particles.

Following this early work, electrospinning (e-spinning), a process that utilizes the stable jet mode of electrohydrodynamic phenomenon to generate fine filament of fluid, was patented in 1934 by Formhals, A. (Li, D., & Xia, Y. 2004). In the early 1990's, researcher groups such as the Reneker Group from the University of Akron started to investigate the use of electrospinning for

photovoltatic technology with organic polymers. Since the initial introduction of e-spray and e-spinning, research regarding electrohydrodynamic phenomena has increased rapidly. Over the past two decades, process advancements have been focused on an electrohydrodynamic technique that utilizes the stable cone jetting mode of electrohydrodynamic atomization to print discrete and high-resolution (<20μm) fluid droplets onto a substrate. This process has been termed electrohydrodynamic jet (E-jet) printing, and significant growth can be observed in the past 16 years (see Figure 3).

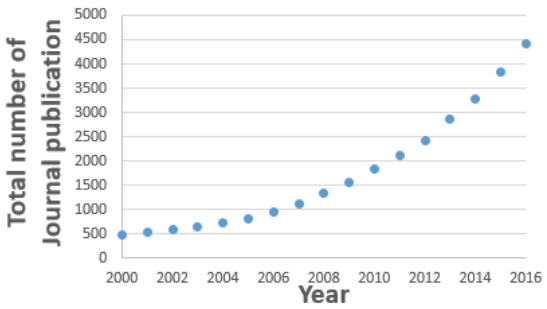

Figure 3. E-jet publications since 2000 as determined from Google Scholar.

1.3.2 Working principle of E-jet printing

Figure 4 shows the schematic diagram of a traditional E-jet setup, which includes an ink-filled nozzle above a conductive substrate that is connected to a computer controlled voltage amplifier. As the ink gets charged with a high voltage and the substrate is grounded, the electrostatic force upon the ink material draws the ink to the nozzle tip. When the charged ink material forms a meniscus at the nozzle opening, the interaction between the surface tension and the electrostatic force within the ink material deforms the usually round meniscus into a conical shape, termed a Taylor Cone. If the critical level of electric field intensity is reached, the tip of the Taylor Cone will be drawn towards the substrate as a small ink droplet.

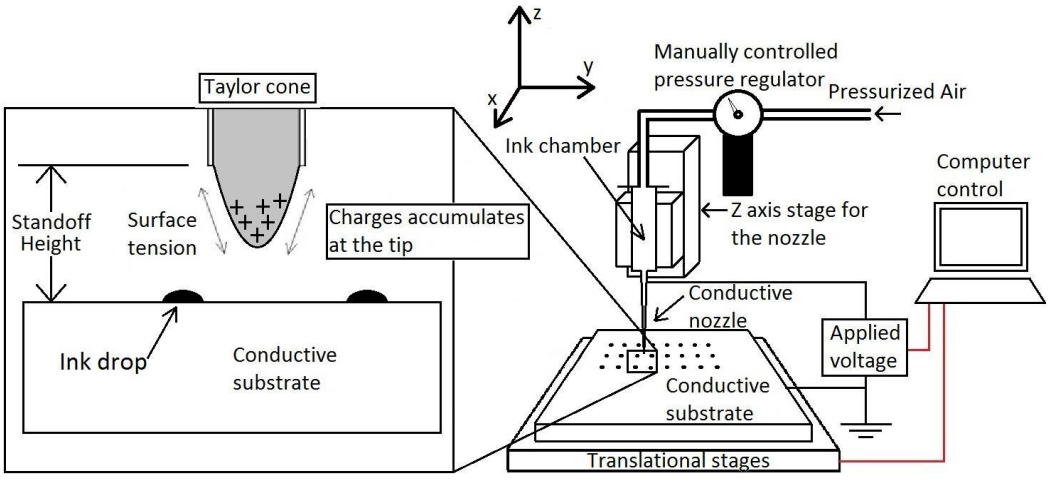

Figure 4. Schematic diagram of a traditional E-jet printer.

E-jet printing behavior is mainly controlled by (1) nozzle opening diameter, (2) standoff height between the nozzle tip and the substrate, (3) voltage difference between the nozzle and the substrate, (4) air pressure supply to the ink filled nozzle, and (5) ink material. The process undergoes different printing modes such as dripping, spraying, stable cone jetting, and multi-jet printing (Hayati, I. et al. 1986) depending on the interactions between these controlled parameters and key environmental conditions. For high-resolution (<20μm) E-jet printing, the stable cone jetting mode is utilized, which usually involves a relatively low voltage (<550V), short distance (<3mm) between the nozzle and substrate, and a nozzle size ≤200μm. During the E-jet printing process, the tip of the Taylor Cone is stretched into a thin stream of fluid jet until the tip breaks into small ink droplets that are typically smaller than the diameter of the nozzle. After one or more ink droplets are released, the charge within the Taylor cone has been reduced and the ink will then retract due to surface tension. This process is repeated as the charge builds up once again, creating a new Taylor cone, and allowing the release of another round of ink droplets.

1.3.3 E-jet printing with pulse signal

The ink droplet size and printing frequency are both affected by the printing voltage. According to Choi, H. K., *et al.* (2008), the ink droplet diameter can be estimated with the following equation:

$$d \propto \sqrt{\frac{\gamma}{\varepsilon_o}} \frac{\sqrt{d_N}}{E} \tag{1}$$

In equation (1), d is ink droplet diameter, γ is the surface tension of the air-ink interface, ε_o is permittivity of free space, d_N is the nozzle diameter, and E is the magnitude of the electrostatic field. The volume of the ink droplet x can therefore be estimated with the following equation:

$$x \propto \left(\sqrt{\frac{\gamma}{\varepsilon_o}} \frac{\sqrt{d_N}}{E}\right)^3 \tag{2}$$

E in turn can be determined with the following equation (Eyring, C. F., *et al.,* 1928**,** Marginean, I., *et al.,* 2006):

$$E = \frac{4V}{d_N \ln\left(\frac{8H}{d_N}\right)}. \tag{3}$$

In Eqn. (3), H is the standoff height between the nozzle and the substrate, and V is the voltage difference between the nozzle and the ubstrate, the unit of E is V/μm.

On the other hand, the natural jetting frequency of E-jet can be estimated with the following equation:

$$f \propto \left(\frac{\varepsilon_o^3}{\rho^2 \gamma}\right)^{\frac{1}{4}} \frac{E^{3/2}}{d_N^{3/4}}. \quad (4)$$

In equation (4), ρ is density of the ink. Notice the natural jetting frequency is once again dependent on E, which is a function of V.

To control the ink droplet size and the jetting time of ink droplets independently, Mishra, S., *et al.* (2010) developed the technique of pulse printing. For a certain voltage V_o, the E-jet nozzle gives a particular ink droplet diameter d_o, ink droplet volume x_o and jetting frequency f_o. The time in between each ink droplet release is therefore $1/f_o$. By applying a pulse signal with peak voltage at V_o and a pulse width that is a multiple of $1/f_o$, the user is able to control how many ink droplets with a volume of x_o be released. Since the ink droplets released by a pulse signal will overlap and fuse into a large single droplet if the stage movement is slow enough during the pulse, the user can control the ink droplet size by controlling the pulse width. The resultant fused ink droplet volume will therefore always be a multiple of x_o. Using this pulse printing technique, the user will also be able to control the ink droplet release time by adjusting the time spacing between each pulse signal; the natural jetting frequency will no longer determine the start time of ink droplet release.

1.3.4 Current capabilities of E-jet printing

E-jet printing has not been widely applied in industry at this stage; however, it has been applied to the deposition of various materials in many research fields. The major advantage is its high-resolution printing capability; ink droplets down to ~100nm have been shown in literature (Onses, M. S., *et al.* 2015). E-jet has also been demonstrated with relatively high frequency printing rates (10kHz)[1] on a flat substrate surface (Mishra, S., *et al.* 2010).

E-jet's high-resolution printing capability allows it to lay down thin lines of conductive ink material that are invisible to the naked eye. Such a property was used by Seong, B., *et al*. (2014) to create a transparent heating unit; they E-jet printed a grid of conductive mesh composed of thin silver nanoparticle lines on a glass substrate, which heats up when the silver lines are electrically charged. On the other hand, since the ink droplets released from an E-jet nozzle are charged, some researchers have utilized this property to create microscopic charge patterns and dope a transistor at the micro-scale (Park, J. U., *et al.*2010). Lastly, E-jet has been demonstrated to work with a

[1] Anecdotally, experimental demonstrations of > 25kHz printing frequency have been performed.

wide variety of materials including viscous biological materials such as glycerol or protein suspensions. One application of E-jet printing with biological materials can be found in (Poellmann, M. J., *et al.* 2011) in which E-jet printing was used to create a cell culture environment by E-jet printing a fibronectic pattern onto a hydrogel surface. Figure 5 demonstrates this process as performed in the Barton Research Lab. Figure 5a shows a dot matrix of fibronectin solution is printed onto a hydrogel surface, while figure 5b shows that some of cells in the cultural fluid adheres to these printed dots of fibronectin.

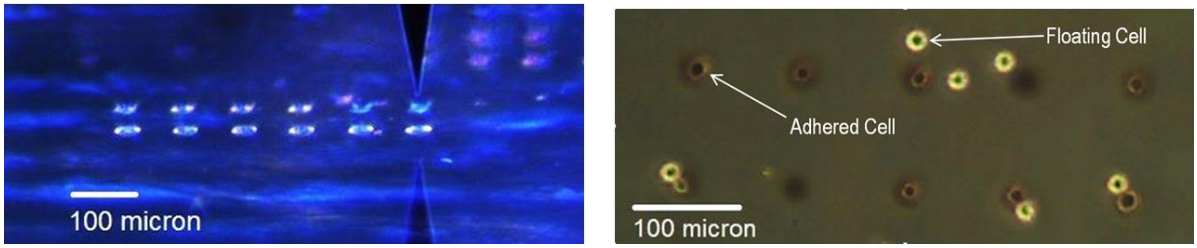

(a) (b)

Figure 5. Demonstration of E-jet printing of fibronectin on a hydrogel substrate for cell culturing.

1.3.5 Limitations of E-jet printing

The two major limitations of E-jet are substrate restrictions and low throughput. The impact of substrate condition (material or flatness) upon E-jet printing behavior is termed substrate effect. To maintain a consistent standoff height between a conductive nozzle and substrate, the substrate needs to be a surface with high flatness (commercially available glass slides exhibit flatness variability on the order of 6μm/in). This restriction prevents E-jet from printing on a contoured surface with high fidelity unless the printing voltage or standoff height is adjusted accordingly.

E-jet printing currently exhibits low throughput as compared to traditional inkjet printing because the use of multi-nozzle arrays has demonstrated significant challenges due to multi-nozzle/substrate alignment mismatches and electric field interference between nozzles (Takagi, M. F. and Ferreira, P. M., 2013). When multiple charged nozzles are placed in close proximity to each other and form a nozzle array, the electrostatic field of each nozzle interferes with the electrostatic fields of neighboring nozzles, driving the ink droplets into undesirable trajectories (Khan, A., et al. 2011). This interference behavior between adjacent nozzles is termed cross talk effect. Additionally, if the substrate is not a surface with high flatness, the jetting behavior of each nozzle in the array will vary according to their corresponding standoff height above the substrate (e.g. alignment mismatch).

Essentially both of the identified limitations (substrate effect and low throughput) can be attributed to interference of the electrostatic field from the surrounding environment. It is therefore an important topic to investigate possible solutions for reducing the interference effects due to these external factors. Several studies in the literature have been focused on reducing the substrate effect. Consequently, we started our investigation of electrostatic field interference with this body of work, which should give us some general insights into different types of interference phenomenon.

1.3.6 Substrate effect in E-jet

Within a conventional E-jet setup, the substrate is part of the electrohydrodynamic controlling mechanism. The change in E-jet behavior due to a change in substrate properties is termed "substrate effect". For a particular nozzle size and voltage difference level across the nozzle and substrate, conventional E-jet can only give steady printing behavior if (1) the standoff height remains constant throughout the printing process, (2) the nozzle is perpendicular to the substrate surface, and (3) the substrate has an even charge distribution throughout the printing cycle. Printing on surfaces that do not meet these three criteria can lead to ink droplet scattering, inconsistency of ink droplet size, or inaccurate ink droplet placement.

Assume that these three conditions are met, the ink releasing rate in volume from a conventional E-jet nozzle can be estimated with Eq. (5) according to Choi, H. K., et al. (2008):

$$Q \approx \frac{\pi d_N^4}{128\mu L}\left(\Delta P + \frac{1}{2}\,\varepsilon_o E^2 - \frac{4\gamma}{d_N}\right) \tag{5}$$

Where Q is the ink releasing rate, dN is the nozzle opening diameter, μ is the viscosity of the liquid, L is the length of the nozzle, ΔP is the pressure difference between the ink chamber and the ambient air, ε_o is permittivity of free space, γ is the surface tension of the air-ink interface, and E is the magnitude of the electrostatic field, which is determined in equation (3).

Equation (5) describes the situation when the ink - air pressure difference (ΔP) and the electrostatic field (E) exceeds the resistance due to the capillary pressure ($4\gamma/d_N$), ink material in the nozzle will flow (Q becomes positive) and be released from the nozzle. In most of our experiments, no extra air pressure is supplied into the ink chamber during printing; as such, E-jet will only happen when the electrostatic field (E) overcomes the capillary pressure ($4\gamma/d_N$). Notice $4\gamma/d_N$ is a constant value

once the nozzle diameter and ink material are chosen. Therefore E-jet printing or the ejection of material occurs within a particular printing setup when E reaches a certain constant threshold.

If we return to equation (3), we can see that a change in standoff height H leads to a change in electrostatic field intensity E. Assume there exists a minimum value of E that overcomes the capillary pressure and enables the release of material; as standoff height H increases (nozzle printing across a non-flat substrate surface), E will decrease according to Equation (5) and may potentially drop below the threshold that overcomes capillary pressure, therefore stopping the printing. On the other hand, if the standoff height H decreases, E will increase, and ink flow rate Q will increase leading to the release of more ink droplets.

To maintain consistent printing throughput a printing cycle, it is undesirable to let electrostatic field intensity E fluctuate at any time during the print. There have been various approaches and attempts to maintain E at a constant level regardless of the substrate condition provided in the literature. These approaches will be discussed in the following section.

1.4 Prior art for substrate effect reduction

We classify the various E-jet printhead designs and printing techniques that aim to mitigate substrate effects into 3 categories: (1) unique solutions, (2) control loop implementation techniques, and (3) nozzle and extractor ring style printheads. The following sections will discuss the strengths and weaknesses of these approaches.

1.4.1 Unique solutions

Unique solutions are defined as E-jet printing approaches that have been designed for particular settings and therefore cannot be easily generalized to other E-jet printing conditions. One common technique for printing on a non-conductive surface is to place the non-conductive substrate upon a grounded conductive surface or pin (Poellmann, M. J., *et al.* 2011, Lee, J. S., *et al.*2008, Wei C., *et al.* 2014, Song, C., *et al.* 2015). This technique is only applicable to non-conductive surfaces with high flatness and constant thickness across the substrate.

Another E-jet printing technique that builds upon this approach utilizes e-spinning. E-spinning refers to the technique of creating fine filaments of ink material in the form of a very long and

narrow Taylor Cone, which is only applicable to very viscous ink materials. Given the high viscosity of the ink material, the ink and substrate maintain contact through a long, thin Taylor Cone even if there is rapid change in substrate condition; which means e-spinning can continue even if there is a rapid change in substrate condition. The e-spinning nozzle can move across a contoured surface without breaking the continuous strand of viscous fluid. The ability of e-spinning to lay down long strands of viscous ink material upon a contoured surface enables e-spinning to perform 3D printing on a grounded platform (Wei, C., & Dong, J. 2014). Using e-spinning, researchers were able to construct the foundation of a 3D structure by laying down a raster of ink material. By laying down another raster on top the first layer of raster (which was a contoured surface), a 3D structure was formed. The process can be repeated by increasing the printing voltage as the nozzle moves up in height.

Clearly, printing on a contoured surface using these techniques requires a priori knowledge of the height variations of the substrate surface and a dynamic printing voltage that has been characterized before the start of the printing cycle. While these unique solutions can effectively meet very specific application needs with low cost and focused efforts; they are restricted to certain situations and fail to greatly expand the capabilities of E-jet printing.

1.4.2 Control loop implementing techniques

As mentioned in section 1.3.6, a consistent printing behavior can be maintained if electrostatic field intensity *E* stays constant. One method for maintaining constant printing behavior is to integrate a control loop into the process. Example control architectures that use current detection or vision-detected ink meniscus height as an indicator of *E* that is then used to determine an appropriate adjustment in the printing voltage can be found in Barton, K., *et al*. 2011 and Altin, B., *et al.* 2014. These approaches are restricted by sensing challenges such as poor signal-to-noise ratio, low camera resolution, and low camera frame rates. Another approach for controlling the system to maintain a constant nozzle-to-substrate standoff height involves scanning the substrate prior to printing. The scan provides the substrate topography that can be used to derive a nozzle trajectory profile that will ensure consistent printing (Seong, B., *et al.* 2014). Consequently, this technique is only applicable to substrate surfaces that can easily be scanned before printing and not dynamically changing surfaces as one would expect in 3D printing.

Control loops can theoretically be implemented in any E-jet printer. However, these approaches are generally expensive to acquire; the sensing devices in the system require high-sensitivity to measure the high-resolution changes that occur during the printing process; and the actuators must be highly accurate with short reaction times so that they can apply appropriate signals to the printer at the right time.

1.4.3 Nozzle and extractor ring style printhead

Another approach to overcome the substrate effect is to reduce the role of the substrate within the electrohydrodynamic process with a grounded electrode ring (Lee, J. S., *et al.* 2009, Kim, Y., *et al.* 2008, Lee, S., *et al.* 2008, Choi, J., *et al.* 2008, Pan, Y. *et al*, 2015). The designs of these printheads are very similar; a grounded electrode ring (often termed extractor ring) is placed in between the positively charged nozzle tip and the substrate. With the extractor ring in place, the role of the substrate within the electrohydrodynamics is no longer as significant as in the traditional E-jet setup. First of all, the extractor rings act as a filter that partially blocks the electrostatic field interference from the substrate. The extractor ring also dominates the control of the electrostatic field around the nozzle by being the closest charged feature to the nozzle.

Some of these nozzle with electrode ring printheads have demonstrated an ability to print on non-conductive surfaces (Lee, J. S., *et al.* 2009, Lee, S., *et al.* 2008, Choi, J., *et al.* 2008, Pan, Y. *et al*, 2015). However, none of the systems were able to show high-resolution (<20μm) printed results, that is none of these prototypes were able to surpass the state of the art inkjet printer resolution. One obvious reason for their poor resolution is the feature size within these printheads. They were all designed with large nozzle tips (>100μm) and long nozzle-to-extractor ring distances (>1mm), which allows them to be fabricated easily; however, the large feature sizes limit the resolution of these printheads. Additionally, the sensitivity of these printheads to the substrate effect was never experimentally characterized; for example, there are no printing records demonstrating the use of these printheads to E-jet print onto non-conductive contoured surfaces.

1.5 Problem statement

High-resolution E-jet printing can potentially enhance the capabilities of jet-based printing technology through the improvement of resolution and expansion of printable materials. Current E-jet technology cannot be widely implemented in industry because of limited throughput and

restrictions to substrate surfaces with high flatness. This dissertation focused on resolving the following scientific questions:

Q1. Can electrohydrodynamics be utilized to enable high-resolution (<20μm), non-contact based printing onto non-conductive and contoured surfaces?

Q2. What combination of basic physics, experimental data, and numerical simulations should be utilized in the construction of practical models that can be used to study various actuation forces for ink droplet manipulation at the micro-scale?

Q3. What additional phenomena (e.g. magnetic attraction, airflow, electric-field shaping channels) could serve as complementary actuation mechanisms for controlled E-jet printing with an integrated printhead (the nozzle and ground source are combined into a single design) onto non-conductive and contoured surfaces?

1.6 Research Approach

The set of scientific questions were addressed through an iterative modeling, analysis, design and experimental testing methodology. Figure 6 shows the iteration process for this research. In each iteration, the process initiates by synthesizing experimental data, basic physics principles, and Comsol models into practical models that describe the printing behavior of various E-jet set-ups. These models directed the design and fabrication process by informing the selection of key printhead design parameters such as the dimension of feature sizes (e.g. nozzle diameters), the geometry of the features, and the allowable tolerance for positioning and orientation of the different components. These models also provided a means for predicting expected printing results based on the selection of design and process parameters. These predicted values were then validated through experimental characterization of the printhead. Based on the new experimental results, basic physics principles were used to understand the results and then update the synthesized models. These new models then provided new insights to guide the design and fabrication of a new printhead. This iterative process continued throughout the research project; enabling increasingly more accurate models of the electrohydrodynamics or other relevant physics to be generated for future reference, ensuring the generation of new E-jet knowledge, and providing an opportunity for the design and fabrication of improved E-jet printheads for more consistent, high-resolution printing.

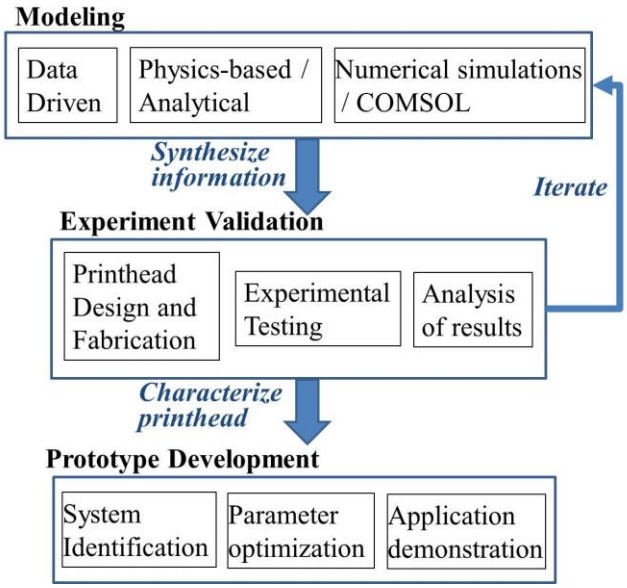

Figure 6. Schematic diagram of design and experiment iteration process

1.7 Research Project Outline

To address the scientific questions stated in subsection 2.1, we strove to achieve the following milestones (M) and deliverables (D) in the project:

M1. Demonstrate feasibility of high-resolution printing with an integrated E-jet printhead.
  D1. Construct an integrated printhead for experimental demonstration
  D2. Patent novel concepts
  D3. Disseminate work through published manuscripts
M2. Characterize the relationship between printhead design and printing behavior
  D1. Develop a flexible experimental platform to test various integrated printhead concepts
  D2. Build practical models of E-jet printing dynamics using experimental data, basic physics principles, and numerical simulations (COMSOL)
M3. Investigate the impact of alternative actuation mechanisms on E-jet printing
M4. Characterize the relationship between key parameters and printing quality
  D1. Design and fabricate prototypes of high-resolution E-jet printheads with low substrate effect sensitivity

D2. Develop a set of critical design principles based on a synthesis of experimental data and basic physics principles

D3. Disseminate work through published manuscripts

M5. Investigate the potential for high-resolution E-jet printing onto highly contoured surfaces

D1. Use the models from before to predict E-jet behavior under various design and printing conditions

D2. Design and fabricate an E-jet printhead that utilizes multiple actuation mechanisms

D3. Conduct experimental validation of printhead behavior

D4. Conduct a series of controlled experimental tests for system identification of the printhead dynamics

D5. Patent novel concepts

D6. Disseminate work through published manuscripts

The work for M1-M4 can be loosely grouped into the modeling, design, and experimental testing of three prototypes: (1) a field shaping E-jet printhead, (2) an airflow assisted E-jet printhead and (3) a Nozzle-in-Nozzle airflow assisted printhead. Within this research program, we have successfully completed the milestones and associated deliverables in M1-M5. Future research will focus on the development of an integrated multi-nozzle printhead that can print on contoured and insulated surfaces. Another future direction will be to apply the developed integrated printhead in flexible electronic printing research.

1.7.1 Field shaping E-jet printhead

The field-shaping integrated E-jet printhead provided the first demonstration of high-resolution E-jet printing onto non-conductive and contoured surfaces. This prototype and the subsequent experimental tests conducted with this printhead led to new knowledge about the physics that govern E-jet printing that was important for laying the foundation of the later prototypes. We developed a design concept that aimed to improve the basic nozzle and electrode ring E-jet printhead, which utilized two electrode plates to reshape the electrostatic field around the nozzle. The details of this design, fabrication challenges, experimental results and weaknesses of the design will be discussed in chapter 3. This work has led to the following deliverables:

Tse, L., Barton, K, (2013), "Integrated Electrohydrodynamic Jet Printing: A Flexible Deposition Approach for Micro/Nano-Manufacturing", *Proceedings of North America Manufacturing Research Conference*, Vol. 41, 1536

Tse, L., Barton, K, (2013), "Novel Printhead Design for Microfabrication using Electrohydrodynamic Jet Printing", *Proceedings of International Design Engineering Technical Conference*, Vol. 7

Tse, L., Barton, K. (2014). "A field shaping printhead for high-resolution electrohydrodynamic jet printing onto non-conductive and uneven surfaces", *Applied Physics Letters*, Vol. 104(14), 143510.

1.7.2 Airflow assisted E-jet printhead

To resolve the technical issues of the field shaping E-jet printhead, we investigated the use of new electrostatic field shapes as well as the addition of alternative actuation forces to manipulate and eject the ink droplets. Based on these investigations, we designed and fabricated an airflow assisted E-jet printhead. The working principle of an airflow assisted E-jet printhead, fabrication challenges, experimental results and limitations of the design will be discussed in chapter 4 and 5. This work has led to one conference publication, a journal article and a patent:

Tse, L., Barton, K, (2014), "Airflow assisted electrohydrodynamic jet printing: An advance micro-additive manufacturing technique", *Proceedings of Manufacturing Science and Engineering conference*.

Tse, L. and Barton, K., (2015), "Airflow assisted printhead for high-resolution electrohydrodynamic jet printing onto non-conductive and tilted surfaces". *Applied Physics Letters*, Vol. 107(5), 054103.

Tse, L., Barton, K. "An Integrated Electroyhydrodynamic Jet Printhead for Flexible Micro/Nano-Manufacturing", Patent Granted, US9415590 B2, Date of Patent: Aug. 16, 2016.

1.7.3 Nozzle-in-Nozzle E-jet printhead

To further improve the printing performance of our printhead and to create a practical design for mass production, we designed and fabricated a nozzle-in-nozzle printhead design based on our

design evaluation tool. The working principle of the nozzle-in-nozzle printhead, fabrication challenges, experimental results and limitations of the design will be discussed in chapter 5. This work will generate one journal article:

Tse, L. and Barton, K. “A new printhead design for high-resolution electrohydrodynamic jet printing onto contoured and insulating surfaces”, *Journal of Dynamic Systems and Measurement Control*, to be submitted Spring 2017.

1.8 Dissertation Outline

In this proposal, we will define the specific problem that we are tackling with the proposed research, as well as describe the particular design and characterization methodology that we will use for this work. Additionally, the proposal will introduce several printhead prototypes and discuss the significance of their corresponding experiments towards the advancement of E-jet knowledge. Future work will be discussed:

Chapter 2: An overview of the physics based evaluation tests for our printhead designs.

Chapter 3: Explains the concept of a field shaping E-jet printhead, the capability of the prototype and the knowledge generated through experimental testing with the printhead prototype.

Chapter 4: The design process, basic physics, and printing result of a novel airflow assisted E-jet printhead will be presented.

Chapter 5: The design, physics, printing performance analysis of the Nozzle-in-Nozzle integrated printhead will be discussed.

Chapter 6: Summarized the research contributions of this dissertation and provides some direction on future work.

Chapter 2

Physics Based Evaluation of Printhead Designs

For each of our design iteration, we evaluate and predict the performance of the design with two approaches: 1) Substrate sensitivity test, and 2) Alignment of force directions. The tools guide our design processes for the next iteration, they also help provide more quantitative metrics by which we can evaluate the performance of the printhead prototype.

2.1 Substrate Sensitivity Test

Reducing the sensitivity of E-jet printing to variations in substrate topography and conductivity is one of the major goals in this research project; thus, a standardized approach to evaluate the substrate sensitivity of each design iteration is necessary in this project. One of the indicators of E-jet performance is the minimum printing voltage.

$$E = \frac{4V}{d_N \ln(\frac{8H}{d_N})}. \quad (3)$$

Equation 3 is presented here again to show the relationship between the electric field intensity E and the voltage applied to the nozzle V. For conventional E-jet printheads, there is a constant minimum electric field intensity E_o for E-jet to be initiated. As the standoff height H (the distance between the nozzle tip and the substrate) increases, the corresponding minimum printing voltage also increases (see figure 7). To improve robustness in E-jet printing across varying standoff heights, the aim of an integrated printhead is to create an internal standoff height h that drives the electrohydrodynamic behavior and enables a constant applied voltage V across varying external standoff heights H between the nozzle tip and the substrate (as represented by the green "Ideal voltage range" labelled in figure 7).

For each design iteration, we will create a voltage vs. standoff height plot similar to that in figure 7. The plot for each design will be used as a substrate sensitivity test for each design.

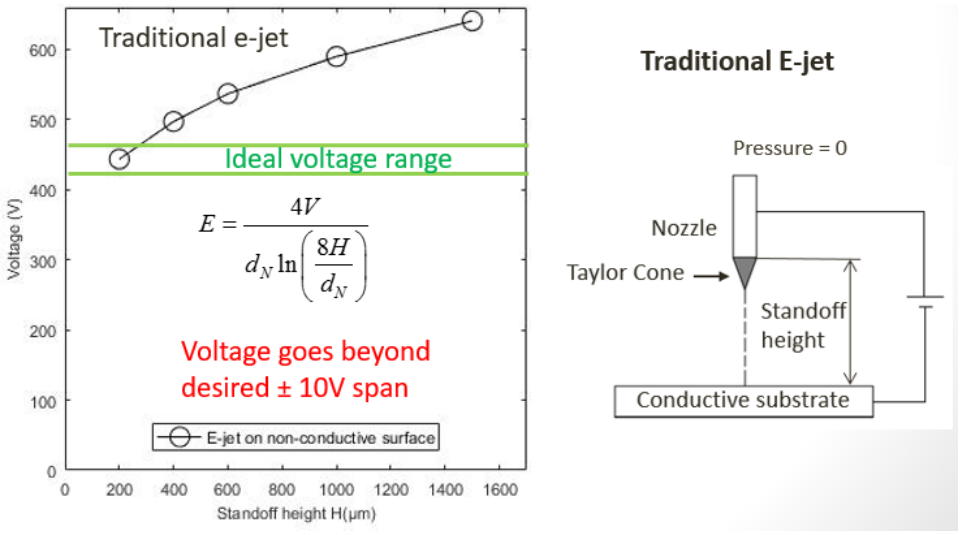

Figure 7. Substrate sensitivity of traditional E-jet.

2.2 Alignment of force directions

Besides changing the printing voltage, the profile of the substrate contour can also impact the directionality of the forces that act upon the ink droplets. This can result in scattering behavior or distortion of ink droplet trajectories. Traditional E-jet is highly susceptible to the substrate contour profile, which is illustrated in figure 8.

As shown in figure 8a, the tilted printing surface can create a misalignment between the gravity force (dotted green arrow) and the electrostatic force (red arrow), which results in the poor scattering behavior shown in figure 8b. By illustrating the different force components in each design iteration, we can predict and estimate the scattering behavior qualitatively. An ideal E-jet

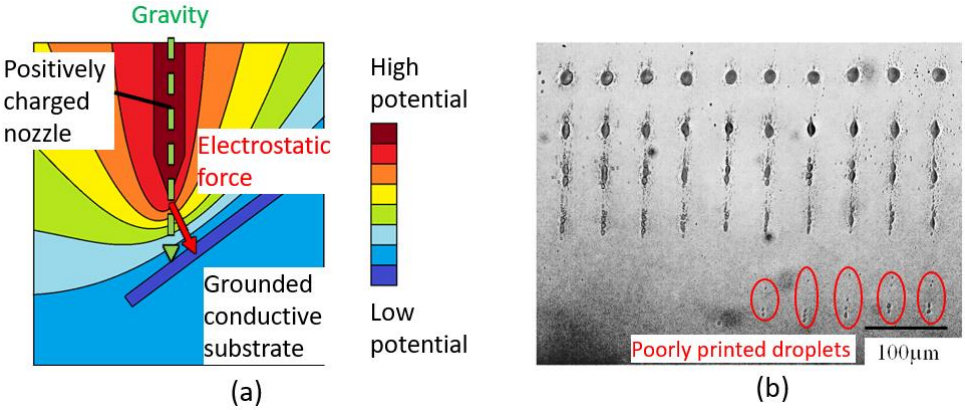

Figure 8. Force misalignment in traditional E-jet. (a) A schematic diagram of traditional E-jet printing on a tilted surface. (b) Tradition E-jet printing results on a 65° tilted surface.

printhead will have all the force components aligned in the same direction regardless of the change in substrate contour profile or electrostatic field.

By assessing the E-jet printhead designs with this evaluation tool, we aim to design an E-jet printhead that can print stably on highly contoured surfaces without exhibiting scattering behaviors or pattern distortions. Importantly, a printhead design that satisfies the design metrics outlined in this chapter will pave the way towards a multiple nozzle printhead design.

2.3 Assessment of the integrated printheads

The designs described in the subsequent chapters were evaluated using the proposed metrics. To evaluate printhead sensitivity to external standoff height variations, we conducted a sensitivity test. The objective of the sensitivity test was to find the initiating electric field intensity E across a range of external standoff heights from 200-1500μm. It is important to note that 200μm is an order of magnitude larger that traditional external standoff heights used in conventional high-resolution E-jet printing. Additionally, traditional E-jet printing exhibits significant changes in jetting dynamics over external standoff height variations on the order of 10μm, eventually transitioning outside the feasible jetting regime within a few 100μm of standoff height variation (using the same applied voltage). The aim of the sensitivity test is to identify an E-jet printhead design that is capable of printing consistently on rough surfaces (contour profile changes by 300μm or less) or highly contoured surfaces (tilted surfaces or hemispheric surfaces) without performing calibration or machine learning beforehand.

To investigate droplet directionality (a critical metric that ensures droplet placement on the desired location), we apply the force direction alignment evaluation tool. This tool identifies each individual force vector within the system (e.g. gravity, electrostatic field, airflow), and sums the vectors to resolve the true directionality of the ejected droplets. The aim of this metric is to determine the appropriate combination of forces that will result in an E-jet printhead that can print stably on highly contoured surfaces without exhibiting scattering behaviors or pattern distortions.

Chapter 3

Field Shaping E-jet Printhead

As described in chapter 1, traditional E-jet printing performance is highly sensitivity to the substrate surface roughness and materials. To mitigate the effect of the substrate on the printing, we focused our research efforts towards the development of a Field Shaping E-jet Printhead. This design concept aims to reduce the role of the substrate in the electrohydrodynamics by shaping the electrostatic field, and thereby reducing the sensitivity of the E-jet process to substrate variations.

3.1 Basic Concept of the Field Shaping E-jet Printhead

Our first concept for creating a high-resolution E-jet printhead with low sensitivity to substrate effects is to scale down the existing nozzle and electrode ring style printheads described in literature [Lee, J. S., *et al.* 2009, Kim, Y., *et al.* 2008, Lee, S., *et al.* 2008, Choi, J., *et al.* 2008]. The working principle of a nozzle and extractor design is illustrated in Figure 9. Here the extractor is illustrated as a thin plate with a hole in the center; this is closer to the geometry of our prototype. We will refer to this design as a single layer field shaping E-jet printhead (single layer FSP).

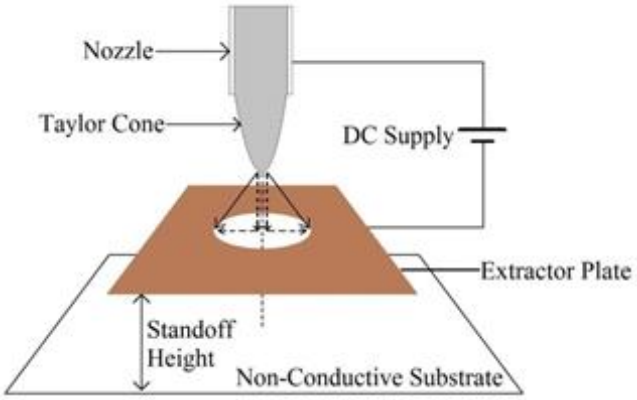

Figure 9. Schematic diagram of a nozzle and extractor ring style E-jet printhead

By charging the nozzle and grounding the extractor plate, a symmetric electrostatic field can be created when the nozzle tip is aligned directly over the center of the hole on the extractor plate. The attraction forces created by the electrostatic field pull the ink meniscus radially and down towards the inner edge of the hole on the extractor plate. A pair of these forces is shown as the solid arrows in Figure 9. Majority of the horizontal components (horizontal dotted arrow in Figure 9) of these attraction forces cancel each other. This cancellation results in a dominant vertical force (vertical dotted arrow in Figure 9) used to project the ejected droplet through the extractor hole and onto the substrate below.

According to a COMSOL simulation, when there is a small misalignment between the nozzle and the extractor hole, the electrostatic field around the nozzle tip can generate undesirable ink droplet trajectories. Figure 10(a) shows a schematic diagram of the COMSOL simulated electrostatic field within a single layer FSP and the possible radiating trajectories when there is misalignment. Since the tolerance of misalignment is very small, the chance of misalignment is very high; the ink droplets will very likely follow one of these undesirable trajectories. The ink droplets will therefore fail to flow vertically downward, which can lead to scattered printing on the substrate or even failure to pass through the extractor hole (i.e. no printed pattern).

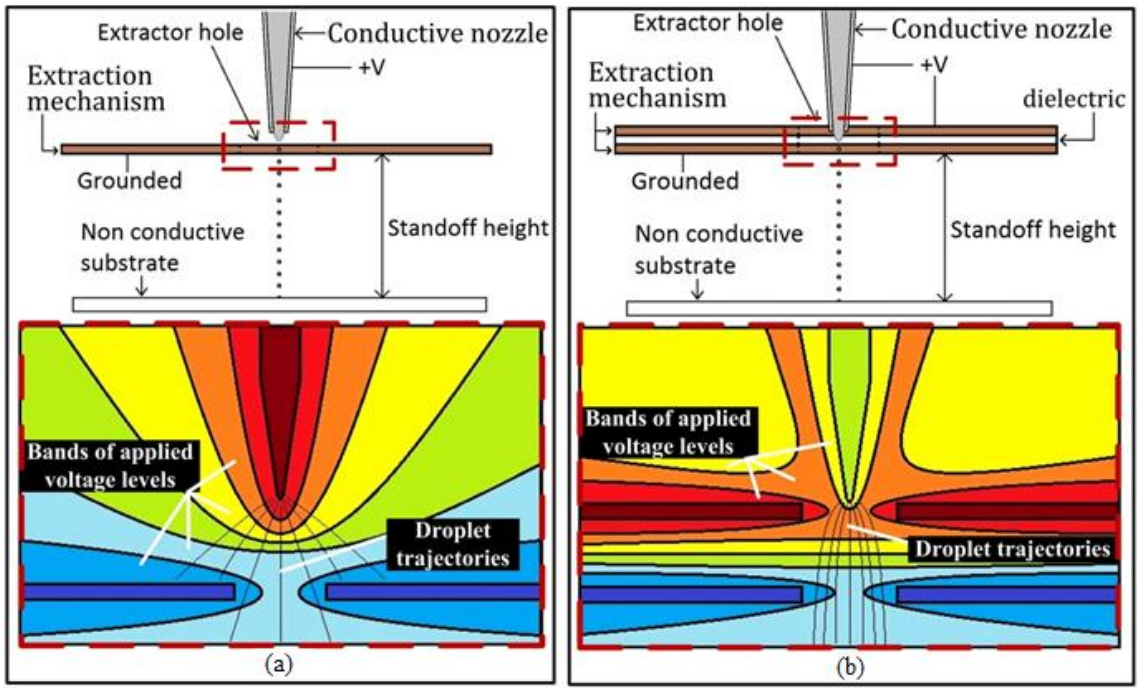

Figure 10. Schematic diagram of field shaping E-jet printheads (FSPs). (a) Single layer FSP design with resulting electric potential fields and radiating force trajectories. (b) Double layer FSP design with reduced radial force trajectories.

Our approach to mitigate this issue is to create a positively charged plate above the grounded extractor plate at the same level of the nozzle tip, which acts as a directionality controlling feature. By adjusting the potential level within this extra plate, we can reshape the electrostatic field around the nozzle; the extra plate should help to prevent ink droplets from landing on the grounded extractor plate and generate more vertical trajectories. We termed this more advance design as double layer field shaping printhead (Double layer FSP). The schematic diagram of the COMSOL simulated electrostatic field within a double layer FSP and the possible radiating trajectories are shown in Figure 10(b). The droplets are more likely to go through the two plates and land onto the substrate, and the scattering of the printed ink droplets should be reduced due to the reduction in potential curved droplet trajectories.

3.2 Printhead Design Methodology

3.2.1 Nozzle diameter - d_n

This is the most critical factor that determines the resolution of a printhead. A practical rule of thumb for nozzle diameter selection is to use a nozzle opening diameter between $2 \cdot \text{desired feature size} \leq d_n \leq 10 \cdot \text{desired feature size}$. We aimed to print sub-15μm ink droplets with our prototype, so we chose a 2μm diameter nozzle for our printhead.

3.2.2 Extractor plate thickness - *t*

The thickness of the extractor plate should be as thin as possible. The grounded plate is the feature that draws the ink material out of the nozzle, but once the ink droplet leaves the nozzle, the extractor continuous to attract the ink droplets instead of sending the ink droplets to the substrate. The thinner the extractor plate, the shorter the time duration during which the ink droplet experience this attraction force from the extractor plate after leaving the nozzle; this will result in a more vertical trajectory of the ink droplets. On the other hand, the mechanical strength of the extractor should be strong enough to sustain the distortion due to electrostatic force within the printhead. After some experimental validation, we settled for an extractor plate with a thickness *t* of 30-40 μm.

The positively charged layer in the double layer FSP should also be as thin as possible. This is because a thin, positively charged plate enables a more accurate estimation of the level of the

positive potential region, leading to a better alignment of the nozzle within the extractor plate as shown in Figure 10(b); the nozzle tip must not be above the positively charged plate or the printhead will fail to generate a meniscus and no ink droplets will be drawn out from the nozzle.

3.2.3 Extractor hole diameter - *R*

The extractor hole design was driven by three aspects: (1) reduction of radial attractive forces; (2) nozzle and hole alignment accuracy; and (3) clogging issues. While smaller holes mitigate radial forces, they increase misalignment and clogging issues.

As mentioned in section 3.1, a small misalignment of the nozzle away from the center of the extractor hole can create undesirable ink droplet trajectories; the ink droplet is very likely to attach to the extractor plate instead of landing on the substrate when misalignment happens. Therefore the extractor hole should not be too small, or it will be very hard to stay within the misalignment tolerance. The nozzle to extractor hole alignment system we developed has a position accuracy of ~±5μm, and we want to have <5% misalignment from the center of the hole relative to the hole diameter; as such, we aim to create an extractor hole $\geq$ 100μm.

When there is disturbance or misalignment, the released ink may land onto the edge of the extractor hole and partially clog the hole. As time progress, more ink accumulates at the edge of the extractor hole and may eventually clog the hole. An extractor hole $\geq$ 100μm will help to reduce the risk of clogging.

Based on these considerations, the projections of our models, experimental testing, and fabrication tools, we selected the final extractor hole diameter to be 120μm.

3.2.4 Nozzle to extractor plate distance - *h*

In a traditional high-resolution E-jet setup, the regular distance between the nozzle and the grounded substrate has been optimized at around 30μm. We therefore design the distance between the nozzle and the grounded extractor plate to be between 30-80μm for similar jetting results.

3.3 Printhead Fabrication

A major consideration in the printhead prototype design process is reconfigurability. This is due to the necessity to replace features within a printhead over time. A nozzle with an opening diameter

of 2μm usually clogs within 2 days; therefore, a printhead that does not allow nozzle replacement has a life span of ≤ 2 days. The extractor plate faces a similar issue; once the extractor has been wetted by the ink due to misalignment and disturbances that change the trajectory of the ejected material, the extractor plate must be replaced.

As there are always fabrication tolerances across any product, the nozzle and extractor plate must be realigned after replacement. A reconfigurable printhead that allows for position adjustments of both the nozzle and the extractor plate should be constructed to ensure flexible design configurations and reduced downtime during repair. The reconfigurable integrated printhead fabricated in this work consists of three major components: the nozzle, the extractor plate, and a high-resolution alignment system (see Figure 12).

3.3.1 Nozzle preparation

The nozzles we use are glass nozzles with 2μm opening diameter; we purchased them from World Precision Instruments, Inc. The glass nozzles are then sputtered with gold, so that we can charge the ink materials within. Finally, the nozzle tips are coated with a layer of hydrophobic coating to prevent ink from wicking up along the outer surface of the nozzle rather than staying at the nozzle tip.

3.3.2 Extractor plate

The extractor plate is a thin plate (30-40μm thick) with a small hole (~120μm diameter) in the middle of it. While MEMS and laser cutting are high-resolution feature fabrication techniques, the high costs and long times associated with these processes preclude their use for extractor plate manufacturing. As such, a traditional machining approach was selected for the extractor fabrication.

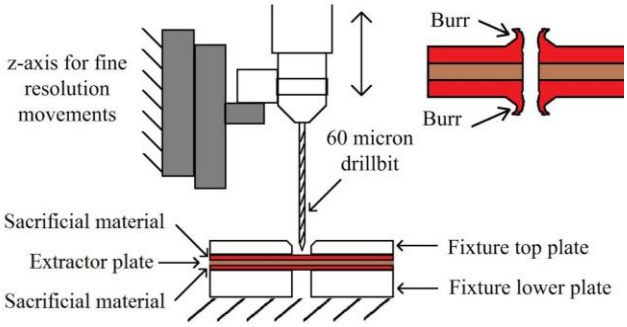

Figure 11. Extractor drilling process.

Creating a small hole in the extractor plate by drilling into an extractor material directly creates burrs around the two ends of the drilled hole, which leads to irregularity in the electrostatic field and poor functionality of the integrated printhead. To prevent burrs from forming around the

drilled hole, sacrificial materials are placed on top and below the extractor material, and then all 3 layers of material are fixed to the working platform of the high speed drill press using the custom made fixture tool. With the sacrificial layers in place, the burrs form around the opening at the top and bottom surfaces of the two sacrificial materials, but not on the extractor materials (see Figure 11 for a schematic diagram of the drilling process).

The extractor plate for the single layer FSP is made with a 30μm thick copper foil. The hole in the center of the copper foil is created with a 120μm diameter drill. The extractor plate for the double layer FSP is made with a 35μm thick polyimide film. The top and bottom surfaces of this polyimide film were sputtered with gold and then the hole in the center of the polyimide film is again created with a 120μm diameter drill. The gold layer sputtered on the top will be positively charged while the gold layer sputtered at the bottom will be grounded.

3.3.3 High-resolution alignment system

The most common approach to align the nozzle and the extractor plate is to monitor their position with a high-resolution camera, and then adjust the relative positions with high-resolution linear stages. Due to space and cost constraints, we only have one high-resolution camera to monitor the

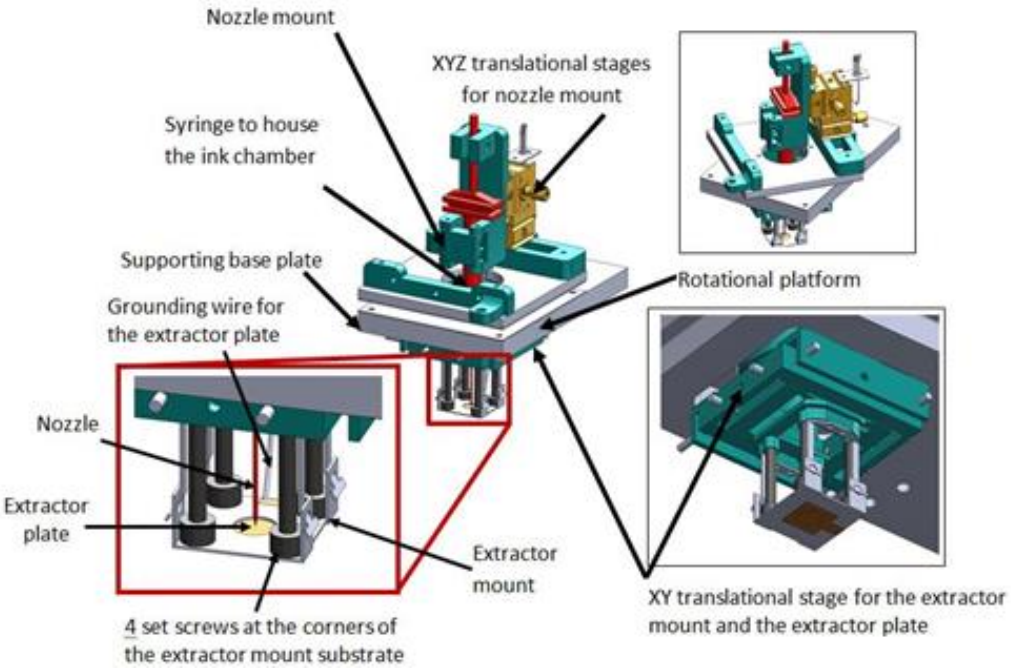

Figure 12. CAD drawing of the high-resolution alignment system

two microscopic features. As such, we are not able to view both X and Y directions of the setup, making it very challenging to align the nozzle and the extractor hole in all XYZ directions.

To address this, we created an alignment system on a rotational platform, which allows the nozzle and extractor plate to rotate 360º within the camera view, enabling X and Y axis positioning of the nozzle and the extractor plate. As shown in Figure 12, the nozzle and ink supply (colored red) are held in place by the nozzle mount. The nozzle mount is attached to an XYZ manual translational stage installed on top of a rotational platform (see the rotated image in Figure 12). The rotational platform allows the user to rotate the setup and align the system along the axis of rotation.

Attached to the bottom of the rotational platform is another translational stage. This manual stage allows the user to adjust the XY position of the extractor mount and the extractor plate within the camera view and along the axis of rotation. With this alignment system, the nozzle and extractor plate can be aligned with a position tolerance of ±5μm, and both the nozzle and the extractor can be replaced when necessary.

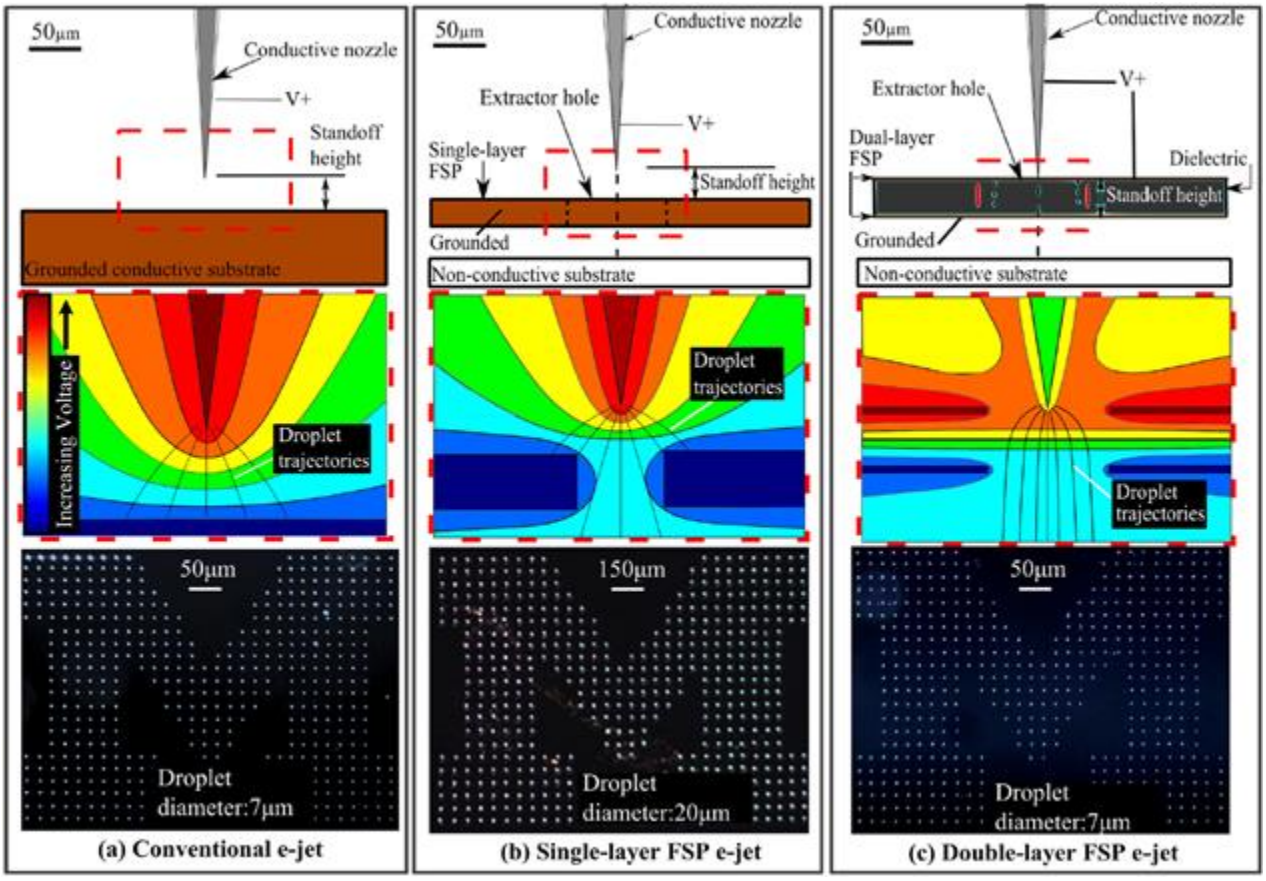

Figure 13. Block M patterns printed under different conditions

Table 1. Printing conditions of the FSP printed results

Block M images	Ink	Nozzle-ground offset (µm)	Baseline voltage	Peak voltage	Printing mode	Feature size (µm)	Substrate type
Conventional	NOA 81	30	200V	370V	Pulse	7 stdev:0.4	Conductive
Single layer FSP	NOA 81	30	290 V	500V	Pulse	20 stdev:1.8	Non-conductive
Double layer FSP	NOA 81	50	100 V	430V	Pulse	7 stdev:0.6	Non-conductive
Spiral block	Ink	Nozzle-ground offset (µm)	Baseline voltage	Peak voltage	Printing mode	Feature size (µm)	Substrate type
Double layer FSP	Silver	50	265V	n/a	DC	5.4 stdev:1	Non-conductive
Contoured image	Ink	Nozzle-ground offset (µm)	Baseline voltage	Peak voltage	Printing mode	Feature size (µm)	Substrate type
Double layer FSP	NOA 81	50	405V	n/a	DC	34 stdev:4	Non-conductive

Design concepts, corresponding electric field shaping, and printed patterns for conventional (conductive nozzle and substrate), single-layer FSP, and dual-layer FSP E-jet set-ups are given in Figure 13. The electric field shaping images are based on simulations performed in COMSOL. The simulated droplets were modeled as point masses corresponding to a 1µm diameter spherical water droplet with no volume. The models assumed symmetric geometries, applied gravity, negligible air drag, and no surface tension. To evaluate trajectory variations due to nozzle and extractor plate misalignment, droplet trajectories were simulated from different starting positions around the Taylor cone.

3.4 Experimental results

The *generalizability* and *controllability* of the field-shaping designs were evaluated through printing demonstrations with a UV curable adhesive (Norland Optical Adhesive 81) and silver nanoparticle suspension onto non-conductive substrates, including a substrate with significant height variations. Experimental parameters for the different demonstrations are provided in Table 1. Optical measurements of droplet size and spacing within the printed patterns were used to examine the controllability of the dual-layer FSP.

A pulsed voltage input was used to modulate the droplet release for the UV curable adhesive to achieve controlled block M patterns (Figure 13). For the dual-layer FSP design, the top conductive layer and the nozzle were positively charged, while the bottom conductive layer was grounded. These results demonstrate controlled **sub 10µm** feature sizes with a non-conventional E-jet system design.

Quantitative measurements of the ink droplet diameter, standard deviation, and registration accuracy of dual-layer FSP E-jet printing are comparable to conventional E-jet printing (Figure 14). Coefficient of variation (CV) values are provided in Figure 14, $c_v = \sigma/\mu$. For the block M patterns in Figure 13, CV values for the droplet diameters are 0.05 (conventional printing), 0.09 (single-layer FSP) and 0.08 (dual-layer FSP); droplet spacing CV values are 0.07, 0.09, and 0.1, respectively. CV values and average droplet diameters for the dual-layer FSP lie well within the range of values determined for conventional E-jet printing (Barton, K., *et al.,* 2011, Korkut, S., et al., 2008), and greatly surpass performance capabilities of ring electrode printing in literature (Lee, S., et al., 2008).

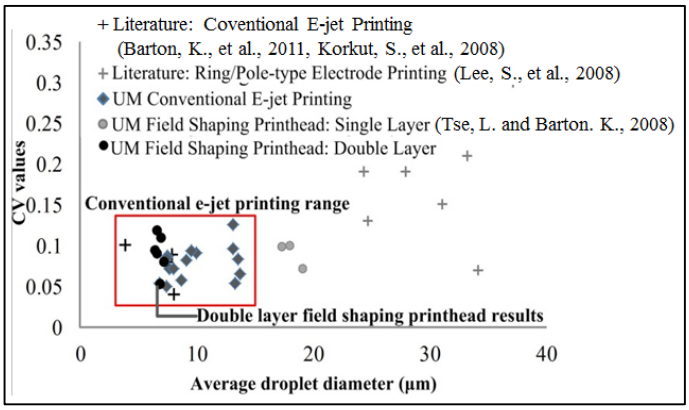

Figure 14. Comparison of printed dimensional accuracy for conventional and pole/ring electrode type printheads.

The dual-layer FSP was also used to print a silver pattern onto a flat, non-conductive glass slide; Figure 15(a). This silver pattern shows a **sub 10µm** silver line continuously printed onto a non-conductive surface without the aid of a grounded substrate. The printed lines have a line thickness CV value of 0.18. Average line width is ~5µm, on par with conventional E-jet printing of silver lines onto conductive substrates (Park, J. U., *et al.,* 2007).

The final demonstration illustrated the **controllability** of the FSP design in the presence of significant topographical variation. The ability to achieve controlled printing onto height varying

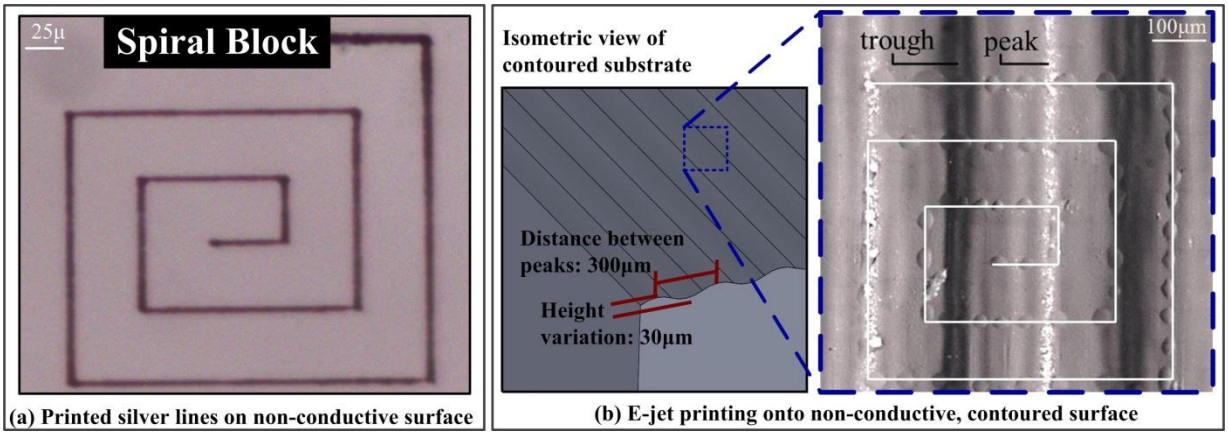

Figure 15. Dual-layer FSP printed patterns. (a) Silver lines printed onto non-conductive surface. (b) Droplet pattern printed onto a non-conductive, contoured surface.

surfaces is key to enabling generalizable 3D printing because layer-to-layer printing will introduce significant topographical variation. The non-flat, non-conductive substrate was fabricated with a Stereolithography machine using Accura60 polymer to create a wave pattern with 30μm height variations across 300μm, Figure 15 (b). Commercially available glass slide flatness variability is approximately ±6μm per inch (Handran, C. Wang, and D. Aziz, 2001), which is ±0.06μm across 300μm; *3 orders of magnitude* less height variability than the substrate used in this demonstrative experiment. NOA 81 was printed onto the surface using a constant applied voltage of 405 V to the nozzle and the top conductive FSP layer, and a grounded bottom layer. The printed pattern (Figure 15. (b)) resulted in a droplet diameter CV value of 0.13 for average droplet diameters of 34 microns. For comparison, consider the 2μm standoff height variation applied in (Barton, K., *et al.*, 2011) that resulted in a 75% reduction in jetting frequency. Applying the process maps from (Barton, K., *et al.*, 2011) and the scaling laws from (Choi, H. K., *et al.* 2010), this standoff height variation could result in a CV value as high as 0.61; more than *4.5 times larger variation* than that exhibited in the printed pattern in Figure 13(b). These results verify controlled E-jet printing onto a surface with significant height variations; indicating a substantial reduction in E-jet printing sensitivity to varying heights as a result of integrating the dual-layer FSP into the E-jet system. While the sensitivity has been reduced, substrate influence has not been entirely eliminated. For the FSP design presented here, substrate height variatios greater than 30μm resulted in poor printing quality (CV values larger than 0.3).

3.5 Deficiencies of Field Shaping E-jet Printhead

To summarize, a dual-layer field shaping E-jet printhead design enabled an array of printing demonstrations with a variety of materials and substrates. The new knowledge obtained from this work, as well as the capabilities demonstrated with this FSP design provide the foundation for future integrated E-jet printhead designs. Despite the success of this initial prototype, there are several deficiencies within the design that make it ineffective for practical use. First of all, the printhead does not mitigate the substrate effect as much as would be desirable; FSP can only print at low standoff heights (<60μm) or under small standoff height variation. The role of the substrate is relaxed but not to a great extent. When the standoff height is < 60μm, the substrate surface becomes polarized and impacts the electrohydrodynamics; the substrate aids in drawing the ink droplets down towards the substrate surface, thereby resulting in successful E-jet printing. When

the standoff height is > 60µm, the polarization effect weakens. As a result of the weakened polarization, the ink droplet size becomes significantly more variable (resulting in a > 30µm printing resolution) and may result in the printing stopping completely. This variation is a direct result of the remaining substrate effects.

Another drawback of the FSP design is the low tolerance for nozzle-to-extractor plate misalignment and poor disturbance rejection. This is due to the unique shape of the electrostatic field that results from the FSP design. Figure 16(b) shows a 3D schematic diagram of the electrostatic field in which the z axis represents the electric potential level, and the XY plane corresponds to the geometric space. We can draw an analogy between the electric potential field and the gravitational potential field in Figure 16(b); the ink droplet is pulled down from the high potential region towards the low potential region. Although the force applied to the droplet induces a downward trajectory, the specific pathway through the field is not specified by the FSP design. Since the pathways (potential droplet trajectories) are neutrally stable, there is no incentive for the droplet to select path 1 versus an alternative path such as path 2. Additionally, the electrostatic field radiates away from the nozzle opening (as seen in Figure 10). Consequently, the potential for droplet scattering is

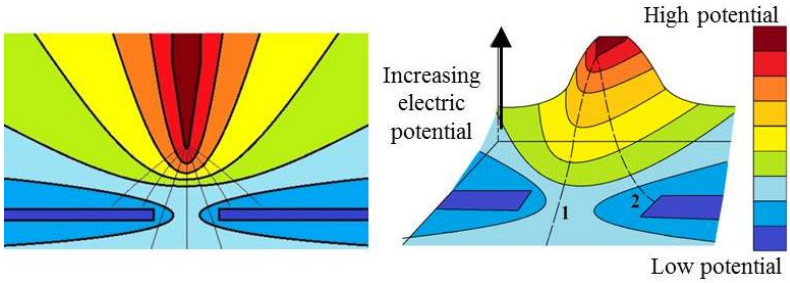

Figure 16. Single-layer FSP electrostatic field: (a) 2D schematic diagram of electrostatic field. (b) 3D representation of electrostatic field.

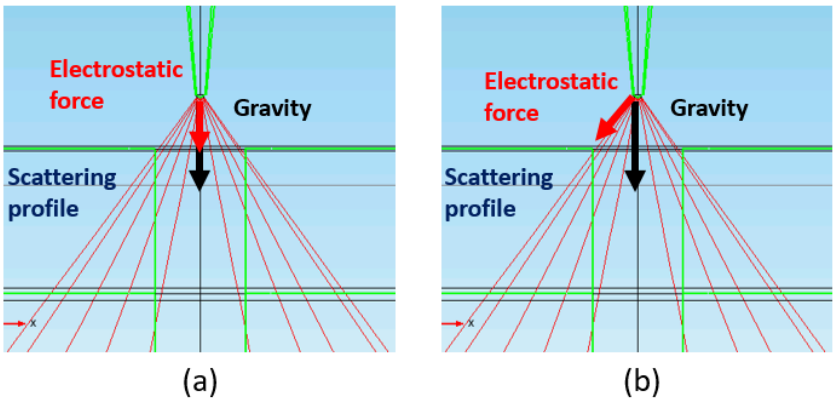

Figure 17. Misalignment of force directions in a FSP. (a) Electrostatic force aligns with the gravity force when standoff height is less than 60µm. (b) Electrostatic force and the gravity force are misaligned when standoff height is more than 60µm.

significantly higher than the desired design specifications. This can also be presented by Figure 17, which shows a misalignment between the electrostatic force and the gravity at a standoff height of more than 60µm. This behavior was observed experimentally. Figure 18 shows a dot matrix printed with a poorly tuned single layer FSP resulting in a dot matrix composed of scattered ink droplets. The red dots represent the desired droplet placement, while the printed results demonstrate the scattered printing.

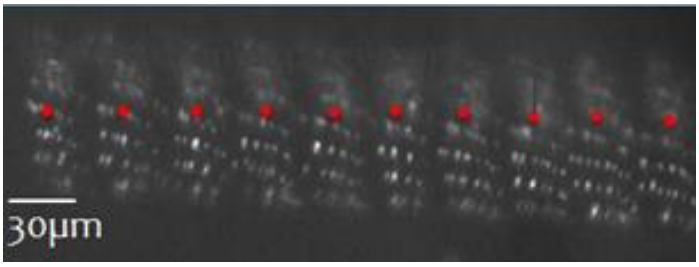

Figure 18. Scattered printing with single layer FSP

Lastly, the design is not easily reproducible, making process characterization printhead dependent. The small features sizes within the printhead combined with the precise design requirements makes even a relatively small modification or change amplified from the process performance standpoint. Given these design challenges, as well as alignment issues due to limited visibility of the printing process while using the dual-layer FSP, a modified printhead design must be considered.

New knowledge: Although this list of deficiencies led to the need for a modified design, there were several important breakthroughs that were key to making the design leap presented in the next chapter.

1. A rotatable alignment system is an effective approach for creating a high-resolution and re-configurable E-jet printhead prototype.
2. Uniformity in the shape of the electric field is paramount in creating a uniform meniscus and droplet trajectory.
3. Electrically charged plates in various positions can be used to alter the shape and directionality of the ejected droplets.
4. An alternative extraction mechanisms (other than a grounded substrate) can be used for high-resolution E-jet printing.
5. At low standoff heights (< 200µm), the substrate effect is very strong for both conductive and non-conductive substrates unless the substrate is shield from the printhead with a grounded feature.
6. In order to relax the nozzle alignment tolerance, extra actuation forces should be considered to guide the ink droplet towards the substrate and away from the extractor feature.

Chapter 4

Characterization and Understanding of Jetting Dynamics

Building from the knowledge obtained from the FSP designs, this chapter will discuss the exploration of additional actuation forces to drive the directionality of the ejected droplets, and the introduction of an airflow assisted, electrohydrodynamic jet printing process.

4.1 Exploration of Different Actuation Forces for Ink Droplet Deflection

Learning from the FSP design, we understand that the use of an extractor will lead to the attraction of released ink droplets towards the extractor instead of the substrate; therefore, we consider the introduction of additional ejection or directionality forces to re-direct the ink droplets away from the extractor after they are released from the nozzle. We investigated three possible redirecting approaches: (1) using electrostatic force to re-direct the ink droplets (create new FSP with a different electrostatic field shape), (2) incorporate magnetic force into the printhead, and (3) incorporate airflow into the printhead. In this section we will explain our findings from our preliminary research of these concepts.

4.1.1 Electrostatic Force

As mentioned in chapter 3, the nozzle alignment tolerance of the FSP designs is very small and therefore very hard to achieve. We aimed to mitigate this issue by creating a flexible printhead testbed that could modify the position and location of various electrostatic force conductors to test the idea of an adjustable electrostatic field. Figure 19 shows a schematic diagram of the flexible testbed.

In this testbed, a polymer ribbon sputtered with gold on the top surface is tilted and suspended in air with a ribbon extractor mount. A second polymer film with a gold sputtered surface is attached to a 150µm thick glass slip, which in turn is attached to a regular glass slide. The glass slip acts as a spacer between the polymer film and the regular glass slide. The regular glass slide can be adjusted in the XY position. The nozzle is placed above the edge of the gold sputtered polymer film, while the lower edge of the ribbon is positioned next to the nozzle tip.

During experimental testing, we grounded the nozzle and positively charged the gold sputtered top surface of the polymer film so that ink droplets were released onto the edge of the polymer film electrohydrodynamically. Therefore, the polymer film serves as an extractor that draws ink droplets out of the nozzle. We then charged the suspended polymer ribbon positively with an adjustable voltage source. This allowed us to adjust the electrostatic field shape according to the ink droplet deposition behavior in real time.

Theoretically, the polymer ribbon with the adjustable voltage level should act as an ink droplet deflector; when the potential level in the polymer ribbon reached a certain level, the attraction force upon the released ink droplets from the polymer ribbon should pull the ink droplets away from the edge of the polymer film towards the regular glass slide beyond the edge of the polymer film.

Experimentally we observed poor printing results from this set-up. When the voltage level at the polymer ribbon was too low, the ink droplet trajectories were unchanged and the droplets continued to land on the edge of the polymer film. Alternatively, when the voltage level was high

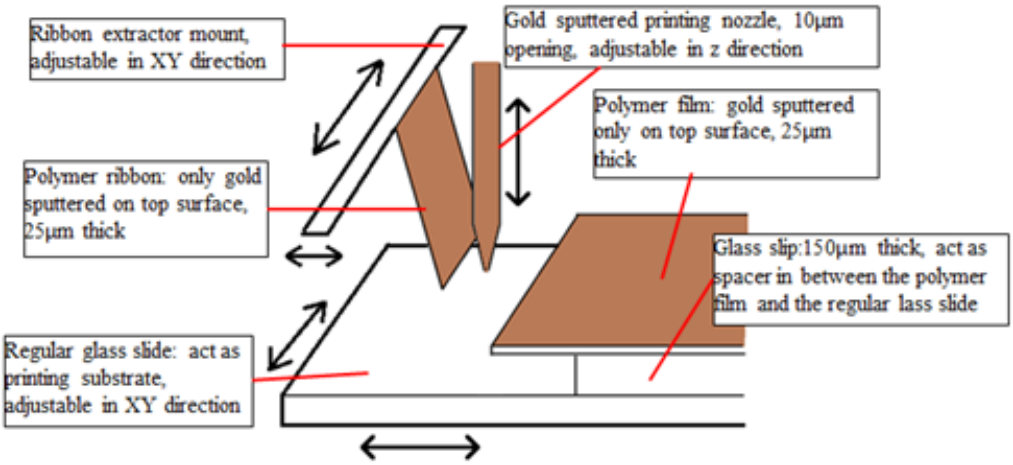

Figure 19. Schematic diagram of an adjustable FSP testbed

enough to re-direct the ink droplets away from the edge of the polymer film, the ink droplets landed on the regular glass slide in a highly scattered pattern (similar to a spray form). If the voltage reached an even higher level, the ink droplets landed on the polymer ribbon instead of the glass slide or the polymer film.

New knowledge: From this work, we determined that the use of large planes (sheets) to control the electrostatic force and redirect ink droplet trajectories was not suitable for controlled printing.

4.1.2 Magnetic Force

This concept was inspired by mass spectrometers, in which ion particles are accelerated by an electrostatic field, and then deflected with a magnetic field. According to the Lorentz force law, the magnetic force acting upon a traveling charged particle in an accelerating electric field is:

$$F = Q(E + v \times B) \tag{6}$$

where F is the force applied to the charged particle, Q is the amount of charge in the particle, E is the electric field, and v x B is the vector cross product of the charged particle velocity and magnetic field.

Figure 20 shows a schematic diagram of an electrically charged particle curving due to magnetic force. In this figure, a positively charged particle on the left is electrically attracted by a negatively charged feature on the right, inducing the particle to traverse from left to right with a certain velocity. The introduction of a magnetic force causes the particle to curve away from the original trajectory.

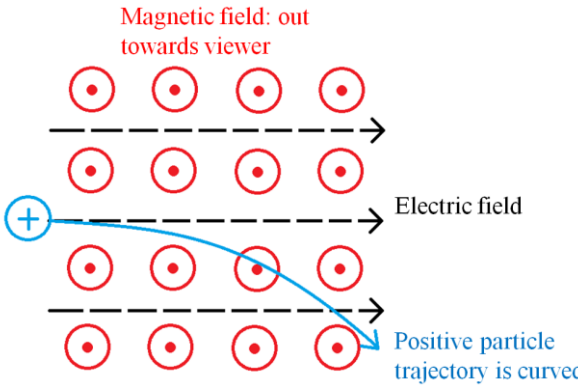

Figure 20. Schematic of a curved charged particle trajectory due to the magnetic and electric fields

Following this concept, theoretically one would expect that the introduction of a sufficiently strong magnetic force within the set-up of an integrated E-jet printing system, when the ink droplet is generated electrohydrodynamically with a grounded extractor instead of a grounded substrate surface, would redirect the ink droplet away from the extractor and towards an alternative surface.

In this manner, the droplet trajectory could be controlled such that droplets land onto the desired surface.

In practice, the magnetic field strength required to deflect the ink droplet is extremely strong. Revisiting equation (6), we can understand that the force acting upon the ink droplet depends highly on the velocity of the droplet. The velocity of an E-jet ejected droplet is slow when compared to the ions in a mass spectrometer; ion velocity approaches the speed of light. Another factor to consider is the traveling distance of the ink droplet. The longer the traveling distance, the more time during which the magnetic force can create a deflection. Since the distance between the nozzle and the substrate is usually < 3mm, which is very short in comparison to the ion traveling distance in a mass spectrometer (>100mm), a minimum deflection force would be expected with a magnetic force. The last factor to consider is air drag. In a mass spectrometer, the ions travel in a vacuum with little to no resistance; ink droplets ejected from an E-jet system travel in air, and therefore, they are subjected to air drag that limits the impact of the magnetic force on the droplet trajectories.

To verify the deflection behavior due to a magnetic field, we placed an ultra-high-pull neodymium-iron-boron magnet in close proximity to an E-jet nozzle (< 500μm), and monitored the change in droplet landing location as a function of magnet position. These test resulted in insignificant changes to the droplet landing location.

New knowledge: Deflection of the droplet trajectory due to magnetic force is minimal due to the relatively slow speeds and short distances over which the droplets must traverse.

4.1.3 Airflow

The major concern for using airflow as an ink droplet redirecting agent is its lack of controllability. As an air jet is released from a nozzle, the air mixes with the ambient air and

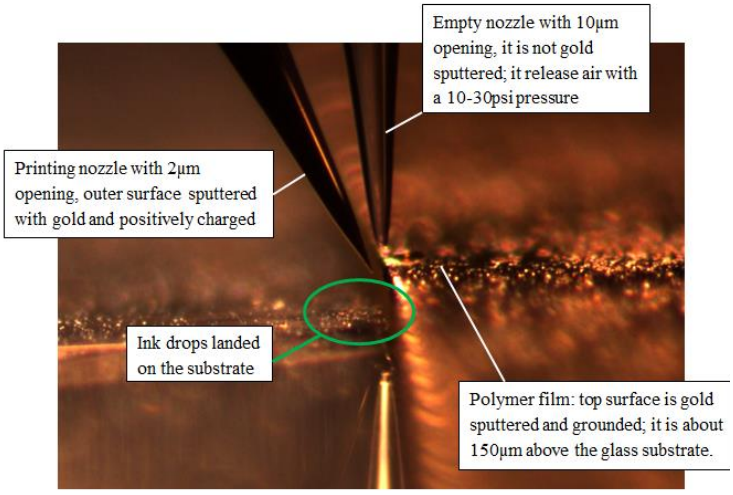

Figure 21. Testbed showing droplet deflection with airflow

creates turbulence, which leads to inaccurate and unpredictable behaviors. Our approach to control the air flow is to use a microscopic nozzle so that the turbulence and mixing of the air will happen at the microscopic scale.

Our initial testbed is shown in Figure 21. The goal of this initial set-up was to investigate the feasibility of using airflow to alter the in-flight trajectory of E-jet ejected droplets. In this testbed, we attached a polymer film onto a 150μm thick glass slip, which in turn was attached to a glass slide that served as the substrate (same arrangement as the polymer film shown in Figure 19). The printing nozzle is positively charged, while the polymer film is grounded; airflow is then released from the non-conductive glass nozzle with a pressure ranging from 10-30psi. It was observed that the ink droplets only traverse to the glass substrate when airflow is applied, thus validating the effectiveness of air as a deflecting mechanism. These early experimental results served as the baseline for future designs that incorporate airflow into the E-jet printhead design.

4.2 Hybrid E-jet Printhead: Airflow Assisted E-jet Printhead with 2 Nozzles

Leveraging the knowledge we gained during the experimental testing with the airflow assisted design presented in 4.1.2, as well as our understanding of the importance in generating a uniform electric field, a two nozzle airflow assisted E-jet printhead was investigated.

4.2.1 Basic Concept of Airflow Assisted E-jet Printhead with 2 Nozzles

Figure 22 provides a conceptual illustration of an airflow assisted E-jet printhead. The two key components within the design include a conductive nozzle that contains the ink material (printing nozzle) and a conductive nozzle that enables airflow through the orifice (extractor nozzle). In the set-up provided in Figure 22, the extractor nozzle serves as the actuation mechanism. Meniscus generation and ejection are driven by an electric field generated through the interaction between

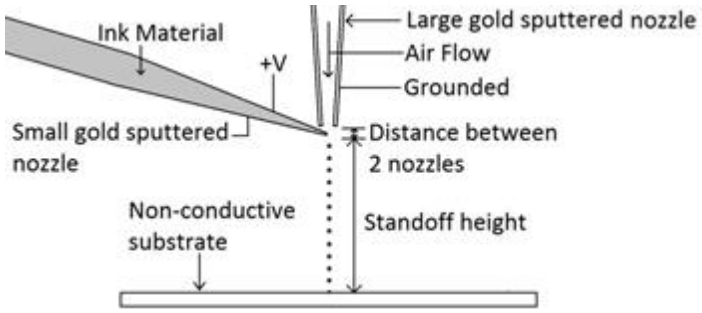

Figure 22. Schematic diagram of an airflow assisted E-jet printhead with 2 nozzles

the grounded surface of the extractor nozzle and the positive voltage applied to the printing nozzle. As the droplet releases from the meniscus, the electric field draws the material towards the surface of the extractor nozzle. At this point, airflow from the extractor nozzle redirects the droplet trajectory from the extractor towards the substrate.

Several important process parameters dictate the printing behavior of an airflow assisted E-jet printhead (given in Table 2). The design process for these parameters requires a systematic approach in which the individual design decisions are a function of application, functional requirements, and basic physics of the air assisted E-jet process.

4.2.2 Printhead design methodology

This section provides a step-by-step design methodology for airflow assisted E-jet printhead design.

Step 1: Determine printer nozzle diameter d_N based on the desired resolution of the individual features within the printed pattern. The diameter should lie within the range: 2• feature size < d_N < 10• feature size.

Step 2: Determine d_E as a tradeoff between electrostatic behavior and fluid dynamics of the airflow. A large extractor nozzle tip generates a strong electrostatic field, mitigating process sensitivity to substrate disturbances. However, as d_E increases, the airflow from the extractor nozzle increases, leading to unnecessary turbulence and displacement of printed droplets on the substrate. Therefore, the selection of d_E should balance the tradeoff between scattering due to substrate effects and droplet displacement due to airflow. For high-resolution printing (<15μm features), a good starting point is d_E =30μm.

Table 2. Airflow assisted E-jet with 2 nozzles process parameters

Parameter	Description
d_N	Printing nozzle diameter
d_E	Extractor nozzle diameter
V	Applied voltage
P_E	Air pressure supplied to extractor nozzle
α	Tilting angle of printing nozzle
h	Standoff height between printing and extractor nozzle tips
H	Relative offset height between printing nozzle and substrate

Step 3: Determine the tilting angle α for the printing nozzle. The angle is determined by the direction of the electrostatic force that drives the ink within the airflow assisted E-jet printhead. In a traditional E-jet setup (Figure 23 (a)), the printing nozzle is oriented perpendicular to the substrate, directing the electrostatic force and the droplets vertically towards the substrate. However, if the printing nozzle within the airflow assisted E-jet printhead is oriented with a very small angle α to avoid physical contact of the two nozzles (Figure 23 (b)), the electrostatic force will draw the ink material towards the inner wall of the printing nozzle (in the direction of the black arrow illustrated in Figure 23 (b)). This force does not draw ink material to the nozzle opening, and therefore, no Taylor Cone will be generated, and hence no ink material will be released. Although a perpendicular orientation between the printing and extractor nozzle may seem ideal (Figure 23 (c)), the asymmetry of the electric field leads to poor meniscus generation and satellite droplets breaking off from the main droplet. The different charge-to-mass ratios of these satellite droplets will result in the satellite droplets traversing along a trajectory that aligns with the electrostatic force (different trajectory paths in Figure 23 (c)). As such, the printing nozzle tilting angle is a tradeoff between minimizing the satellite droplet scattering and ensuring the directionality of the electrostatic force to create a proper meniscus for jetting. For the printhead used in this work, the printing nozzles were oriented at an angle of 60º (from vertical).

Step 4: Determine the relative position of the printing and extractor nozzles as a function of electrostatic field and airflow. A good starting value for electrostatic field generation is $h \approx 10 \cdot d_N$. For $h << 10 \cdot d_N$, the released ink droplet will be strongly attracted to the extractor nozzle, requiring an increase in airflow which could lead to printed pattern deformations. For $h >> 10 \cdot d_N$, substrate

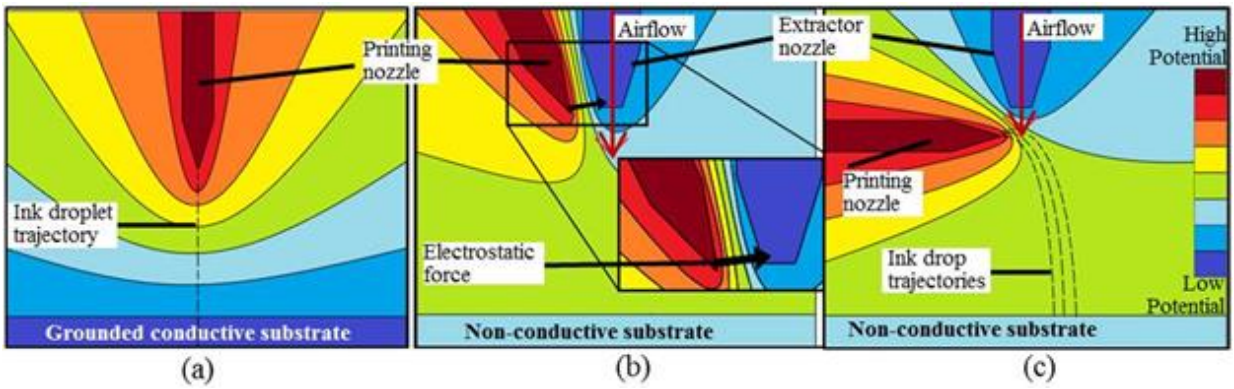

Figure 23. Schematic diagrams of droplet trajectories in airflow assisted E-jet printhead. (a) Airflow assisted E-jet printhead with 2 nozzles aligned tangentially. (c) Airflow assisted E-jet with horizontally oriented printing nozzle.

interference may dominate the electric field generation, resulting in increased sensitivity to substrate variations.

Another important consideration of the relative position is the airflow dynamics from the extractor nozzle. Figure 24 shows a schematic diagram of fluid flow out of a nozzle based on established models in the literature (Albertson, M. L., *et al.*, 1950). From Figure 24, the potential core represents a region where the airflow remains steady and the velocity of the air is the same as the airflow velocity at the nozzle exit. The mixing layer outside the potential core is where the ambient air (in the form of entrainment) mixes with the air released from the nozzle. As shown in Figure 24, the mixing layer expands towards the center axis of the nozzle, along the fluid flow, ending the potential core at a distance of ~4-6 times the extractor nozzle diameter away from the nozzle opening.

While $h \approx 10 \cdot d_N$ is a good distance for the electrostatic field, the location of the nozzle tip within the airflow must be considered carefully. If the printing nozzle is located $10d_N$ away from the extractor nozzle tip **inside the potential core region**, the printing nozzle tip disrupts the potential core, leading to asymmetric air mixing and significant droplet scattering. If the printing nozzle is $10d_N$ away from the extractor nozzle tip **outside the mixing layer in the entrainment region**, the entrainment will be too weak to redirect droplets into the mixing region and result in released droplets landing on the outer surface of the extractor nozzle rather than the substrate. Based on the electrostatic field and airflow dynamics, we have determined that the optimal position of the

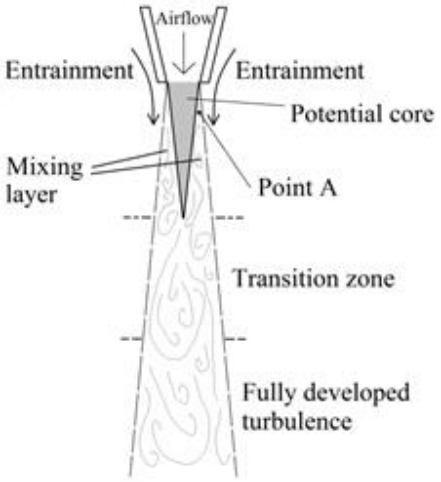

Figure 24. Schematic diagram of sub-sonic fluid flow out from a nozzle (2 nozzle printhead)

printing nozzle tip is $h = 10 \cdot d_N$ under the extractor nozzle tip **within the mixing layer between the entrainment and potential core**. This location is denoted as point A in Figure 24.

Step 5: Determine P_E for optimal airflow dynamics. The optimum level of P_E is the smallest air pressure necessary to redirect the ink droplets away from the extractor nozzle and towards the substrate. High P_E values lead to droplet scattering and the displacement of printed material on the substrate. Start with P_E at the lowest pressure setting for the given system, increase until droplets are redirected onto the substrate.

4.2.3 Experimental Results

To understand the significance and physical meaning of the experimental results, here we will provide a brief recap of section 1.3.6.

As provided in equation (5) and restated here, the ink releasing rate for electrohydrodynamically driven droplet ejection can be estimated by the following equation according to Chen *et al.* (2008):

$$Q \approx \frac{\pi d_N^4}{128 \mu L}\left(\Delta P + \frac{1}{2}\varepsilon_o E^2 - \frac{4\gamma}{d_N}\right).$$

From (5), it is clear that ink material in the nozzle will flow (Q positive) and be released from the nozzle when the ink - air pressure difference (ΔP) and the electrostatic field (E) exceed the resistance due to the capillary pressure ($4\gamma/d_N$). In most of our experiments, no back air pressure is supplied into the ink chamber during printing; thus, E-jet printing will only happen when the electrostatic field (E) overcomes the capillary pressure ($4\gamma/d_N$). Notice $4\gamma/d_N$ is a constant once the nozzle diameter and ink material are chosen. Therefore, E-jet printing occurs within a particular printing setup when E reaches a constant threshold that surpasses the capillary pressure.

The minimum electrostatic field intensity to initiate fluid flow, E_o, can be found using the following equation (Eyring, C. F., *et al.*, 1928**,** Marginean, I., *et al.*, 2006).

$$E_o = \frac{4V_o}{d_N \ln\left(\frac{8\mathrm{H}}{\mathrm{d_N}}\right)}. \qquad (7)$$

In equation (7), which is a slight modification of equation (3), H represents the standoff height between the nozzle and substrate, and V_o defines the minimum voltage difference necessary to initiate printing. Note that equation (7) could be used to calculate the electrostatic intensity for any applied voltage as a function of standoff height and nozzle diameter. As the standoff height H increases, V_o has to increase accordingly in order to maintain the same level of E_o that initiates printing. Importantly, to maintain consistent printing on a contoured surface using a traditional E-jet set-up, either the nozzle position has to change to maintain a constant standoff height with respect to the contoured profile (demonstrated by Seong, B., *et al.,* 2014), or the voltage needs to be adjusted so that the same value of E_o can be maintained throughout the printing process (demonstrated by Barton, K., *et al*. 2011 and Altin, B., *et al.* 2014).

(i) Substrate sensitivity test

To validate the airflow assisted E-jet printhead ability to mitigate substrate effects, we conducted a set of experiments. The experiments identified the minimum voltage V_o required to release material at varying standoff heights H : 30µm, 60µm, 100µm, 200µm, 300µm, 400µm, 500µm, 600µm, 700m, 800µm, 900µm, 1000µm, 1100µm and 1200µm. From equation (7), holding all other parameters constant, increasing the standoff height should result in an increase in applied voltage to meet the minimum electrostatic field intensity for droplet ejection.

These experiments were conducted for three different cases, with each case repeated 3 times:

1. E-jet printing (traditional): positively charged conductive printing nozzle with $d_N = 2\mu$m; conductive grounded substrate (gold sputtered glass slides).
2. E-jet printing: positively charged conductive printing nozzles with $d_N = 2\mu$m ; non-conductive substrate (glass slides).
3. Airflow assisted E-jet with 2 nozzles printing: positively charged conductive printing nozzle with $d_N = 2\mu$m ; non-conductive substrate (glass slides); grounded extractor nozzle with $d_E = 30\mu$m ; h = 20µm; $\alpha = 60^o$ from vertical, and experimentally determined P_E .

Figure 25 (a) shows the minimum voltage values (averaged across the three repeated tests) required for each standoff height for the different cases. Notice the curves for case 1 and 2 are almost

entirely overlapping. On the other hand, one can clearly see that the initiating voltages for the third case (airflow assisted printhead) are significantly lower across all standoff heights.

Additionally, as the standoff height increases, the relative change in the initiating voltage is much smaller as compared to the voltage changes in cases 1 and 2. These differences indicate that as the airflow assisted printhead moves further away from the substrate, the extractor nozzle plays an increasingly dominating role in the electrohydrodynamics as compared to the substrate, and therefore the disruptive effects from the substrate have been mitigated.

Using the parameters for the selected cases, the minimum electrostatic field intensity to initiate fluid flow E_o can be found using equation (7). For cases 1 and 2, basic electrohydrodynamics indicates that this initiating electrostatic field should remain relatively constant. From equation (7), the electrostatic field must be strong enough to overcome the capillary forces $\left({}^{4\gamma}/_{d_N}\right)$; a constant parameter (not a function of standoff height) that must be overcome to initiate fluid flow. Figure 25 (b) gives a relatively close demonstration of this theory.

Alternatively, case 3 requires the calculation of two electrostatic field vectors. In Figure 25 (b), E_o represents the conventional calculation using H, the standoff height between the printing nozzle and the substrate, while E_o^h calculates the electrostatic field using h, the standoff height between the printing and extractor nozzles. Figure 25 (b) presents the averaged electrostatic field values for the two standoff height calculations. While the absolute values of the minimum

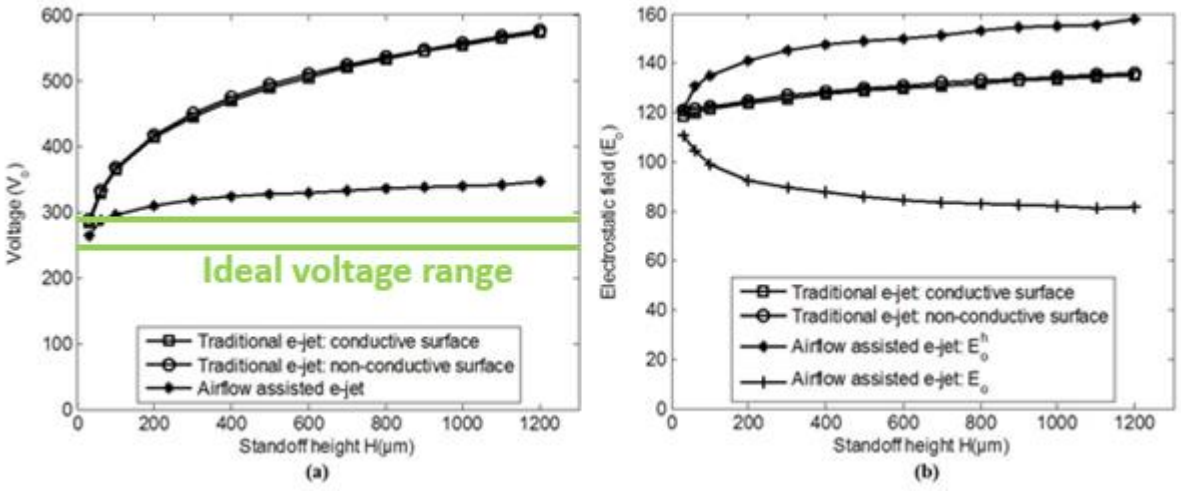

Figure 25. Process parameters for varying standoff heights in 2 nozzle airflow assisted E-jet. (a) Minimum ink releasing voltage V_o. (b) Minimum electrostatic field E_o to release ink.

electrostatic field differ from the more standard E-jet set-ups due to variations in the printing conditions and printhead configurations, we focus this discussion on the significance of the variations found in the data trends.

Similar to the conventional set-ups in cases 1 and 2, the electrostatic field required to initiate fluid flow as a function of the extraction mechanism standoff height (E_o^h in case 3) follows a slowly changing trend after ~400µm. The slope of the curve is 0.457V/µm for the first 3 data points, indicating a disruptive impact from the substrate on the printing dynamics when in *close* proximity to the printing nozzle. The impact diminishes as the airflow assisted printhead moves further away from the substrate as illustrated in Figure 25 (b) (the slope of the curve is 0.027V/µm for the last 8 data points). The plot of E_o for case 3 shows a rapidly decreasing electrostatic field, a violation of a basic electrohydrodynamic principle if one disregards the supplemental field provided by the extractor nozzle. This trend further indicates the importance of the extractor nozzle and the diminishing impact of the substrate in the jetting dynamics. Notice, however, there is a total change of 81V across 1170µm of standoff height change, which is beyond the ±10V ideal voltage range indicated in Figure 25 (a).

(ii) Printing capability demonstration

To demonstrate the capabilities of the airflow assisted E-jet printhead, this section presents printed patterns for varying standoff heights between the printhead and the substrate.

Applying the design methodology outlined in section 4.2.2, an airflow assisted printhead was designed and fabricated for experimental testing. Specific parameter selections are given in Table 3. The printing tests utilized a pulsed voltage modulation for the applied voltage as described in

Table 3. Airflow assisted E-jet with 2 nozzles process parameter for experimental printing

Parameter	Experimental values
Ink	Norland Optical Adhesive 81
Substrate	Non-conductive glass slide
d_N	2µm
d_E	30µm
V_f	296V
$V_{Baseline}$	70% V_f = 207V
V_{Peak}	110% V_f = 326V
P_E	3psi
α	60º from vertical
h	20µm
H	400µm, 800µm, 1200µm

section 1.3.3. The baseline and peak voltages were determined from a reference voltage V_f identified during the calibration process. To standardize printing across multiple experiments and assembled printheads, the calibration process identified the minimum ink releasing voltages at the following standoff heights: 30µm, 60µm, 100µm, 200µm, 300µm, 400µm, 500µm, 600µm, 700µm, 800µm, 900µm, 1000µm, 1100µm and 1200µm. The recorded voltages were then averaged to give the reference voltage V_f for that particular printhead.

Figure 26(a)-(c) presents dot matrices printed with the airflow assisted E-jet printhead at 400µm, 800µm, and 1200µm, respectively. All droplet diameters are sub-15µm, demonstrating superior resolution as compared to previous E-jet (standard set-up configurations) printing demonstrations at these standoff heights. Despite some scattering present in all three figures, it is important to note that the baseline and peak voltage values remained constant across all three standoff heights. This demonstrates relatively stable printing across an 800µm variation in standoff height from the printing nozzle to the substrate. This variation in standoff height is 3 orders of magnitude larger than a flat substrate, the *normal* surface utilized in conventional E-jet printing. Additionally, the selection of a single set of voltage parameters for the entire printing experiment represents a unique departure from the modulation approach presented in literature to handle significant standoff

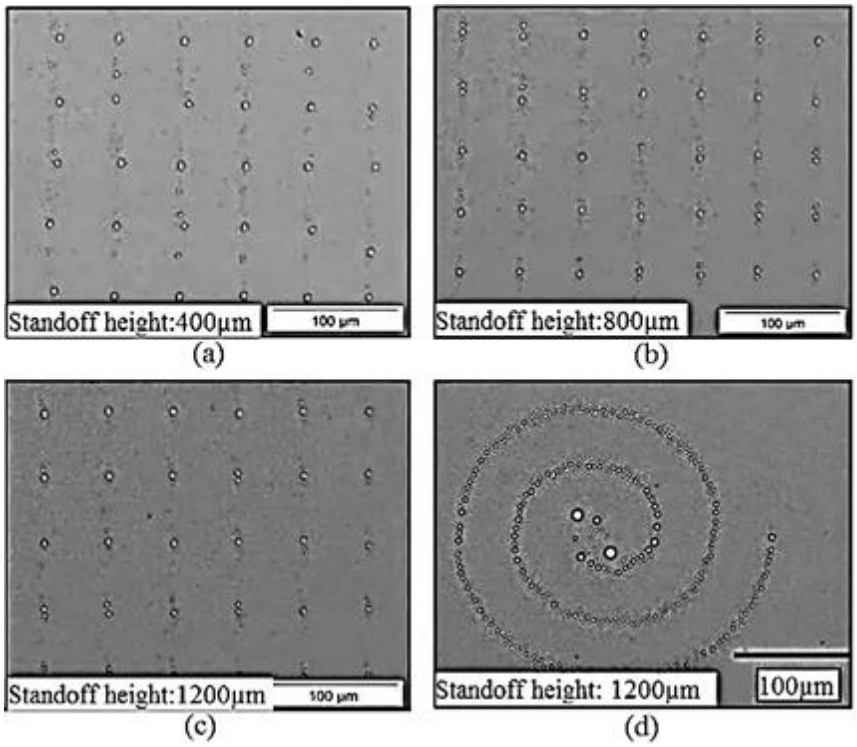

Figure 26. 2 nozzle airflow assisted E-jet printed patterns

height variations. Importantly, when the same voltage setting (Baseline voltage = 70%V_f , Peak voltage =110%V_f) are used in a conventional E-jet set-up, the process **cannot sustain printing** beyond the 400µm standoff height.

To further demonstrate the robustness of the airflow assisted E-jet printhead, Figure 26(d) shows a spiral pattern printed with a constant DC applied voltage of 326V at a standoff height of 1200µm. The spiral, with a ring-to-ring distance of 50µm, demonstrates the ability of the airflow assisted printhead to print a more complex, high-resolution (sub-10µm features) pattern with minimum distortion and scattering. The printing parameters used to print the patterns in Figure 26 are presented in Table 3.

4.2.4 Deficiencies of the airflow assisted E-jet printhead with 2 nozzles

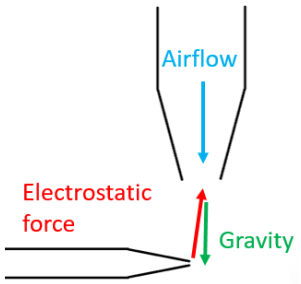

Figure 27. Misalignment of force directions in a 2 nozzle style printhead

The most prominent issue with the printhead is the presence of scattering, a common issue in E-jet printing that degrades the final quality of the printed device, and must be mitigated. Additionally, the airflow releasing mechanism should be revisited to address droplet displacement on the substrate due to airflow disturbances. The last issue of the printhead is the tight tolerance of the printing nozzle position. The ideal location of the printing nozzle tip, point A, as shown in Figure 24, is within a thin air mixing layer. It is very hard to place the nozzle accurately at point A; as such, it usually requires a lot of fine tuning to achieve optimum printing behavior. Alternatively, we can reach the same conclusion by looking at Figure 27, which illustrates the misalignment of the three forces that acts upon the ink droplets; the angle between the electrostatic force and the other two forces is almost 180°. Lastly, the variation within the minimum printing voltage across the various heights is beyond the ±10V ideal voltage range indicated in Figure 25 (a).

Importantly, these issues are created by the coupling effect between the design of the electrostatic field and the airflow dynamics. Because the extractor nozzle serves as the electrostatic and air jetting nozzle, these two extraction dynamics cannot be designed independently. The air jetting nozzle is restricted to being placed a short distance ($10d_N$) from the printing nozzle, along with

having a nozzle diameter ≥30μm to satisfy the electrohydrodynamic role of the nozzle. In this close proximity, the strong airflow from the extractor nozzle disrupts the electrohydrodynamics and leads to scattering. To address this issue, the airflow and electrohydrodynamics must be separated for independent design and control.

New knowledge: A gold sputtered nozzle acts as an ideal extractor mechanism for controlled generation of an electric field. Airflow can be used as an additional manipulation force. Airflow and electrohydrodynamic forces should be designed independently due to design and performance tradeoffs.

4.3 Hybrid E-jet Printhead: Airflow Assisted E-jet Printhead with 3 Nozzles

To separate the airflow and electrohydrodynamics, a three nozzle printhead with a printing nozzle, an electrically driven extractor feature, and an air jetting nozzle was designed. In the following section we will briefly explain the working principle of an airflow assisted E-jet printhead with 3 nozzles.

4.3.1 Basic Concept of Airflow Assisted E-jet Printhead with 3 Nozzles

The working principle of the airflow assisted E-jet printhead with 3 nozzles is very close to that of the printhead with 2 nozzles; a schematic diagram of the printhead is shown in Figure 28. The major difference is the decoupling of the air jetting nozzle from the extractor nozzle. The extractor nozzle is an empty nozzle with no air supply. By charging the printing nozzle positively and grounding the extractor nozzle, ink droplets are generated electrohydrodynamically. As the ink droplets travel through the air towards the extractor nozzle, the air jet from the vertical nozzle redirects the droplets down towards the substrate. Because of the addition of a new nozzle in this

Table 4. Airflow assisted E-jet with 3 nozzles process parameters

Parameter	Description
d_N	Printing nozzle diameter
d_E	Extractor nozzle diameter
d_A	Air jetting nozzle diameter
V	Applied voltage
P_A	Air pressure supplied to air jetting nozzle
α	Tilting angle of printing nozzle
β	Tilting angle of extractor nozzle
h	Standoff height between printing and air jetting nozzle tips
S	Distance between printing and extractor nozzle tips
H	Relative offset height between printing nozzle and substrate

design, it involves a few more parameters as compared to the 2 nozzle printhead. The parameters are given in Table 4.

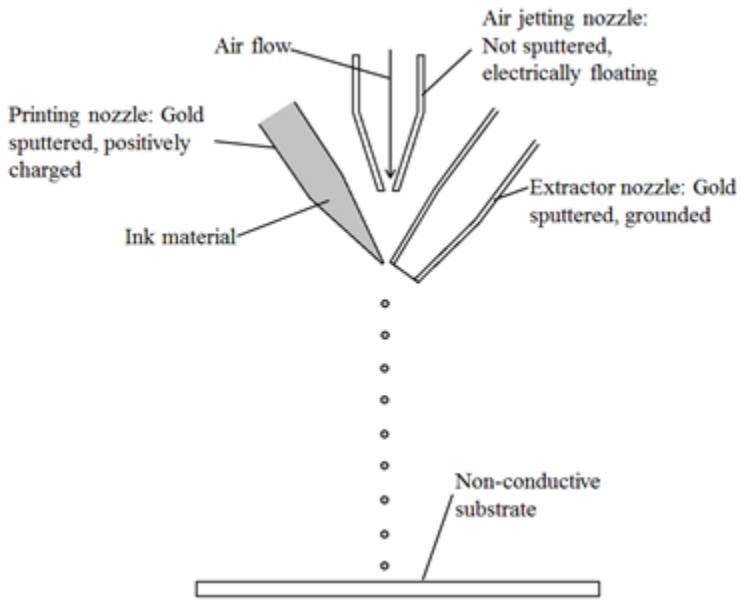

Figure 28. Schematic diagram of airflow assisted E-jet printhead with 3 nozzles

4.3.2 Printhead Design Methodology

This section provides a step-by-step design methodology for airflow assisted E-jet printhead design.

Step 1: Determine printer nozzle diameter d_N based on the desired feature resolution within the printed pattern. The diameter should lie within the range: 2• feature size < d_N < 10• feature size.

Step 2: Determine d_E by selected a nozzle diameter ≥30μm. From our experimental results, we found that the larger the extractor the more effectively it can control the electrohydrodynamics of the printing nozzle, and a d_E of 30μm is an experimentally determined lower limit of an effective extractor. The only drawback of using a large extractor is the bulk volume of the printhead, which can hinder the printhead from printing at low standoff height *H*.

Step 3: Determine d_A by selecting the smallest nozzle size that can redirect the ink droplets. As mentioned in section 4.2.2., the larger the nozzle size, the more turbulence that will be created. Therefore a smaller nozzle size for the air jetting nozzle leads to less scattering and displacement of ink material on the substrate.

Step 4: Determine the tilting angle α for the printing nozzle. The angle should be as vertical as possible, while avoiding physical contact between the printing nozzle and the vertical air jetting nozzle. As mentioned in section 4.2.2, the larger the angle α from vertical position, the more asymmetric the electrostatic field becomes, and the more scattering that will occur (see Figure 23(c) in section 4.2.2.). On the other hand, with the extractor nozzle no longer being the air jetting nozzle, the extractor nozzle tip can now be placed in front of the printing nozzle tip. To avoid physical contact between the printing nozzle and the vertical air jetting nozzle, angle α of the printing nozzle can be reduced down to 30º and the issue of an inhibited meniscus as shown in Figure 23(b) will never occur.

Step 5: Determine the tilting angle β for the extractor nozzle. The angle should again be as vertical as possible, while avoiding physical contact between the extractor nozzle and the vertical air jetting nozzle. While a printing nozzle with a large angle α scatters the ink droplets by **repelling** the ink droplets sideways, an extractor nozzle with a large angle β scatters the ink droplet by **attracting** the ink droplets sideways. Therefore the angle β should be as small as possible. We selected β to be 30º as well.

Step 6: Determine the distance between the printing nozzle and extractor nozzle tips *S*. This distance should be ~10 d_N, which is an experimentally determined optimum distance to ensure the extractor nozzle plays a dominate role in the electrohydrodynamics that govern the E-jet ejection process rather than the substrate. As mentioned in step 4, the tip of the extractor nozzle should be placed directly in front of the printing nozzle so that the meniscus can form properly at the printing nozzle tip.

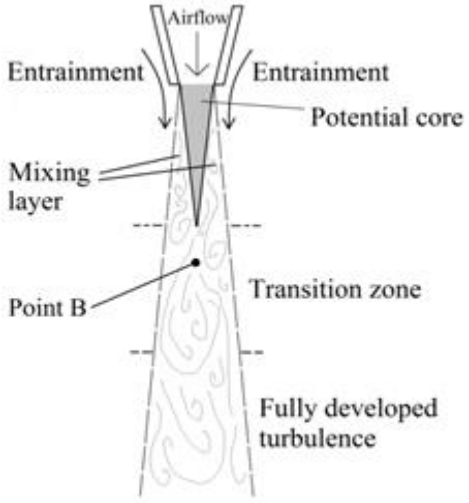

Figure 29. Schematic diagram of subsonic fluid flow from a nozzle (3 nozzle printhead)

Step 7: Determine the standoff height between the air jetting nozzle and the printing nozzle *h*. Since we do not want to disrupt the potential core, and the length of the potential core is ~4-6 d_A, the ideal standoff height *h* between the air jetting nozzle and the printing nozzle was experimentally determined to be ≥8d_A. This ideal location is indicated as point B in Figure 29.

Step 8: Determine P_E for optimal airflow dynamics. The optimum level of P_E is the smallest air pressure necessary to redirect the ink droplets away from the extractor nozzle and towards the substrate. High P_E values lead to droplet scattering and the displacement of printed material on the substrate. Start with a P_E value at the lowest pressure setting for the given system and increase until droplets are redirected onto the substrate.

4.3.3 Experimental Results

Once again, we will first demonstrate printhead ability to mitigate the substrate effect followed by a demonstration of the printing capability of the airflow assisted E-jet printhead with 3 nozzles.

(i) Substrate sensitivity test

To validate the airflow assisted E-jet printhead ability to resist substrate effects, we conducted a set of experiments very similar to the set we presented in section 4.2.3. The experiments identified the minimum voltage V_o required to release material at varying standoff heights H : 30µm, 60µm, 100µm, 200µm, 300µm, 400µm, 500µm, 600µm, 700m, 800µm, 900µm, 1000µm, 1100µm and 1200µm. From equation (7), holding all other parameters constant, increasing the standoff height should result in an increase in applied voltage to meet the minimum electrostatic field intensity for droplet ejection.

These experiments were conducted for three different cases, with each case repeated 3 times:

1. E-jet printing (traditional): positively charged conductive printing nozzle with $d_N = 2\mu\text{m}$; conductive and grounded substrate (gold sputtered glass slides).
2. E-jet printing: positively charged conductive printing nozzles with $d_N = 2\mu\text{m}$; non-conductive substrate (glass slides).
3. Airflow assisted E-jet printing with 3 nozzles: positively charged conductive printing nozzle with $d_N = 2\mu\text{m}$; non-conductive substrate (glass slides); grounded extractor nozzle with $d_E = 30\mu\text{m}$, air jetting nozzle with d_A = 10µm; S = 20µm, h = 100µm; α = 30º from vertical, β = 30º from vertical, and experimentally determined P_E.

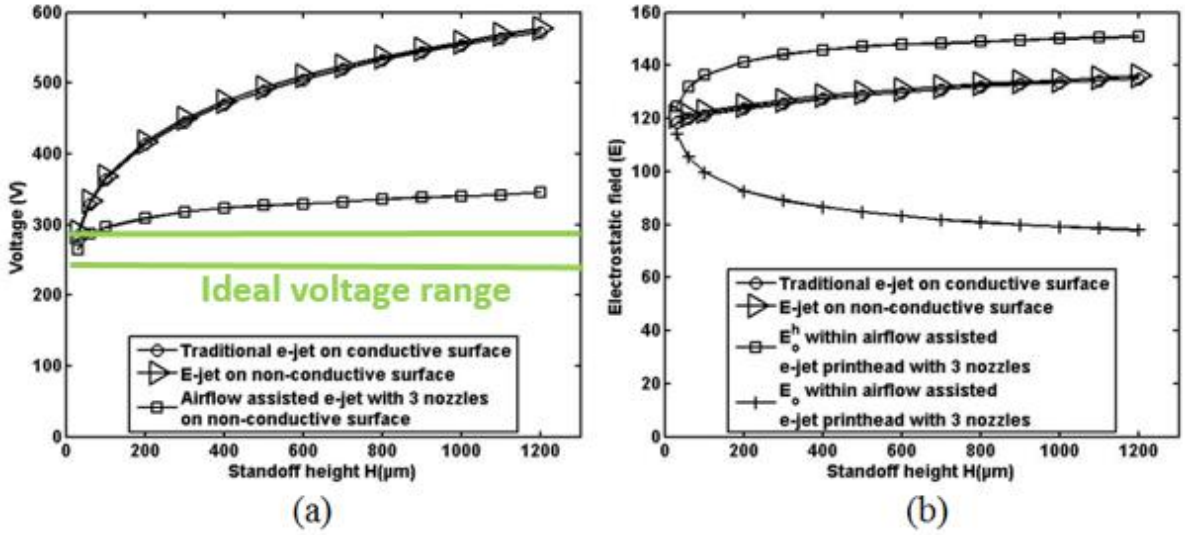

Figure 30. Process parameters for varying standoff heights using a 3 nozzle airflow assisted E-jet printhead. (a) Minimum ink releasing voltage V_o. (b) Minimum electrostatic field to release ink E_o.

As can be seen in Figure 30, the trends that we identified and described in Figure 25 are once again represented in Figure 30. Importantly, the effect of the substrate on the electrostatic field has been greatly reduced by the introduction of a third nozzle. As can be seen in Figure 30 (a), the applied voltage required to release material from the printing nozzle shows a small increase over 1200μm of standoff height variation; a stark contrast to the large increase in initiating voltage seen in the more conventional E-jet set-ups with either a conductive or non-conductive substrate. This difference is even more pronounced if we focus on the printing dynamics for standoff heights beyond 400μm. The slope of the curve in Figure 30 changes from 0.371V/μm for the first 3 data points to 0.011V/μm for the last 8 data points. Notice however, there is a total change of 58V across 1170μm of standoff height change, which is beyond the ±10V ideal voltage range indicated in Figure 30(a).

(ii) Printing capability demonstration

Dot matrices: To validate the printing capabilities of the airflow assisted E-jet printhead with 3 nozzles, we conducted several experimental tests. Of particular importance are the results from printing onto a tilted non-conductive surface with varying tilting angles. Figure 31 shows a schematic diagram of the experimental setup we created for printing onto tilted non-conductive surfaces. Initial printing began with a 400μm vertical standoff height between the substrate and the printing nozzle. The printing was performed as a rastered trajectory with the substrate moving

in the XY plane. As the substrate progressed in the X-axis direction, the tilted surface resulted in a large variation in the vertical distance between the printing nozzle tip and the substrate. We once again used the pulse printing technique mentioned in section 1.3.3 to print these dot matrices on the 3 tilted surfaces.

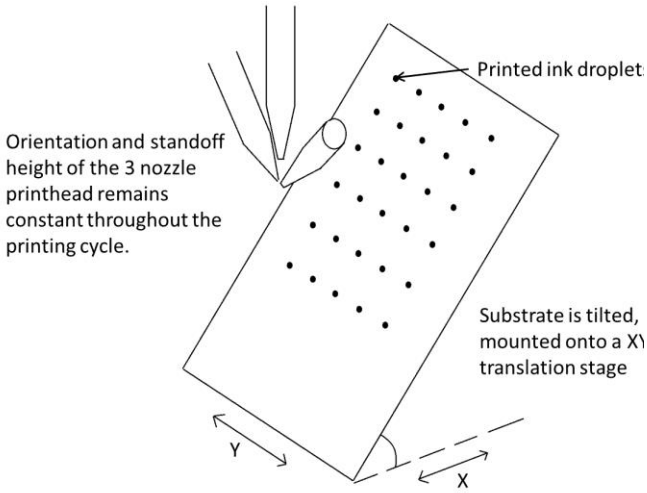

Figure 31. Schematic diagram of tilted surface printing

Similar to the procedure mentioned in section 4.2.3 (ii), the baseline and peak voltages were determined from a reference voltage V_f identified during the calibration process. To standardize printing across multiple experiments and assembled printheads, the calibration process identified the minimum ink releasing voltages at the following standoff heights: 30µm, 60µm, 100µm, 200µm, 300µm, 400µm, 500µm, 600µm, 700µm, 800µm, 900µm, 1000µm, 1100µm and 1200µm. The recorded voltages were then averaged to give the reference voltage V_f for that particular printhead or nozzle. Table 5 shows the printing parameters we used for printing the three dot matrices provided in Figure 32. It is important to note that the printhead and process parameters remained constant for the dot matrix printings across all three tilted surfaces (e.g. applied voltage did not vary, standoff height was constant).

Table 5. Printing parameters for 3nozzles airflow assisted E-jet printed dot matrices on titled surface

Parameter	Value
d_N	2µm
d_E	30µm
d_A	10µm
V_f	315V
$V_{Baseline}$	80% V_f ≈ 262V
V_{Peak}	130% V_f ≈ 415V
Pulse width	100ms
P_A	10psi
α	30°
β	30°
h	100µm
S	20µm
Ink material	NOA 81
Substrate	Tilted 150µm thick glass slip

Due to the different tilting angles in each case, the changes in vertical standoff height across adjacent rows in the three substrates are not the same and they are labelled in Figure 32. If we compare the printed result of the airflow assisted E-jet printhead with 3 nozzles in Figure 32 with the results we have for traditional E-jet printing on a tilted surface provided in Figure 33, we can clearly see the significant level of improvement in the printing quality with the airflow assisted E-jet printhead. The printed patterns using traditional E-jet printing on a tilted surface are inconsistent and show significant scattering effects (Figure 33(a)). Additionally, the angle of tilt greatly affects the ability of the traditional E-jet printer to release material; the release of materials was not observed after the 5th row on a surface tilted at 45 degrees (Figure 33(b)) or after the 4th row for a 65 degree tilted surface as shown in Figure 33 (c).

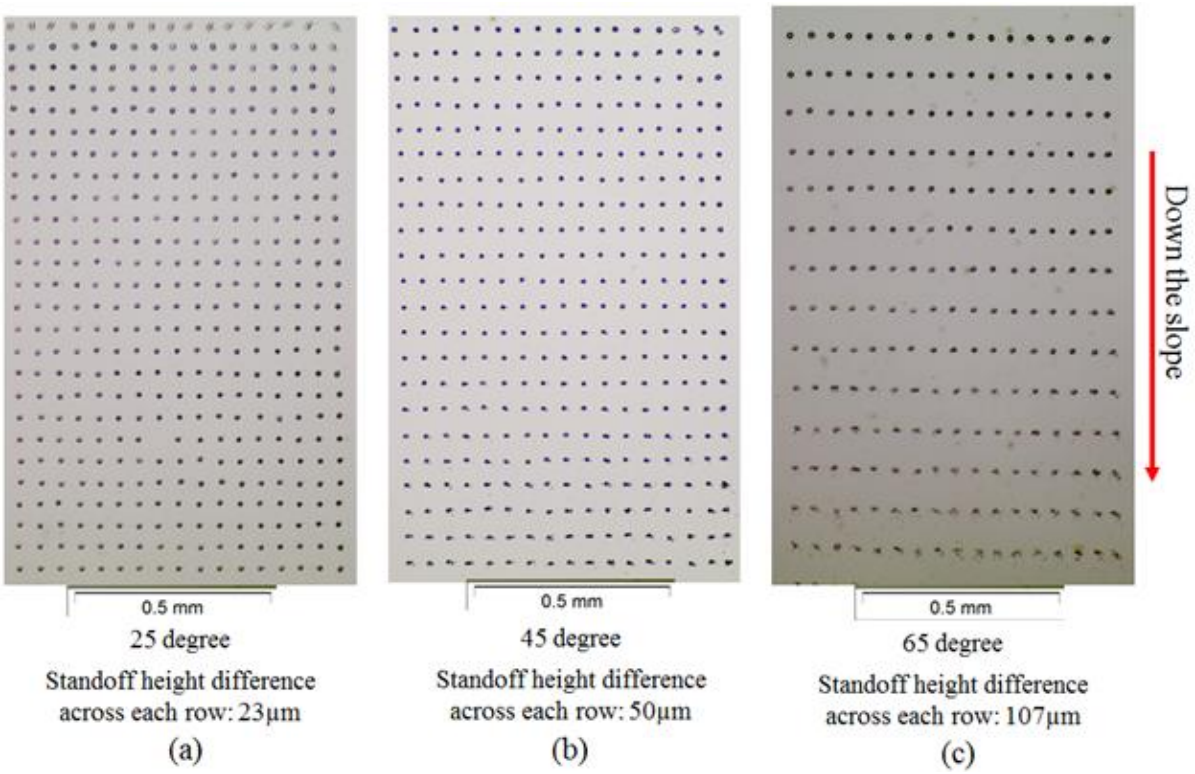

Figure 32. Printed dot matrices by airflow assisted printhead with 3 nozzles on tilted glass slips

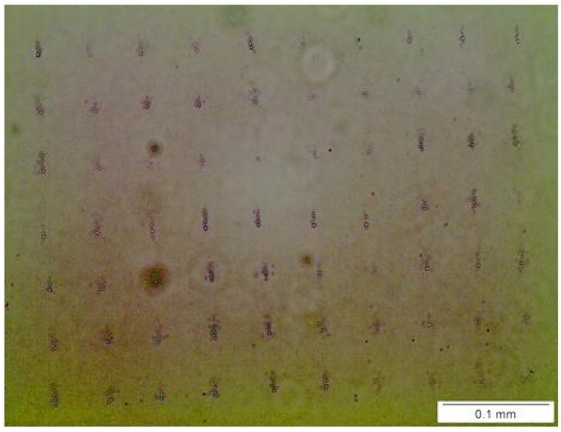

Parameter	Value
d_X	2µm
V_f	489V
$V_{Baseline}$	70% $V_f \approx$ 342V
V_{Peak}	130% $V_f \approx$ 635V
Pulse width	100ms
Ink material	NOA 81
Substrate	25° Tilted 150µm thick glass slip

(a)

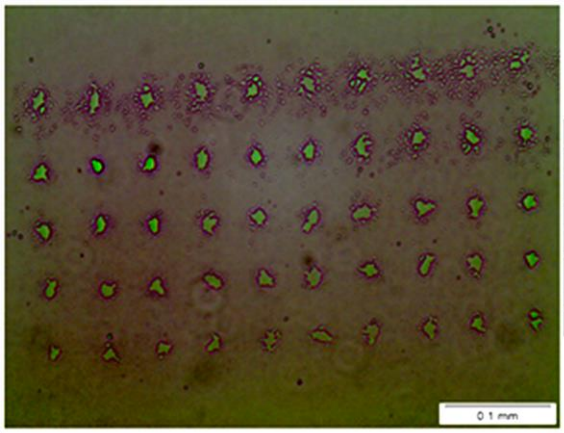

Parameter	Value
d_X	2µm
V_f	472V
$V_{Baseline}$	70% $V_f \approx$ 330V
V_{Peak}	130% $V_f \approx$ 614V
Pulse width	100ms
Ink material	NOA 81
Substrate	45° Tilted 150µm thick glass slip

(b)

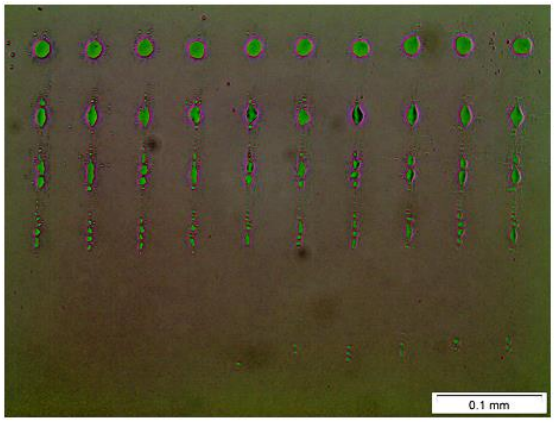

Parameter	Value
d_X	2µm
V_f	470V
$V_{Baseline}$	70% $V_f \approx$ 329V
V_{Peak}	130% $V_f \approx$ 611V
Pulse width	100ms
Ink material	NOA 81
Substrate	65° Tilted 150µm thick glass slip

(c)

Figure 33. Printed dot matrices by traditional E-jet nozzle on tilted glass slips.

Droplet directionality: In addition to poor printing quality, traditional E-jet does not place ink droplets vertically onto a tilted surface due to the asymmetric electrostatic field. Figure 34 shows a schematic diagram of the asymmetric electrostatic field of an e–jet nozzle on a tilted surface; the ink droplet trajectory is tilted which gives rise to undesirable and unpredictable ink droplet quality.

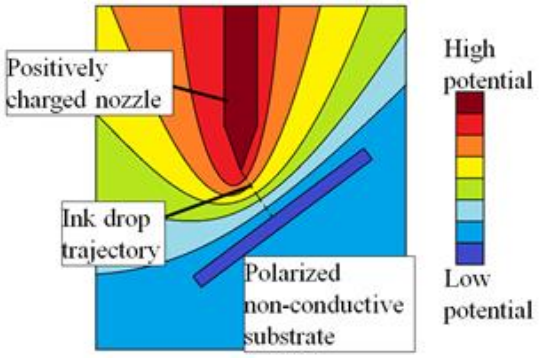

Figure 34. Schematic diagram of electrostatic field of a traditional E-jet nozzle on tilted substrate

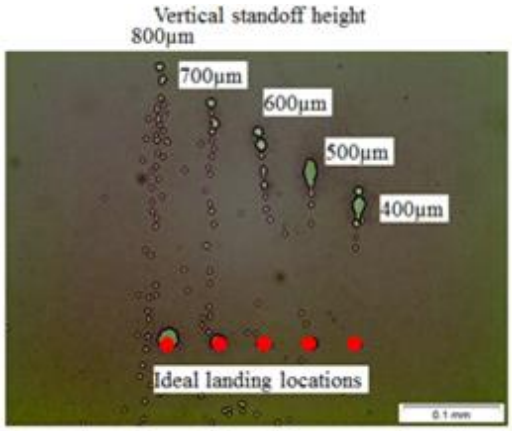

Vertical standoff height	Ink releasing voltage
400	633
500	662
600	679
700	695
800	701

Figure 35. Change in ink droplet landing position of traditional E-jet printing onto a 65º tilted surface

To validate this phenomenon, we conducted an experimental test that investigated the effect of droplet trajectory misdirection. Figure 35 shows the change in ink droplet landing location for traditional E-jet printing on a 65º tilted glass slip. The red dots in Figure 35 indicate the vertical locations that lie directly under the nozzle tip (e.g. the desired droplet placements). While printing at different vertical standoff heights, instead of landing on the ideal location vertically below the nozzle, the ink droplets land at a higher position as predicted by the tilted ink droplet model provided in Figure 34. We can also see that as the vertical standoff height increases, the scattering effect gets worse as well.

Spiral patterning: Figure 37 shows three spiral patterns printed on 25 degree, 45 degree, and 65 degree tilted surfaces. Figure 36 depicts a representative diagram of the E-jet set-up for the spiral printing. The printing conditions of these patterns are the same as those provided in Table 5 with the exception of a constant 415v DC printing modality rather than the pulse printing mode used to create the dot matrices. The substrate followed a spiral pattern within the horizontal plane, while the printhead was held constant. Neither vertical z-axis adjustments nor modified applied voltage was used to compensate for the varying external standoff height over the course of the spiral pattern. Note that the patterns have different lengths because they were printed on substrates at varying tilted angles, in which the angle of tilt

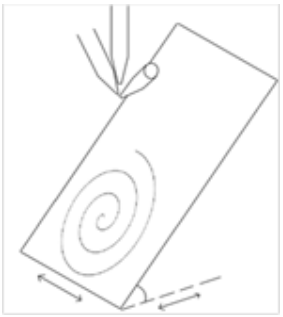

Figure 36. Schematic diagram of spiral printing

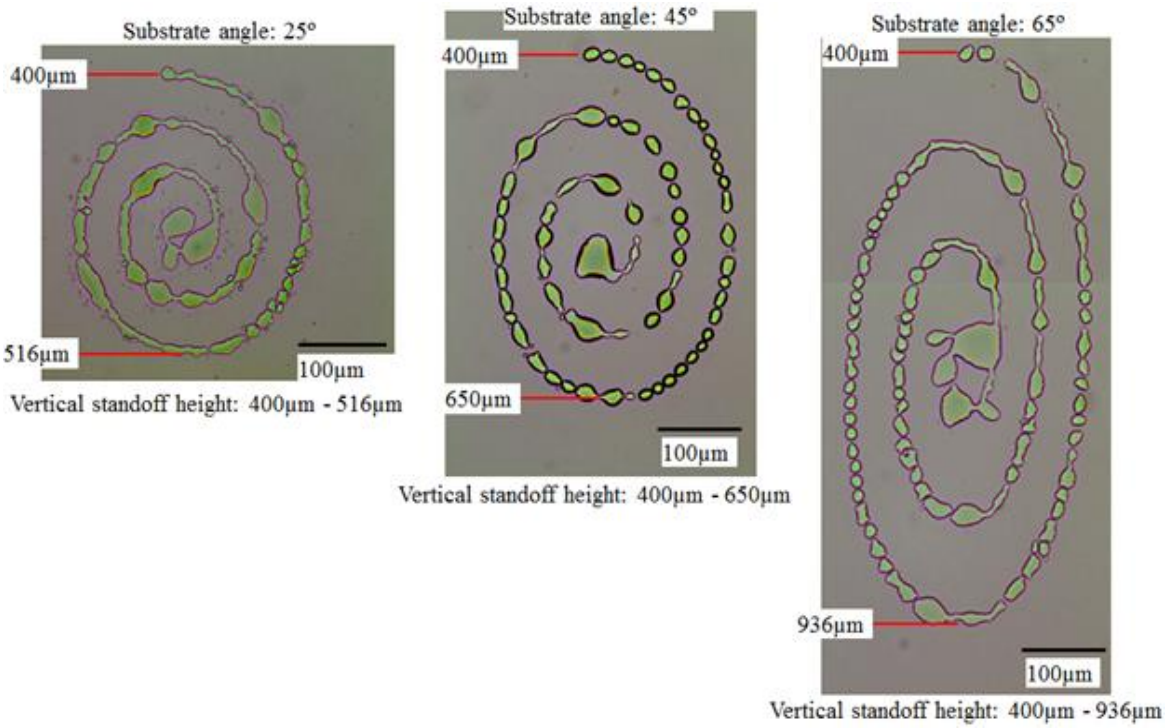

Figure 37. Spiral patterns printed by airflow assisted E-jet printhead on three tilted surfaces.

The tilting angle determines the vertical stretch (e.g. larger tilt angle leds to more stretch). Because the ink droplets landed vertically under the nozzle, the printed pattern reflects the vertical stretch.

Pulse width printing variations: The airflow assisted printhead with 3 nozzles was also tested with the pulse printing technique mentioned in section 1.3.3 to observe the behavior of different pulse widths during the printing process. In effect, we wanted to validate the ability of the 3 nozzle airflow printhead to respond to pulse width variations in a predictable manner as outlined in (Mishra, S., *et al.* 2010). The pulse width was varied from 100ms to 20ms (see Table 6 for printing parameters used in this experiment). As per the guidelines in (Mishra, S., *et al.* 2010), a decrease in pulse width should correspond to a decrease in droplet diameter (e.g. shorter time intervals results in less material being released within the given time).

As predicted, the decrease in pulse width resulted in a reduced droplet diameter (see

Table 6. Printing parameters of 3 nozzle style printhead using different pulse width

Parameter	Value
d_N	2µm
d_E	30µm
d_A	10µm
V_f	299V
$V_{Baseline}$	90% V_f ≈ 269V
V_{Peak}	140% V_f ≈ 419V
P_A	10psi
α	30º
β	30º
h	100µm
S	20µm
Ink material	NOA 81
Substrate	65º Tilted 150µm thick glass slip

Figure 38). The printed droplet diameter reduced from an average size of 17µm (Figure 38(a)) to an average size of 10µm (Figure 38(b)) when the pulse width was reduced from 100ms to 20ms. Note the consistency in the printed droplets over a 214µm variation in standoff height.

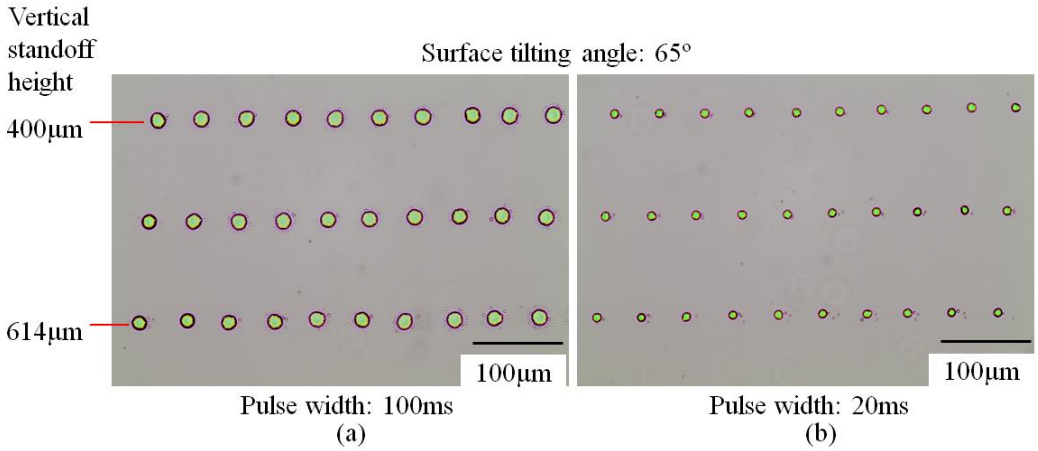

Figure 38. Airflow assisted E-jet printhead with 3 nozzles printing using 2 different pulse widths

4.3.4 Deficiencies of Airflow Assisted E-jet Printhead with 3 Nozzles

The airflow assisted E-jet printhead with 3 nozzles has greatly reduced the scattering effect as compared to the printhead with only 2 nozzles; it is also much easier to tune without the coupling effect between the airflow and electrostatic field as observed in the 2 nozzle design. Despite these improvements, the 3 nozzle printhead design requires a considerable amount of setup time, calibration, and parameter tuning. The electrostatic force in the printhead is also misaligned with the gravity force and the airflow direction; the misalignment is less than the 2 nozzle style integrated printhead (misalignment ~180°), but there is still an ~90° misalignment as shown in Figure 39. Additionally, the current design still fails the substrate sensitivity test; there is a total change of 58V across 1170µm of standoff height change, which is beyond the ±10V ideal voltage range indicated in Figure 30 (a).

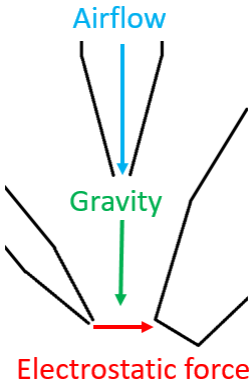

Figure 39. Misalignment of force directions in a 3 nozzle style printhead

An additional limitation of the 3 nozzle approach comes from the restriction on the allowable applied voltage. Recall from equations (1) and (3) in section 1.3.3 that droplet size and applied voltage are inversely related; a high applied voltage signal will lead to the release of smaller ink droplets. Thus, to drive down the resolution capabilities, we must apply relatively high voltages.

For the 3 nozzle design, a high voltage increases the attraction force between the released ink droplets and the extractor nozzle, requiring a stronger airflow to redirect the ink droplets onto the substrate. This strong airflow will lead to scattering or even displacement of ink materials on the printing substrate and render the printhead non-functional. Hence, the tradeoff between airflow strength and printing voltage restricts the printing resolution of the airflow assisted E-jet printhead.

Finally, the current printhead design cannot be readily converted into a mass production design, nor is it suitable for scale up to a multi-nozzle array. As throughput is a major limitation in E-jet printing, a successful design should lead towards a multi-nozzle array.

With a goal towards a higher level of flexibility, reliability, and throughput all encapsulated within a *plug-and-play* printhead, more self-contained designs must be investigated. **Important to this research is the new knowledge we have been building in high-resolution E-jet printing towards the understanding, characterization, and control of key process and design parameters.**

New knowledge: To reduce the misalignment of the force directions, a radially symmetric printhead structure is preferred. To further reduce substrate sensitivity of the printhead, it is necessary to shield the printing nozzle from the external environment to mitigate the polarization effects of the substrate when in close proximity to the printing nozzle.

Chapter 5

Advancements in Airflow Assisted Integrated E-jet Printing

While the three nozzle integrated printhead showcased in Chapter 4 provided new insights into the actuation dynamics that govern E-jet printing, sensitivity to substrate interactions, particularly at near-field offset heights (< 100 microns), was not completely mitigated. As such, there was a need for continued design and analysis to fully understand the interactions between the substrate and the integrated nozzle, such that a modified design that eliminates substrate effects could be identified. Building from our knowledge obtained from previous design iterations, this chapter introduces a modified nozzle-in-nozzle design with extensive process characterization to understand the advantages and limitations within an integrated two-nozzle design. Manufacturability and ease of use will also be discussed.

5.1 Airflow Assisted Nozzle-in-Nozzle E-jet Printhead

An Airflow assisted Nozzle-in-Nozzle (or simply Nozzle-in-Nozzle) design is a variation of the 2 nozzle style printhead showcased in Section 4.2. However, unlike the 2-nozzle style shown in Section 4.2, the Nozzle-in-Nozzle design utilizes radial symmetry to guide the applied voltage and airflow for enhanced E-jetting performance. In addition to the improved printing performance, this radial design enables a faster and more straight-forward assembly process, an important consideration for commercial viability.

5.1.1 Basic Concept of Nozzle-in-Nozzle E-jet Printhead

The outlook and the conceptual illustration of a Nozzle-in-Nozzle E-jet printhead is provided in Figures 40 and 41. The two key components within the design include a conductive nozzle that contains the ink material (printing nozzle) and a conductive nozzle that enables airflow through the orifice (extractor nozzle). In the set-up provided in Figure 41, the extractor nozzle serves as

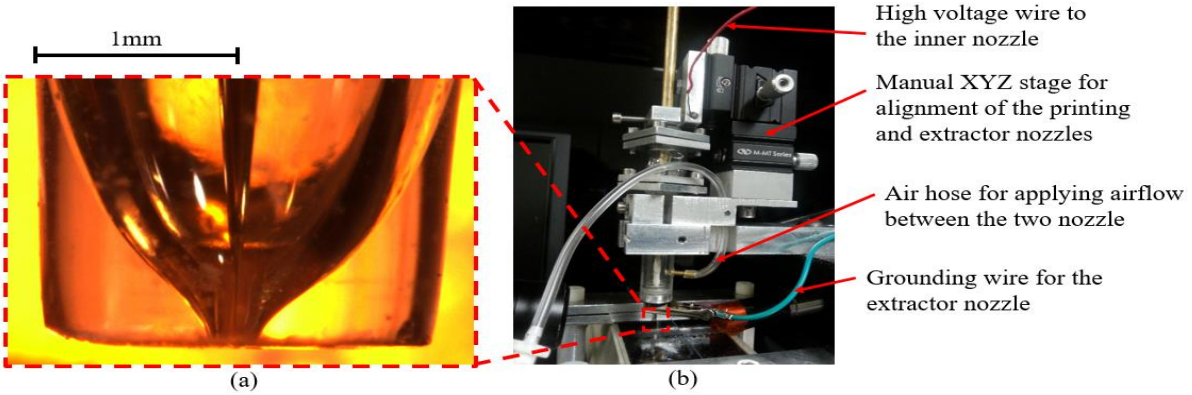

Figure 40. Image of a Nozzle-in-Nozzle E-jet printhead

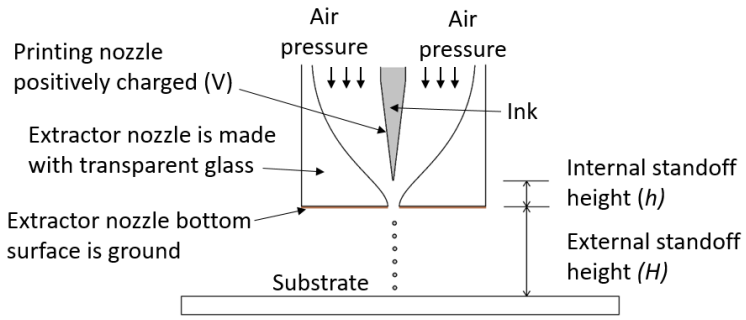

Figure 41. Schematic diagram of Nozzle-in-Nozzle E-jet printhead

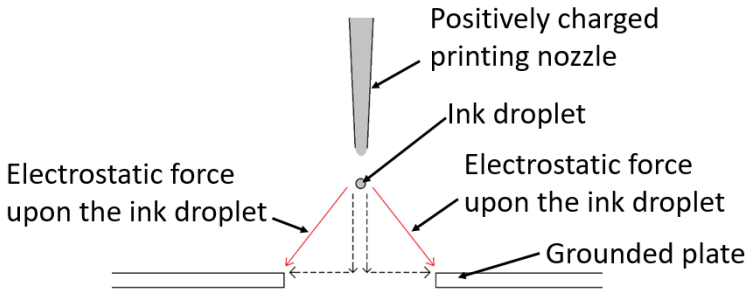

Figure 42. Schematic diagram of electrostatic forces in a nozzle-extractor ring E-jet printhead. Red arrows represent electrostatic forces, the dotted black arrows represent vertical and horizontal components of the electrostatic forces.

the actuation mechanism. Meniscus generation and ejection are driven by an electric field generated through the interaction between the grounded bottom surface of the extractor nozzle and the positive voltage applied to the printing nozzle. As the droplet releases from the meniscus, the electric field draws the material towards the edge of the extractor nozzle orifice, which is grounded. At this point, airflow from the extractor nozzle redirects the droplet trajectory from the grounded orifice towards the substrate. With this Nozzle-in-Nozzle design, the electrostatic field and air pressure are radially symmetric in the printing process. The extractor nozzle serves three purposes: (1) provides electrostatic force to pull the meniscus into a Taylor cone, (2) utilizes airflow to cancel

the horizontal component of the electrostatic force to redirect the ejected droplets smoothly out of the orifice with a streamlined inner profile (see Figure 41), and (3) shields the printing nozzle from external electrostatic fields generated by the substrate or other external surfaces.

In all the "nozzle – extractor ring" E-jet designs, the released ink droplets experiences electrostatic forces that draw the droplets to the extractor ring as shown in Figure 42. These electrostatic forces represented by the red arrows in Figure 42, can be separated into vertical and horizontal components, which are represented by the dotted black arrows. Purpose (2) of the extractor nozzle is to cancel the horizontal components of the electrostatic force with the guided airflow. It is worth noting the importance of the streamlines inner profile within the extractor nozzle; without such an inner profile, turbulence would be generated around the orifice resulting in excessive scattering of the ink droplets.

This design also aims to align the resultant forces within the printhead. The schematic in Figure 43 illustrates that the misalignment of the 3 actuation forces is less than 5°, which indicates the closest alignment among all of the integrated E-jet printhead designs.

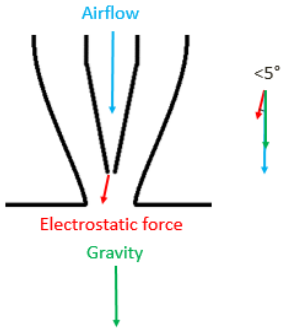

Figure 43. Schematic diagram of force directions in a nozzle-in-nozzle printhead.

Key process parameters that dictate the printing behavior of an airflow assisted Nozzle-in-Nozzle E-jet printhead are given in Table 7. The design process for these parameters requires a systematic approach in which the individual design decisions are a function of application, functional requirements, and basic physics of the air assisted E-jet process.

Table 7. Airflow assisted Nozzle-in-Nozzle E-jet process parameters

Parameter	Description
d_N	Printing nozzle outer diameter
d_E	Extractor nozzle orifice diameter
V	Applied voltage
P_E	Air pressure supplied to extractor nozzle
h	Standoff height between printing nozzle tip and extractor nozzle orifice
H	Relative offset height between the extractor nozzle and the substrate

5.1.2 Printhead Design Methodology

This section provides a step-by-step design methodology for the Nozzle-in-Nozzle E-jet printhead.

Step 1: Determine printer nozzle diameter d_N based on the desired resolution of the individual features within the printed pattern. Since the ink wets the outer surface of a jetting nozzle, the effective meniscus diameter corresponds to the outer diameter of the nozzle. At this stage we have only tested the printhead with NOA (Norland Optical Adhesive) 81 at the lowest printing voltage regime, which is the dripping mode (Jaworek, A. et al., 1999, Onses, M. S. et al, 2015). According to our previous printing experiences, using NOA 81 printing with dripping mode, a nozzle with a diameter of d_N can effectively print features sizes of $\{1-10\} \times d_N$. For other ink materials, such as distilled water, a very similar relationship was observed (Jaworek, A. et al., 1999).

Step 2: Determine d_E as a tradeoff between electrostatic behavior and fluid dynamics of the airflow. A large extractor nozzle orifice results in several key printing challenges: (1) it creates a large distance between the grounded orifice and the nozzle tip, which drives the printing voltage up unnecessarily, (2) a large d_E also generates excessive airflow, leading to undesirable scattering behavior, and (3) a large d_E reduces the effectiveness of the extractor nozzle to act as a shield between the inner printing nozzle and external electrostatic field disturbances. Conversely, as the size of d_E decreases, the ejected ink droplets will experience increased electrostatic attraction towards the inner edge of the extractor nozzle orifice, resulting in misalignment of the ejected droplets and potential failure of the droplets to pass through the orifice. To redirect the droplets away from the inner edge of the grounded orifice, a higher air pressure will be required, resulting in increased scattering due to the higher air flow passing through the orifice. Therefore, the selection of d_E should balance the tradeoff between scattering due to a large horizontal electrostatic force components, shielding of the inner conductive nozzle, and droplet scattering due to increased airflow. For high-resolution printing (<15μm features), a good starting point is d_E =100μm.

Step 3: Determine the standoff height h between the two nozzles. This distance dictates the vertical and horizontal components of the electrostatic force experienced by the ink droplets. If h is too short ($h < d_E$), the horizontal components of the electrostatic force upon the droplet (see Figure 42) will be strong enough to scatter the droplet (for supporting data, see section 5.2.2 (ii)). As mentioned in step 2, larger horizontal components of the electrostatic force require increased air pressure to redirect the droplets away from the grounded nozzle orifice, which can lead to scattering of the droplets on the substrate surface. Moreover, if the misdirection of the ejected droplets is not corrected by airflow, the strong horizontal electrostatic force component that drives

the droplets towards the extractor orifice will create scattering behavior directly. On the other hand, we have observed that ink droplets do not exit the extractor nozzle when $h \geq 2.5 \cdot d_{E,}$. To maintain stable and high quality printing, a good rule of thumb for h will be $d_E < h < 2.5 \times d_E$.

Step 4: Determine the air pressure P_E for optimal airflow dynamics. The optimum level of P_E is the smallest air pressure necessary to redirect the ink droplets away from the extractor nozzle and towards the substrate. High P_E values lead to droplet scattering and the displacement of printed material on the substrate. Start with a P_E value at the lowest pressure setting for the given system and increase until droplets are redirected onto the substrate.

5.2 Nozzle-in-Nozzle E-jet Printhead Experimental Results

We have conducted two sets of experiments with our Nozzle-in-Nozzle printhead prototype. The first set of experiment is a substrate sensitivity test for validating the printhead's ability to mitigate substrate effects. The second set of experiments is a printing performance study, which investigates the relationships between the printing parameters listed in Table 7 and the different performance metrics.

5.2.1 Investigating the Effects of Substrate Sensitivity

The objective of this set of experimental tests was to investigate the effects of substrate sensitivity as a function of the new integrated Nozzle-in-Nozzle design. To evaluate the impact of the substrate to the applied electrostatic field, these experiments focused on identifying the minimum applied voltage V_o required to release material at varying standoff heights between the substrate and the extractor nozzle (external standoff height H). In these experiments, the external standoff height (H) was varied as: 200µm, 400µm, 600µm, 1000µm, 1500µm. From equation (7), holding all other parameters constant and utilizing a more conventional E-jet setup that relies on the substrate to generate a potential field, increasing the standoff height should result in an increase in applied voltage to meet the minimum electrostatic field intensity for droplet ejection.

These experiments were conducted for 7 different cases:

1. E-jet printing: positively charged conductive printing nozzles with d_N = 8µm; non-conductive substrate (glass slides).

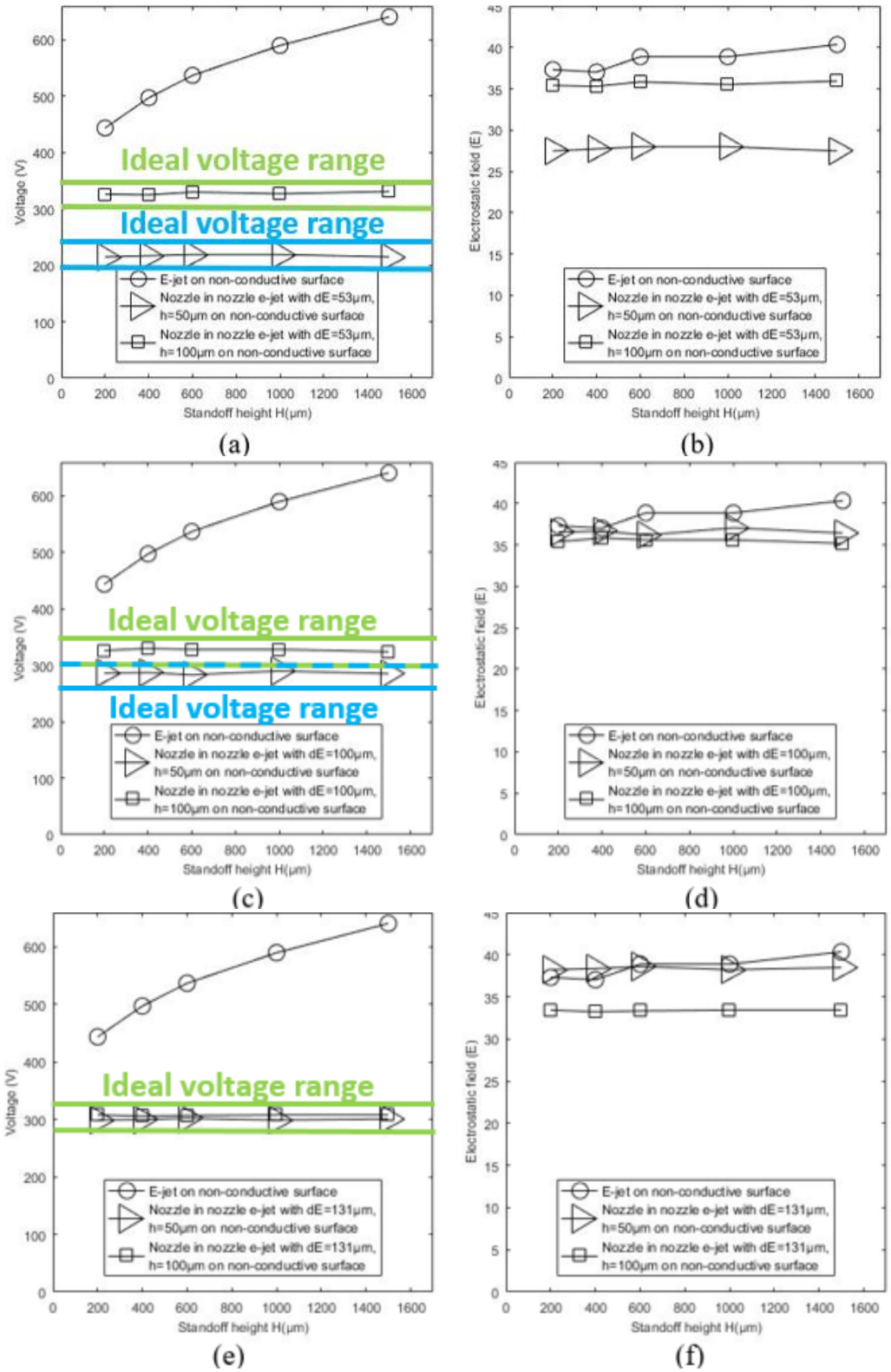

Figure 44. Process parameters for varying standoff height and extractor nozzle size (a), (c), (e) Minimum ink releasing voltage V_o, (b), (d), (f) Minimum electrostatic field E to release ink

2. Airflow assisted Nozzle-in-Nozzle E-jet: positively charged conductive printing nozzle with d_N = 8μm; non-conductive substrate (glass slides); grounded extractor nozzle with d_E = 53μm; h = 50μm, and experimentally determined P_E (0.625psi, or 4309Pa).
3. Airflow assisted Nozzle-in-Nozzle E-jet: positively charged conductive printing nozzle with d_N = 8μm; non-conductive substrate (glass slides); grounded extractor nozzle with d_E = 53μm; h = 100μm, and experimentally determined P_E (0.5psi, or 3447Pa).
4. Airflow assisted Nozzle-in-Nozzle E-jet: positively charged conductive printing nozzle with d_N = 8μm; non-conductive substrate (glass slides); grounded extractor nozzle with d_E = 100μm; h = 50μm, and experimentally determined P_E (0.0438psi, or 302Pa).
5. Airflow assisted Nozzle-in-Nozzle E-jet: positively charged conductive printing nozzle with d_N = 8μm; non-conductive substrate (glass slides); grounded extractor nozzle with d_E = 100μm; h = 100μm, and experimentally determined P_E (0.0438psi, or 302Pa).
6. Airflow assisted Nozzle-in-Nozzle E-jet: positively charged conductive printing nozzle with d_N = 8μm; non-conductive substrate (glass slides); grounded extractor nozzle with d_E = 131μm; h = 50μm, and experimentally determined P_E (0.0625psi, or 431Pa).
7. Airflow assisted Nozzle-in-Nozzle E-jet: positively charged conductive printing nozzle with d_N = 8μm; non-conductive substrate (glass slides); grounded extractor nozzle with d_E = 131μm; h = 100μm, and experimentally determined P_E (0.0625psi, or 431Pa).

Figure 44 (a), (c) and (e) show that the airflow assisted Nozzle-in-Nozzle printhead has superior resistance against substrate influence compared to the 3 nozzle style printhead. As shown in Figure 30 from section 4.3.3, the minimum printing voltage of a 3 nozzle style printhead increases on the order of 10V per 200μm for standoff heights of 600μm or below, whereas the Nozzle-in-Nozzle printhead varies less than 10V across all of the tested conditions (all printing conditions pass the

Table 8. Minimum printing voltage at different standoff heights on a regular glass surface

Standoff height	**Standard E-jet**	**3 nozzle printhead**	**Nozzle-in-Nozzle printhead**					
			d_E = 53μm h =50μm	**d_E = 53μm h =100μm**	**d_E = 100μm h =50μm**	**d_E = 100μm h =100μm**	**d_E = 131μm h =50μm**	**d_E = 131μm h =100μm**
200μm	417V	309V	215V	326V	286V	326V	299V	308V
400μm	474V	319V	217V	325V	287V	330V	300V	306V
600μm	510V	324V	219V	330V	283V	328V	302V	307V
1000μm	557V	328V	219V	327V	290V	328V	299V	308V
Voltage span	**140V**	**19V**	**4V**	**5V**	**7V**	**4V**	**3V**	**2V**

substrate sensitivity test). This is summarized in Table 8, which compares the minimum printing voltage for different E-jet printing techniques on a regular glass surface at different standoff heights. Note that for the different sets of extractor nozzle diameter d_E and internal standoff height h, the minimum printing voltage of a Nozzle-in-Nozzle printhead varied within 7 volts or less as the standoff height changed by 800µm. By comparison, the voltage change required to ensure printing across the 800µm for the standard E-jet setup was found to be 140V. It is important to note that the minimum printing voltage for a 3 nozzles style printhead (as seen from Figure 30 from section 4.3.3) changed by 19V as the standoff height increased by 800µm. Figure 44 (b), (d) and (f) demonstrate the consistency in the initiating electric potential E_o across the varying external standoff heights. This correlates with our expectation of the initiating electric field, despite the less than 10V variation in applied voltage across the height variations. These results illustrate that the modified nozzle in a nozzle style printhead can effectively shield the external electrostatic field from the electrohydrodynamics within the printhead, and that the electrohydrodynamics are driven by the integrated nozzles.

5.2.2 Printing Performance Study

To investigate the relationship between the controlling parameters of a Nozzle-in-Nozzle printhead and printing performance, we have conducted a series of printing experiments using different extractor nozzle diameters d_E and internal standoff heights h at varying substrate standoff heights H. A total of 30 dot matrices were printed using a rastered pattern trajectory that resulted in each matrix containing 60 printed E-jet droplets. The printed matrices share the follow parameters:

- Printing ink: NOA 81
- Substrate: Non-coated glass slide
- Positively charged conductive printing nozzle with d_N = 8µm

Below are the lists of varying parameters:

- External standoff height: H = 200µm, 400µm, 600µm, 1000µm, 1500µm (5 levels)
- Internal standoff height: h = 50µm, 100µm (2 levels)
- Grounded extractor nozzle with a d_E = 53µm, 100 µm, 131µm (3 sizes)

The total number of combinations is therefore $5 \cdot 2 \cdot 3 = 30$.

All 30 matrices were printed utilizing a pulse printing mode; each droplet was printed with a square pulse signal of 50ms peak voltage window. The following procedure was used to determine the

peak (V_P) and baseline voltages (V_B). First, the minimum printing voltages at each standoff height (H) were averaged (as listed in Table 9) and the resulting value was defined as V_{ref}.

For each pair of d_E and h, a peak voltage $V_p = 140\% \cdot V_{ref}$ and a baseline voltage $V_B = 60\% \cdot V_{ref}$ were used to print at different external standoff heights (H). For example, for the Nozzle-in-Nozzle integrated printhead with d_E =53μm and h = 50μm, the average minimum voltage across the five standoff heights was found to be 217V. Applying the above increase and decrease, a peak voltage of 300V (299.6V) and a baseline voltage of 130V (130.2V) were used to print at the 5 external standoff heights (200μm, 400μm, 600μm, 1000μm and 1500μm), resulting in 5 matrices. Notice the highest voltage used among all 30 matrices is 459V (458.9V), which is not sufficient for regular E-jet to print on a glass surface at a standoff height of 400 μm or above (according to Table 8, a voltage of $\geq$ 474.3V is needed).

The experimentally optimized P_E (minimum printing pressure) for each pair of d_E and h are listed in Table 10. The printing performance are quantified with 5 printing quality metrics:

1. Droplet positioning consistency [I_{PC}]
2. Scattering index [I_S]
3. Droplet diameter variation [I_D]
4. Number of missing droplets [I_M]
5. Droplet diameter variation across different standoff heights [I_V]

Table 9. Experimentally determined pulse printing voltages for different settings

internal standoff height h = 50μm				internal standoff height h = 100μm			
standoff height (H)	d_E = 53μm	d_E = 100μm	d_E =131μm	standoff height (H)	d_E = 53μm	d_E = 100μm	d_E =131μm
200μm	215V	286V	299V	200μm	326V	326V	308V
400μm	217V	287V	300V	400μm	325V	330V	306V
600μm	219V	283V	302V	600μm	330V	328V	307V
1000μm	219V	290V	299V	1000μm	327V	328V	308V
1500μm	215V	285V	301V	1500μm	331V	324V	308V
Average (V_{ref})	217V	286.2V	300.2V	Average (V_{ref})	327.8V	327.2V	307.4V
140% V_{ref}	299.6V	400.7V	420.2V	140% V_{ref}	458.9V	458.1V	430.4V
60% V_{ref}	130.2V	171.6V	180.1V	60% V_{ref}	196.7V	196.3V	184.4V

Table 10. Experimentally optimized air pressure for different settings

internal standoff height h = 50μm				internal standoff height h = 100μm			
	d_E = 53μm	d_E = 100μm	d_E =131μm		d_E = 53μm	d_E = 100μm	d_E =131μm
Air pressure (P_E)	4309Pa	302Pa	431Pa	Air pressure (P_E)	3447Pa	302Pa	431Pa

To determine these 5 metrics across all 30 printed matrices, a matlab program was created to automatically identify the main droplets in the printed image. For example, the 58 most prominent droplets in the microscope image shown in Figure 45 were identified as core droplets using image processing software and illustrated in Figure 46. The remaining smaller droplets in Figure 45 were defined as satellite droplets. These two different categories of droplets were used to derive the five performance metrics described below.

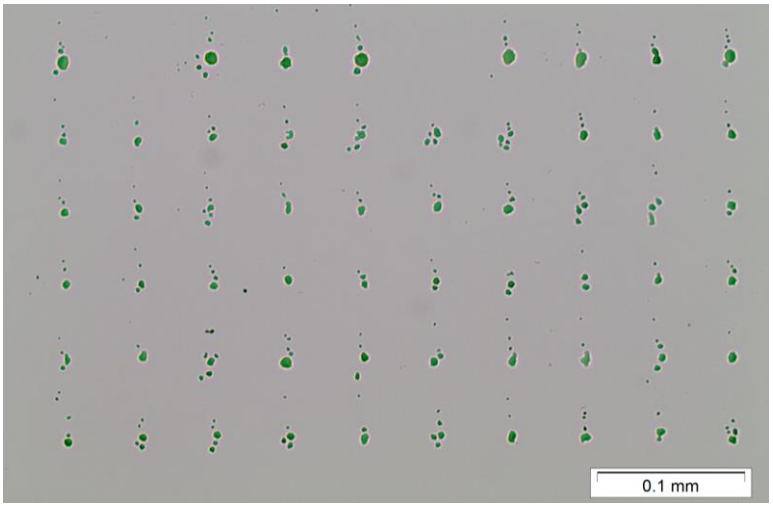

d_N	8µm
d_E	53µm
h	100µm
H	1500µm
V_P	458V
V_B	196V
Pulse width	50ms

Figure 45. A microscope image of a 60 dot matrix (2 are missing due to inconsistent printing behavior) with scattered droplets.

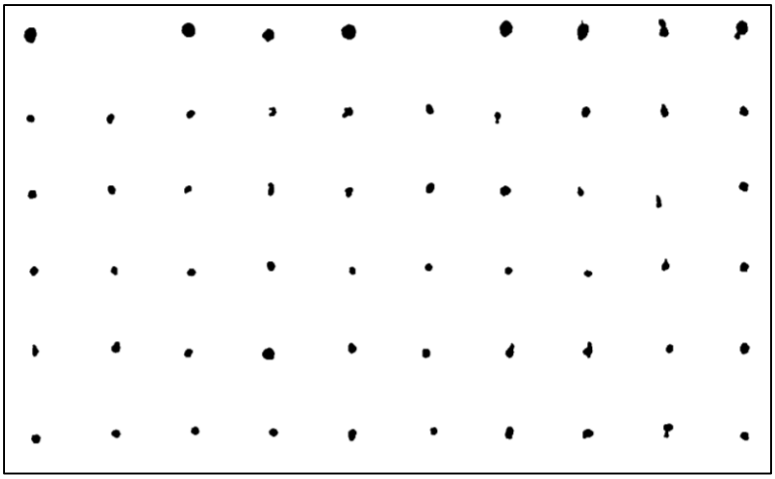

Figure 46. The matlab program processed image from Figure 45. The main droplets are selected and are presented here without the scattered satellite droplets

(i) Droplets positioning consistency [I_{PC}]

To quantify the positioning consistency of the printed droplets, we first determine the distance between all the core droplets as shown in Figure 47.

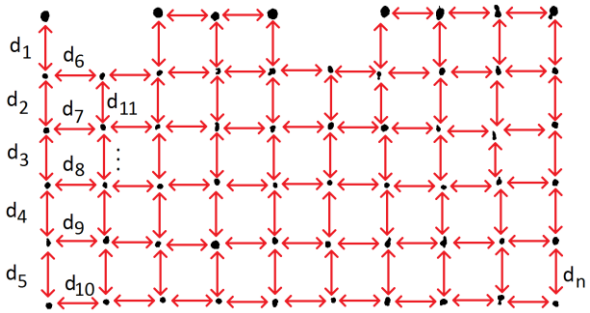

Figure 47. Schematic diagram of the measured distances between the main droplets. d_1, d_2, d_3 … are the measured distance between he main droplets, which are presented as red arrows

The droplet positioning consistency is defined as:

$$I_{PC} = \sqrt{\frac{\sum_{i=1}^{n}(d_i - \bar{d})^2}{n}} \tag{8}$$

where d_1, d_2, d_3 …d_n are all the distances between the adjacent main droplets as presented in Figure 47, n is the total number of red arrows, and $\bar{d}$ is 50µm, which is the mean of all the distances represented by the red arrows. Table 11 shows the value of I_{PC} for all 30 matrices.

As shown in Table 11, a Nozzle-in-Nozzle printhead with the following design parameters: d_N = 8µm, d_E = 100µm and h = 100µm (highlighted in green), resulted in the lowest standard deviation or best droplet positioning consistency across a substrate offset height change of 1300µm. This is the optimum setting when the d_E is not too small or too large (as explained in section 5.1.2 step 2), and the ratio between h and d_E is 1:1 (which falls within the optimum ratio described in section 5.1.2 step3).

Table 11. Droplet positioning consistency for different printing parameters

Internal Standoff height 50µm (h)					
	External standoff height (H)				
d_E	200µm	400µm	600µm	1000µm	1500µm
53µm	3.206µm	3.922µm	3.938µm	6.208µm	3.915µm
100µm	1.723µm	2.429µm	2.393µm	2.68 µm	3.196µm
131µm	2.294µm	2.32µm	2.994µm	5.081µm	8.507µm

Internal Standoff height 100µm (h)					
	External standoff height (H)				
d_E	200µm	400µm	600µm	1000µm	1500µm
53µm	1.856µm	1.779µm	2.137µm	2.693µm	2.701µm
100µm	1.005µm	2.185µm	1.454µm	1.567µm	1.806µm
131µm	1.958µm	2.502µm	2.164µm	2.595µm	3.205µm

(ii) Scattering index [I_S]

The scattering index is defined as:

$$I_S = \frac{\sum_{i=S_1}^{S_n} a_i}{\sum_{k=1}^{m} A_k} \cdot \sum_{j=S_1}^{S_n} d_j \tag{9}$$

where a_i is the area associated with satellite droplet i, A_k is the area associated with main droplet k, $s_1 \ldots s_n$ identify all satellite droplets within the image, $d_{s1} \ldots d_{sn}$ are defined as the shortest distances between the centers of the satellite droplets to the nearest main droplet center. Figure 48 illustrates a group of droplets from Figure 45, where ds_1, ds_2, ds_3 are labelled. The scattering index was derived for all of the main droplets identified across the 30 printed matrices.

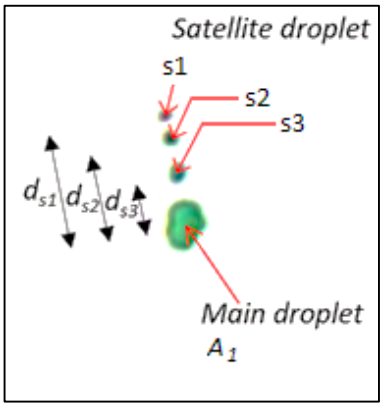

Figure 48. Microscope image of a group of droplets from Figure 45. Center distances between satellite droplets and the closest main droplet labelled ds_1, ds_2, ds_3.

The scattering index was defined to incorporate the impact of three key metrics:

1. Relative size of the satellite droplets compared to the main droplet
2. Distance between the satellite droplets and the center of the closest core droplet
3. Number of satellite droplets

As the size, relative distance, and number of satellite droplets increases, the scattering index will increase. This increase was typically found to correlate with increased offset height between the substrate and the extractor nozzle. Table 12 shows the scattering indexes for all 30 matrices printed in this set of experiments. Similar to the previous findings, the parameter design with the lowest scattering index was found to be: d_N = 8µm, d_E = 100µm and h = 100µm (highlighted in green).

It is worth noting that the air pressure P_E used in this setting is the lowest among all settings (Table 10), which generates the least amount of scattering as explained in section 5.1.2 step 4. Figures 49 and 50 provide a representation of matrices with large and small scattering indexes.

Table 12. Scattering index for different printing parameters

Internal Standoff height 50µm (h)					
	External standoff height (H)				
d_E	200µm	400µm	600µm	1000µm	1500µm
53µm	4.045	46.968	50.392	1075	1581.7
100µm	0.1046	0.47	9.192	39.675	95.76
131µm	1.144	6.515	26.761	57.341	106.032

Internal Standoff height 100µm (h)					
	External standoff height (H)				
d_E	200µm	400µm	600µm	1000µm	1500µm
53µm	2.702	4.652	5.333	11.937	27.307
100µm	0.035	0.201	0.02	0.094	0.2213
131µm	2.267	2.764	9.769	26.076	41.967

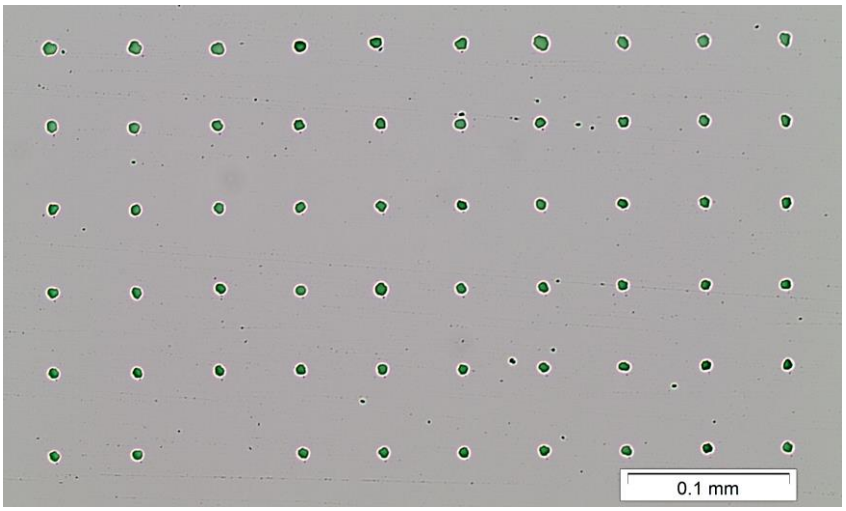

d_N	8μm
d_E	100μm
h	100μm
H	200μm
V_P	458V
V_B	196V
Pulse width	50ms
Scattering index	0.035

Figure 49. A matrix with minimum scattering behavior. The scattering index of this matrix is 0.035.

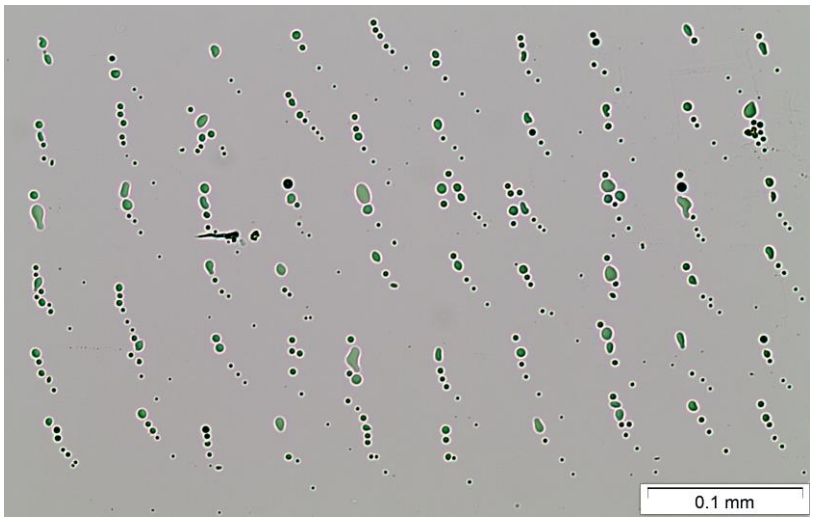

d_N	8μm
d_E	100μm
h	50μm
H	1500μm
V_P	400V
V_B	171V
Pulse Width	50ms
Scattering index	95.67

Figure 50. A matrix with prominent scattering behavior. The scattering index of this matrix is 95.76.

(iii) Droplet diameter variation [I_D]

The droplet diameter variation is defined as:

$$I_D = \sqrt{\frac{\sum_{i=1}^{n}(d_{diameter,i} - \overline{d_{diameter}})^2}{n}} \quad (10)$$

The formula represents the standard deviation of the main droplet diameters in a matrix. The smaller the standard deviation, the more consistent the printing within a matrix.

Two of the best sets of results are highlighted in green in Table 13. It is worth noting that with design parameters d_E = 53μm and h = 100μm, the scattering index of this set of conditions is not

Table 13. Droplet diameter for different printing parameters

Internal Standoff height 50µm (h)					
	External standoff height (H)				
d_E	200µm	400µm	600µm	1000µm	1500µm
53µm	0.849µm	0.855µm	2.705µm	1.17µm	0.937µm
100µm	0.893µm	0.594µm	0.526µm	0.853µm	0.5655µm
131µm	1.267µm	0.702µm	0.847µm	1.638µm	1.396µm

Internal Standoff height 100µm (h)					
	External standoff height (H)				
d_E	200µm	400µm	600µm	1000µm	1500µm
53µm	0.28µm	0.339µm	0.331µm	0.836µm	1.27µm
100µm	0.575µm	0.89µm	0.53µm	0.45µm	0.282µm
131µm	0.62µm	0.84µm	0.844µm	0.844µm	0.818µm

ideal (ranging from 2.7 to 27.3) as compared to the scattering index when d_E = 100µm and h = 100µm (ranging from 0.035 to 0.221). As such, one can conclude that small droplet diameter variations do not necessarily correlate with a low scattering index.

(iv) Factor of missing droplets [I_M]

The factor of missing droplets is defined as:

$$I_M = \frac{number\ of\ missing\ droplets}{number\ of\ droplets\ in\ a\ matrix} \tag{11}$$

This performance metric regarding the number of missing droplets can be used to provide a means of evaluating printing robustness. While the previous metrics describe inconsistencies in droplet placement or the presence of satellite droplets, a missing droplet indicates that for some reason the process either (1) did not eject a droplet, (2) the droplet ejected but was captured on the extractor nozzle rather than released through the extractor orifice, or (3) the droplet merged with another droplet on the substrate. The first two cases would only impact the missing droplet metric, while the second case would also be reflected in the droplet diameter variation metric. The factor of missing droplets for all 30 matrices are listed in Table 14.

There are in general fewer droplets missing when h = 50µm as compared to h = 100µm. This is a very reasonable result; if the printing nozzle gets closer to the extractor nozzle, the attraction force upon the droplets is stronger and more reliable, giving a more consistent jetting performance. This consistency is at a price of higher scattering indexes. The horizontal components acting upon the

Table 14. Factor of missing droplets for different printing parameters

Internal Standoff height 50µm (h)					
	External standoff height (H)				
d_E	200µm	400µm	600µm	1000µm	1500µm
53µm	0	0	0.033	0	0
100µm	0	0	0	0	0
131µm	0	0	0	0	0

Internal Standoff height 100µm (h)					
	External standoff height (H)				
d_E	200µm	400µm	600µm	1000µm	1500µm
53µm	0	0	0	0	0.033
100µm	0.017	0	0.017	0	0
131µm	0	0.017	0	0	0

ink droplets are larger when h = 50 µm, which requires a stronger airflow to redirect the droplets, leading to more prominent scattering behavior.

(v) Droplet diameter variation across different standoff heights [I_V]

This metric is used to investigate consistency of the printing performance across different external standoff heights H. The average droplet diameters of the 30 matrices are listed in Table 15. For each pair of d_E and h, the droplet size variation is defined as the difference between the largest droplet diameter among the 5 standoff height levels (200µm, 400µm, 600µm, 1000µm, 1500µm) and the smallest droplet diameter among the 5 standoff height levels:

$$I_V = \max(d_{diameter}) - \min(d_{diameter}) \quad (12)$$

As shown in Table 15, the droplet size variation across the 5 standoff height levels is the smallest when d_E = 53µm and h = 100µm (highlighted in green). As mentioned earlier in part (ii) of this section, we know that the scattering index of this pair of parameter is not ideal. With d_E = 100µm and h = 100µm, the droplets size variation is 0.63µm (highlighted in yellow), which is the second best result among all 30 matrices. This set of design parameters was determined to provide the best overall performance across the five define metrics.

Table 15. Average printed droplet sizes for different printing parameters

Internal Standoff height 50µm (h)						
d_E	External standoff height (H) 200µm	400µm	600µm	1000µm	1500µm	Droplet size variation
53µm	9.15µm	7.87µm	9.83µm	6.70µm	6.40µm	3.42µm
100µm	8.09µm	7.01µm	6.21µm	5.94µm	5.65µm	2.44µm
131µm	8.01µm	7.07µm	6.94µm	7.13µm	6.37µm	1.64µm

Internal Standoff height 100µm (h)						
d_E	External standoff height (H) 200µm	400µm	600µm	1000µm	1500µm	Droplet size variation
53µm	6.42µm	6.15µm	6.15µm	6.41µm	6.22µm	0.27µm
100µm	6.87µm	6.88µm	6.39µm	6.48µm	6.25µm	0.63µm
131µm	8.37µm	7.96µm	7.12µm	6.40µm	5.89µm	2.48µm

(vi) Metric normalization and performance cost function [C]

To compare the various metrics, the metrics needed to be normalized. All the metrics (except I_M) are normalized by dividing the value of the metric with the largest value among them all. For example, the normalized I_{PC} is defined as:

$$\overline{I_{PC}} = \frac{I_{PC}}{\max(I_{PC})} \quad (13)$$

The normalized metrics and original I_M are provided in Table 16. I_M is not normalized because it is a normalized index by definition.

Table 16. Normalized performance metrics for different printing parameters

Internal Standoff height 50µm (h)						Internal Standoff height 100µm (h)					
d_E	$\overline{I_{PC}}$	$\overline{I_S}$	$\overline{I_D}$	I_M	$\overline{I_V}$	d_E	$\overline{I_{PC}}$	$\overline{I_S}$	$\overline{I_D}$	I_M	$\overline{I_V}$
53µm	1.00	1.000	1.00	0.033	1.00	53µm	0.53	0.019	0.47	0.033	0.08
100µm	0.59	0.053	0.52	0	0.71	100µm	0.38	0.0002	0.42	0.033	0.18
131µm	1.00	0.072	0.90	0	0.48	131µm	0.58	0.030	0.61	0.017	0.73

To truly identify the optimal design parameters, we must consider the cost of all five performance metrics. The weighted cost function is defined as:

$$\min_{\{\overline{I_{PC}},\overline{I_S},\overline{I_D},\overline{I_M},\overline{I_V}\}\in[0,1]} C = W_{PC}\cdot\overline{I_{PC}} + W_S\cdot\overline{I_S} + W_D\cdot\overline{I_D} + W_M\cdot I_M + W_V\cdot\overline{I_V} \qquad (14)$$

Where W_{PC}, W_S, W_D, W_M and W_V are the weighting gains associated with each performance metric. These weights are preference dependent. For example, to optimize the printhead for minimum scattering, W_S should be increased relatively to the other 4 weights in order to emphasize the importance of I_S in the cost function.

With a set of decided weights, the optimum set of key parameters can be determined by minimizing the cost function C. For example, with W_S =20, and W_{PC}, W_D, W_M and W_V = 1, the cost function for the 6 pairs of d_E and h are listed in Table 17:

Table 17. Cost function comparison

Internal Standoff height 50µm (h)							Internal Standoff height 100µm (h)						
	Weighted Performance Metrics							Weighted Performance Metrics					
d_E	$\overline{I_{PC}}$	$20\cdot\overline{I_S}$	$\overline{I_D}$	I_M	$\overline{I_V}$	Cost	d_E	$\overline{I_{PC}}$	$20\cdot\overline{I_S}$	$\overline{I_D}$	I_M	$\overline{I_V}$	Cost
53µm	1.00	20.000	1.00	0.033	1.00	23.03	53µm	0.53	0.38	0.47	0.033	0.08	1.49
100µm	0.59	1.06	0.52	0	0.71	2.88	100µm	0.38	0.004	0.42	0.033	0.18	1.02
131µm	1.00	1.44	0.90	0	0.48	3.82	131µm	0.58	0.60	0.61	0.017	0.73	2.54

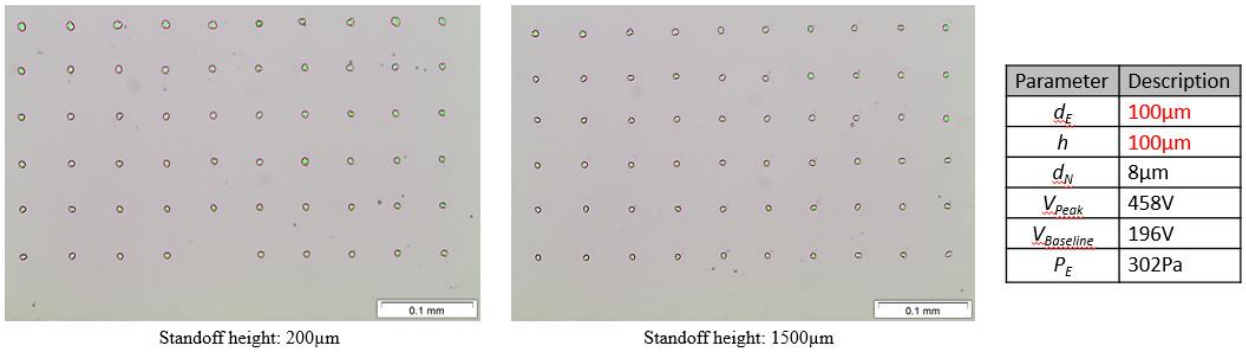

Standoff height: 200µm Standoff height: 1500µm

Figure 51. Matrices printed by the performance metrics that minimized the cost function in equation (14)

The case with d_E = 53µm and h = 100µm was found to minimize the cost function for the given weights (highlighted in green). Figure 51 shows printed matrices using the determined optimal design parameters at standoff heights of 200µm and 1500µm; these images demonstrate the consistency, robustness, and minimal scattering that resulted from this design selection.

5.3 Deficiencies of Nozzle-in-Nozzle E-jet Printhead

There are two major issues with the Nozzle-in-Nozzle printhead at the current stage: (1) coupled aerodynamics and electrohydrodynamics and (2) airflow being directed towards the substrate.

In the current design, the extractor nozzle opening diameter d_E influences both the electrohydrodynamics and airflow. Similar to the deficiencies denoted in the two nozzles style printhead described in section 4.2.4, the airflow cannot be adjusted independently from the electrostatic field in a Nozzle-in-Nozzle printhead.

As we use the Nozzle-in-Nozzle printhead to print on tilted surfaces, we observe very prominent scattering effects (see Figure 52). A probable reason for the scattering behavior is the excessive airflow delivered to the substrate along with the droplet. To reduce the amount of airflow, an effective approach is to create a smaller extractor nozzle opening (use a smaller d_E). However, as the extractor opening gets smaller, the distance between the ink droplet and the inner edge of the extractor nozzle opening will also decrease, which greatly increases the horizontal electrostatic

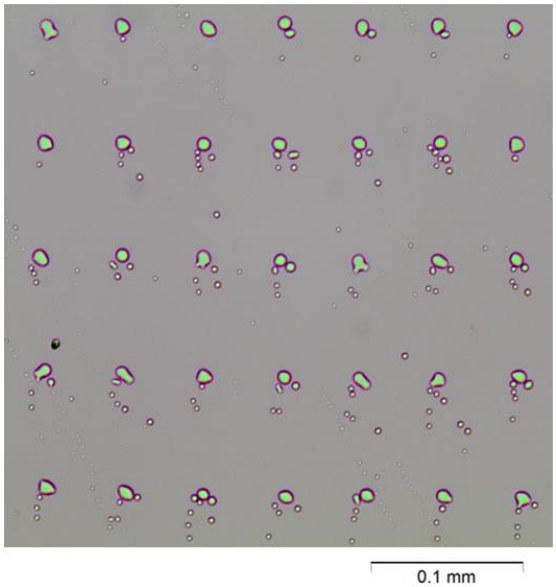

d_N	8µm
d_E	100µm
h	10µm
V_P	458V
V_B	196V
Pulse Width	50ms

Figure 52. A matrix printed on 45° tilted glass surface with Nozzle-in-Nozzle printhead. Prominent scattering behavior is observed. Standoff heights H vary from [200,400µm] by 50µm, starting at the top.

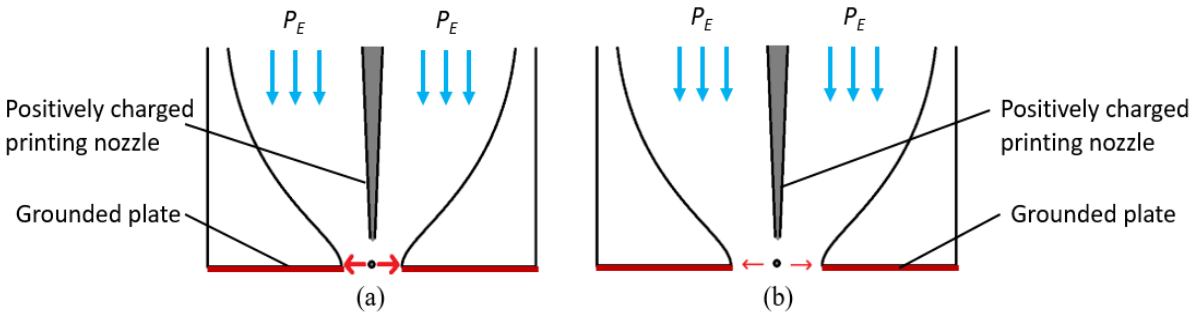

Figure 53. Schematic diagram of electrostatic forces with different d_E. (a) Small extractor nozzle openings exhibit large horizontal electrostatic forces (thick red arrows). (b) Large extractor nozzle openings exhibit weaker horizontal electrostatic forces, represented by thinner red arrows.

forces acting on the droplets as they pass through the extractor nozzle opening (see Figure 53(a)). Therefore, a higher air pressure is needed to redirect the droplets away from the inner edge of the extractor nozzle opening, leading to prominent scattering behavior. For example, the scattering index is larger when d_E = 53µm instead of 100µm as presented in chapter 5.2.2 section (ii).

A more fundamental issue with this current design is the airflow being directed towards the substrate along with the droplet. As the airflow travels towards the substrate along with the droplet, the airflow scatters not only the droplet that is in the air, but may also be scattering the previously printed ink droplets that are currently residing on the substrate. Through the experimental tests, it was observed that the core function of the airflow should be to cancel the horizontal electrostatic forces derived from the extractor nozzle (represented with red arrows in Figure 54). To enable more independent electrostatic and airflow control, the airflow directionality should be restricted to a weak horizontal airflow (dotted arrows) applied at the inner edge of the extractor nozzle opening, Figure 54. This horizontal airflow should be sufficient to redirect droplets away from the inner edge without inducing scattering. Since the airflow is not directed down towards the substrate, the airflow would disperse in both the up and down directions with a low velocity; creating minimum droplet scattering or airflow turbulence around the substrate surface.

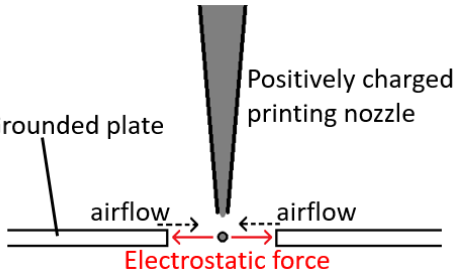

Figure 54. Schematic diagram of integrated nozzle with horizontal airflow. Red arrows represent horizontal electrostatic forces. Black dotted arrows represent horizontal airflow sufficient to redirect the droplets without inducing scattering.

Chapter 6

Concluding Remarks and Future Directions

This chapter provides some concluding remarks and a few suggestions for future directions. Key contributions of the research, as well as some important lessons learned are provided.

6.1 Conclusion Remarks

To overcome the substrate effect in electrohydrodynamics, we have explored and investigated various printing techniques and approaches. Through our experiments, we have acquired a better understanding of the different physics governing the electrohydrodynamics. Based on our experimental and simulation-based observations across a broad range of printhead designs, our scientific contributions include: (1) The generation of practical theories that blend physics-based models with data-driven understandings to predict ink droplet trajectory, scattering, jetting consistency and nozzle cross-talk behaviors under a variety of electrostatic field geometries; (2) The construction of simulation models and experimental hardware that can be used to estimate and validate the inflight directionality change and scattering behavior of ink droplets under different aerodynamics conditions; and (3) The derivation of several key performance metrics that can be used to quantify the jetting behavior in varying printing conditions. This knowledge will enable a researcher to predict the feasibility, reliability and performance of new E-jet printhead designs on different substrate surfaces in simulation, and validate these predictions through quantifiable experimental tests.

Technical contributions of this dissertation include the demonstration of different fabrication techniques as well as the development and characterization of a novel airflow assisted E-jet printing process; a new printing technique with a high potential for enhanced printing performance. The printing results from this new printing technique show promise; under certain conditions, the printed results demonstrated that the substrate effect was sufficiently mitigated; enabling functional E-jet printing across a large range of standoff heights.

There were two very important lessons that were learned as a result of the work in this dissertation. First, we developed an understanding and appreciation for the tradeoffs associated with design considerations and printing performance. The initial aim of this research was to provide enhanced flexibility within the E-jet printing process, particularly in terms of the types of substrates onto which the process could consistently and robustly print. This project was primarily motivated by this need to relax the substrate restrictions in E-jet printing. As new printhead designs were developed to achieve this goal, we encountered new fabrication and printing challenges related to the fabrication/alignment tolerances at the microscale. This is in stark contrast to what one might experience with macroscale E-jet printhead designs. In the macro-scale, misalignment and design variations result in fairly insignificant effects on the printing performance. As we pushed our designs to the microscale, the impact of these slight design imperfections was greatly amplified, leading to important design tradeoffs that drove the outcomes of the different performance metrics. With a consideration towards lost-cost E-jet printing systems, we focused our exploration of design strategies to mitigate the effects of misalignment at the microscale on creative solutions that leveraged the physics that governed the process to enhance our designs. Through this approach we are able to create practical and inexpensive designs that approach commercial standards.

The second critical lesson came from understanding the importance of symmetrical forces and shielding within the E-jet printhead design. During the design iterations, the importance of these two parameters became increasingly apparent. Through this discovery, we were able to define critical design metrics that would result in a printhead design that met the performance requirements. As the application of E-jet printing becomes more fully integrated into 3D printing for biological, electrical and optical devices, the need for a robust E-jet printhead that is capable of printing onto contoured and insulated surfaces increases. Traditional E-jet printing cannot meet this demand; however, the Nozzle-in-Nozzle design, due to the symmetric forces and integrated shielding effects, has shown tremendous potential to meet this demand. As we explored this space, we realized that symmetrical forces and shielding became paramount for success printing.

6.2 Future Directions

The ultimate goal of this research was to understand the physics that govern the electrohydrodynamic jetting process and leverage this knowledge to design and fabricate commercially viable E-jet printing systems. Future research directions aimed at further addressing this goal will build off of our existing knowledge and expertise in this area. These advancements will leverage the existing design framework to enable advanced E-jet printing applications. These activities could include:

1. Understanding the printing process requirements to fabricate functional electronics or biomedical devices using the integrated Nozzle-in-Nozzle E-jet printing system.
2. Investigating further design improvements to the integrated printhead to enable E-jet printing onto highly contoured (out-of-plane) surfaces.
3. Creating a simple yet reliable procedure to produce functional integrated printheads at small scale for research use.
4. Designing a manufacturing approach for mass production of integrated E-jet printheads, including multi-nozzle printheads that utilizes the integrated nozzle actuation system.

We will describe the each of these directions in detail within the follow sections.

6.2.1 Understanding the Needs for E-jet Printing of Functional Electronics and Biomedical Devices

Currently there are a lot of electronic device development and research projects seeking low cost and flexible manufacturing processes for the fabrication of high-resolution (<20μm) circuits or sensors. As explained in chapter 1.2, MEMS (Micro-Electro-Mechanical Systems), inkjet printing and contact printing technologies all have their shortcomings and E-jet can potentially fill the void where these traditional technologies fall short.

Many electronics development processes involve the creation of high-resolution conductive patterns onto non-conductive substrates. In general, these surfaces provide poor substrates for traditional E-jet printing due to three factors:

1. The surfaces are not flat; most consist of a surface roughness of 5-200μm.

2. Many of these substrates are non-conductive and thick, which means classic techniques such as placing grounded plates under these non-conductive substrates may fail to create consistent electrohydrodynamic behaviors.
3. Some of these substrates may contain residue electrostatic charges that can influence the electrohydrodynamics at the printing nozzle tip.

One such example is the recent work on flexible electronics with elastic conductive inks on silicon rubber (Chortos, A., et al. (2016)). Researchers developing artificial prosthetic skin with tactile sensing capabilities are looking into technologies that can create conductive patterns on non-flat surfaces with a resolution of 20μm. Projects such as these will serve as ideal application examples for our integrated E-jet printhead.

As silicon 3D printing technologies mature, we will investigate the challenges around E-jet printing onto 3D printed silicon rubber surfaces. A hybrid printing example such as this will demonstrate a fully customizable flexible electronic: both the silicon substrate and the printed conductive circuits upon it can be customized and fabricated without the need for templates or molds.

6.2.2 Further improving the printing quality of the integrated printhead

Independent control of the airflow and electrohydrodynamics may be necessary to enable integrated E-jet printing onto more contoured and tilted surfaces. Significant scattering was observed while printing onto a tilted surface (Figure 52). Design and fabrication of a Nozzle-in-Nozzle design that enables horizontal airflow, illustrated in Figure 54, may provide the necessary actuation control to redirect the droplets away from the extractor nozzle orifice, while mitigating droplet scattering on the substrate surface. Novel preliminary design concepts for horizontal airflow control are provided in Figures 55 and 56. Figure 55 illustrates a design that regulates the airflow towards a horizontal component. 3D printing for the fabrication of the air releasing mechanism that can eject airflow radially along the extractor hole may be used given the design complexity. A more traditional approach to test the concept would include the integration of two or more nozzles to release horizontal airflow around the printing nozzle as shown in Figure 56.

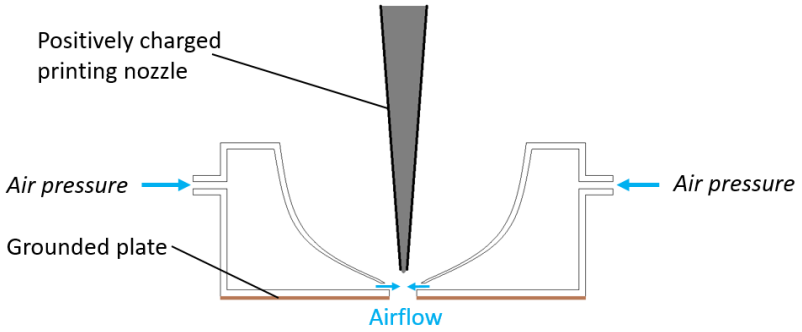

Figure 55. Schematic diagram of an integrated nozzle with a horizontal airflow releasing mechanism. The air releasing mechanism may be 3D printed due to its geometry complexity.

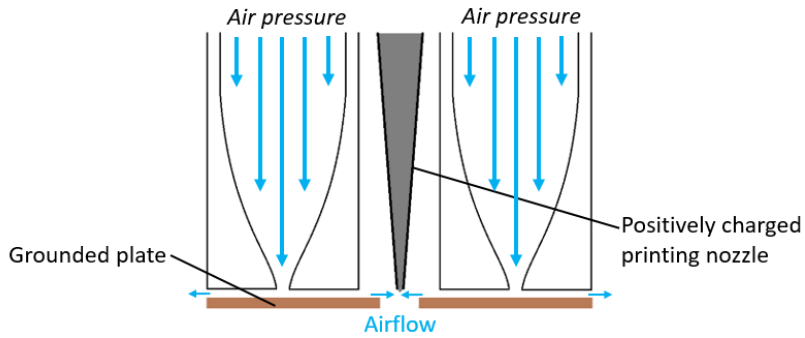

Figure 56. Schematic diagram of an integrated nozzle with two air jetting nozzles to create horizontal airflow around the printing nozzle

To investigate the printing capability of these prototypes, one would conduct printing experiments similar to the ones described in this dissertation and apply the performance metrics described in section 5.2.2.

6.2.3 Create a simple yet reliable procedure to produce functional integrated printheads

At this stage, the integrated printhead prototypes include complicated design concepts and require a tremendous amount of practice before the user can construct them consistently. For research and application projects, a more readily available and easy to setup printhead should be designed. Users should be able to fill the printing nozzle with ink and setup the printhead for use with minimum training.

The most challenging procedure in the integrated printhead construction process is the alignment of all the micron scale features (printing nozzle tip, air releasing nozzle, extractor nozzle opening, etc), which takes a lot of practice before consistent alignment can be completed. One solution to this issue is to design the integrated printhead with precise locating features, which will align the

components automatically during the assembly process. This research direction is still in the concept stage and will be continue in the future.

6.2.4 Design a Manufacturing Approach for Mass Production of an Integrated Printhead

By simplifying the design of the integrated E-jet printhead into perpendicular microfluidic channels and electrode pads, we may be able to convert the airflow assisted E-jet printhead into a MEMS device (Figure 57) that can be rearranged into a multi-nozzle array for high throughput E-jet printing. Initial fabrication efforts may be focused at the 200-800µm scale prior to creating a high precision microscopic printhead prototype. This would allow one to prove the concept before investing time and money into MEMS technology. There are also significant challenges associated with this proposed research direction:

- Electric field interference with neighboring nozzles: it is well documented (Choi, K. H., *et al*., 2011, Takagi, M. F., 2013) that nozzles in close proximity to each other will exert electrostatic field interference. This will need to be further studied in order to design an appropriately shielded printhead for multi-nozzle printing.
- Material delivery: the delivery of material becomes more complicated once a MEMs approach is considered. Material compatibilities and the potential use of micro-fluidics are some of the challenges that must be investigated for this design approach.

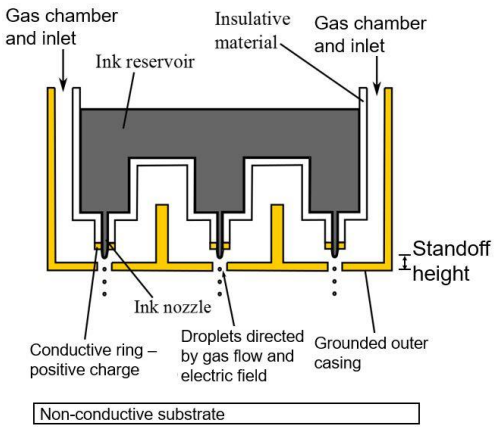

Figure 57. Schematic diagram of a MEMS airflow assisted E-jet printhead

- Optimized design parameters: preliminary work has been focused on nozzle alignment and parameters. This will change significantly if the design moves towards micro channels rather than nozzles. The modeling, analysis and experimental testing for these variations will need to be conducted.
- Fabrication: MEMS fabrication introduces design and manufacturing challenges stemming from the chemical and etching properties of the fluid involved, yield rate improvement will be a major challenge in the development process.

BIBLIOGRAPHY

Albertson, M. L., Dai, Y. B., Jensen, R. A., & Rouse, H. (1950). "Diffusion of submerged jets". *Transactions of the American Society of Civil Engineers*, Vol. 115(1), 639-664.

Allain, L. R., Stratis-Cullum, D. N., & Vo-Dinh, T. (2004). "Investigation of microfabrication of biological sample arrays using piezoelectric and bubblE-jet printing technologies". *Analytica chimica acta*, Vol. 518(1), 77-85.

Altin, B., Tse, L., Barton, K. (2014), "Visual Feedback based Droplet Size Regulation in Electrohydrodynamic Jet Printing", In *ASME 2014 Dynamic Systems and Control Conference,* (pp. DSCC2014-6110) American Society of Mechanical Engineers.

Barton, K., Mishra, S., Alleyne, A., Ferreira, P., & Rogers, J. (2011). "Control of high-resolution electrohydrodynamic jet printing". *Control Engineering Practice*, Vol. 19(11), 1266-1273.

Bernard, A., Fitzli, D., Sonderegger, P., Delamarche, E., Michel, B., Bosshard, H. R., & Biebuyck, H. (2001). "Affinity capture of proteins from solution and their dissociation by contact printing". *Nature biotechnology*, Vol. 19(9), 866-869.

Buehner, W. L., Hill, J. D., Williams, T. H., & Woods, J. W. (1977). "Application of ink jet technology to a word processing output printer". *IBM Journal of Research and Development*, Vol. 21(1), 2-9.

Choi, H. K., Park, J. U., Park, O. O., Ferreira, P. M., Georgiadis, J. G., & Rogers, J. A. (2008). "Scaling laws for jet pulsations associated with high-resolution electrohydrodynamic printing". *Applied Physics Letters*, Vol. 92(12), 123109.

Choi, J., Kim, Y. J., Lee, S., Son, S. U., Ko, H. S., Nguyen, V. D., &Byun, D. (2008). "Drop-on-demand printing of conductive ink by electrostatic field induced inkjet head". *Applied Physics Letters*, Vol. 93(19), 193508.

Choi, K. H., Rahman, K., Khan, A., & Kim, D. S. (2011). "Cross-talk effect in electrostatic based capillary array nozzles". *Journal of mechanical science and technology*, Vol. 25(12), 3053-3062.

Chortos, A., Liu, J., & Bao, Z. (2016). "Pursuing prosthetic electronic skin". *Nature Materials*, Vol.15(9), 937-950.

Duffy, S., Bozler, C., Rabe, S., Knecht, J., Travis, L., Wyatt, P., ... & Gouker, M. (2001). "MEMS microswitches for reconfigurable microwave circuitry". *Microwave and Wireless Components Letters, IEEE*, Vol. 11(3), 106-108.

Eyring, C. F., Mackeown, S. S., & Millikan, R. A. (1928). “Fields currents from points”. *Physical Review*, , Vol. 31(5), 900.

Handran, C. Wang, and D. Aziz, Axon Instruments, Inc., GenePix Application Note, 2001

Hayati, I., Bailey, A. I., & Tadros, T. F. (1986). “Mechanism of stable jet formation in electrohydrodynamic atomization”. *Nature*, Vol. 319(6048), 41-43.

Jaworek, A., & Krupa, A. (1999). “Classification of the modes of EHD spraying”. *Journal of Aerosol Science*, Vol. 30(7), 873-893.

Khan, A., Rahman, K., Hyun, M. T., Kim, D. S., & Choi, K. H. (2011). “Multi-nozzle electrohydrodynamic inkjet printing of silver colloidal solution for the fabrication of electrically functional microstructures”. *Applied Physics A*, Vol. 104(4), 1113-1120.

Kim, Y., Son, S., Choi, J., Byun, D., & Lee, S. (2008). “Design and fabrication of electrostatic inkjet head using silicon micromachining technology”. *J Semi Conductor Tech Sci*, Vol. 8(2), 121-127.

Korkut, S., Saville, D. A., & Aksay, I. A. (2008). “Collodial cluster arrays by electrohydrodynamic printing”. *Langmuir*, Vol. 24(21), 12196-12201.

Kumar, A., & Whitesides, G. M. (1993). “Features of gold having micrometer to centimeter dimensions can be formed through a combination of stamping with an elastomeric stamp and an alkanethiol ‘‘ink’’followed by chemical etching”. .*Applied Physics Letters*, Vol. 63(14), 2002-2004.

Lai, S. T., Chan, K., & Cook, K. (1980). “Electrohydrodynamic ionization mass spectrometry of poly (ethylene glycols)”. *Macromolecules*, Vol. 13(4), 953-956.

Lee, J. S., Kim, S. Y., Kim, Y. J., Park, J., Kim, Y., Hwang, J., & Kim, Y. J. (2008). “Design and evaluation of a silicon based multi-nozzle for addressable jetting using a controlled flow rate in electrohydrodynamic jet printing”. *Applied Physics Letters*, Vol. 93(24), 243114.

Lee, J. S., Kim, Y. J., Kang, B. G., Kim, S. Y., Park, J., Hwang, J., & Kim, Y. J. (2009). “Electrohydrodynamic jet printing capable of removing substrate effects and modulating printing characteristics”.In *Micro Electro Mechanical Systems, 2009.MEMS 2009. IEEE 22nd International Conference on* (pp. 487-490). IEEE.

Lee, S., Byun, D., Jung, D., Choi, J., Kim, Y., Yang, J. H., ...&Ko, H. S. (2008). “Pole-type ground electrode in nozzle for electrostatic field induced drop-on-demand inkjet head”. *Sensors and Actuators A: Physical*, Vol. 141(2), 506-514.

Li, D., & Xia, Y. (2004). “Electrospinning of nanofibers: reinventing the wheel?”..*Advanced materials*, Vol. 16(14), 1151-1170.

Liang, X., Fu, Z., & Chou, S. Y. (2007). “Graphene transistors fabricated via transfer-printing in device active-areas on large wafer”. *Nano Letters*, Vol. 7(12), 3840-3844.

Marginean, I., Nemes, P., & Vertes, A. (2006). “Order-chaos-order transitions in electrosprays: The electrified dripping faucet”. *Physical review letters*, Vol. 97(6), 064502.

Onses, M. S., Sutanto, E., Ferreira, P. M., Alleyne, A. G., & Rogers, J. A. (2015). “Mechanisms, Capabilities, and Applications of High-Resolution Electrohydrodynamic Jet Printing”. *small*, Vol. 11(34), 4237-4266.

Takagi, M. F. and Ferreira, P. M., (2013), “Multi-Nozzle Array Electrohydrodynamic Jet (E-jet) Printing”, *Proceedings of North America Manufacturing Research Conference*, Vol. 41, 1607

Mishra, S., Barton, K. L., Alleyne, A. G., Ferreira, P. M., & Rogers, J. A. (2010).“High-speed and drop-on-demand printing with a pulsed electrohydrodynamic jet”. *Journal of Micromechanics and Microengineering*, Vol. 20(9), 095026.

Pan, Y., Huang, Y., Guo, L., Ding, Y., & Yin, Z. (2015). “Addressable multi-nozzle electrohydrodynamic jet printing with high consistency by multi-level voltage method”. *AIP Advances*, Vol. 5(4), 047108.

Park, J.U., Hardy, M., Kang, S.J., Barton, K., Adair, K., kishore Mukhopadhyay, D., Lee, C.Y., Strano, M.S., Alleyne, A.G., Georgiadis, J.G. and Ferreira, P.M., (2007). “High-resolution electrohydrodynamic jet printing”. *Nature materials*, Vol. 6(10), 782-789.

Park, J.U., Lee, S., Unarunotai, S., Sun, Y., Dunham, S., Song, T., Ferreira, P.M., Alleyene, A.G., Paik, U. and Rogers, J.A. (2010). “Nanoscale, electrified liquid jets for high-resolution printing of charge”. *Nano letters*, Vol. 10(2), 584-591.

Poellmann, M. J., Barton, K. L., Mishra, S., & Johnson, A. J. W. (2011). Patterned hydrogel substrates for cell culture with electrohydrodynamic jet printing. *Macromolecular bioscience*, Vol. 11(9), 1164-1168.

Rothschild, M., Bloomstein, T.M., Fedynyshyn, T.H., Kunz, R.R., Liberman, V., Switkes, M., Efremow, N.N., Palmacci, S.T., Sedlacek, J.H., Hardy, D.E. and Grenville, A. (2003). “Recent trends in optical lithography”.*Lincoln Laboratory Journal*, Vol. 14(2), 221-236.

Salaita, K., Wang, Y., & Mirkin, C. A. (2007). “Applications of dip-pen nanolithography”. *Nature Nanotechnology*, Vol. 2(3), 145-155.

Saunders, R. E., Gough, J. E., & Derby, B. (2008). “Delivery of human fibroblast cells by piezoelectric drop-on-demand inkjet printing”. *Biomaterials*, Vol. 29(2), 193-203.

Schmid, H., Wolf, H., Allenspach, R., Riel, H., Karg, S., Michel, B., & Delamarche, E. (2003). “Preparation of metallic films on elastomeric stamps and their application for contact processing and contact printing”. *Advanced Functional Materials*, Vol. 13(2), 145-153.

Seong, B., Yoo, H., Nguyen, V. D., Jang, Y., Ryu, C., & Byun, D. (2014). “Metal-mesh based transparent electrode on a 3-D curved surface by electrohydrodynamic jet printing”. *Journal of Micromechanics and Microengineering*, Vol. 24(9), 097002.

Sharma, K., Macwan, I., Zhang, L., Hmurcik, L., & Xiong, X. (2008, March). “Design optimization of MEMS comb accelerometer”. In *ASEE Zone 1 Conference 2008* (pp. 28-29).

Song, C., Rogers, J. A., Kim, J. M., & Ahn, H. (2015). Patterned polydiacetylene-embedded polystyrene nanofibers based on electrohydrodynamic jet printing. *Macromolecular Research*, *23*(1), 118-123.

Takagi, M. F., Ferreira, P. M. (2013), “Multi-Nozzle Array Electrohydrodynamic Jet (Ejet) Printing”, *Proceedings of North American Manufacturing Research Conference by NAMRI/SME,* Vol. 41

Wei, C., & Dong, J. (2014). “Hybrid hierarchical fabrication of three-dimensional scaffolds”. *Journal of Manufacturing Processes,* Vol. 16(2), 257-263.

Wei, C., Qin, H., Ramírez-Iglesias, N. A., Chiu, C. P., Lee, Y. S., & Dong, J. (2014). “High-resolution ac-pulse modulated electrohydrodynamic jet printing on highly insulating substrates”. *Journal of Micromechanics and Microengineering*, Vol. 24(4), 045010.

Xue, W., & Li, P. (2011). “Dielectrophoretic Deposition and Alignment of Carbon Nanotubes”. Carbon Nanotubes - Synthesis, Characterization, Applications.

Zeleny, J. (1914). “The electrical discharge from liquid points, and a hydrostatic method of measuring the electric intensity at their surfaces”. *Physical Review*, Vol. 3(2), 69.